The Structural Biology of HIV Budding and Maturation

Thesis by

Megan J. Dobro

In Partial Fulfillment of the Requirement for the

Degree of

Doctor of Philosophy

CALIFORNIA INSTITUTE OF TECHNOLOGY

Pasadena, California

2012

(Defended May 14, 2012)

ACKNOWLEDGEMENTS

I would first like to thank all of the great teachers I had who made learning so much fun. Teachers greatly impact the direction of a person's life, and I am grateful that I was led to academia and will teach future generations of lifelong learners.

I would like to acknowledge the Student Leadership Training Program who taught me how to be curious and never stop asking "why?" Many of my morals, values, and life perspectives were built while working with SLTP, and I often reach into those lessons when faced with a difficult situation.

The foundation of my science career is built on the confidence I gained while working with Meri Krevosky and Jeff Bowen at Bridgewater State University. They are wonderful mentors and have become good friends. It was with their help that I was able to work at the Marine Biological Laboratory in Woods Hole, MA for two summers, where I realized my passion for science and inevitability of graduate school.

I am deeply indebted to the Jensen Lab for teaching me so much. Graduate school was the hardest thing I have ever done, but I cannot believe how much I have learned from you all. You are all brilliant, geek-tastically hilarious, and I am honored to call you friends. I would especially like to thank my advisor, Grant Jensen, for investing in me and from whom I learned a great deal about the scientific method and effective communication. I thank Caltech for spoiling me with amazing research facilities. I also thank my collaborators in the Sundquist, Hope, and Bell Labs, for all of their time, help, and enthusiasm in making our projects successful. A special thank you to Associate Dean, Felicia Hunt, for keeping me sane and taking such good care of me. Caltech is very lucky to have you. And to the rest of my Caltech friends– a sincere thank you for your camaraderie. Though we were working too hard to see each other often, I knew we were

getting through it together and you made me feel “normal,” which is what kept me from quitting all along the way.

To the Mindshare/Phage posse– I could write an entire dissertation about how much you all have changed my life. Graduate school could have been a very lonely time, but you have been my California family and provided so much fulfillment and inspiration. The last few years have been a crazy adventure no one else would believe, and I love you all dearly. There are too many to name individually, but you know who you all are– I will treasure you always. Special thanks to Jason Porath and Jean Choi who made a heroic effort to animate the story of Chapter 1.

Lastly, thank you to my family, to whom I dedicate this thesis– I would be nowhere without your support. Mom, Dad, and Brandon; you are my best friends and I have missed you so much. Thank you for being my loudest cheerleaders, from 3,000 miles away. On my hardest days, of which there were many, it was you who fixed me and picked me back up. It is for you that I look forward to coming home. And to the brilliant Benjamin Solis– you have helped me immensely and I cannot thank you enough for all of your effort. I love you all.

PREFACE

I never had a defining moment when I knew I would be a scientist, but I always had a natural inclination toward it. Science never felt like work, it felt like play; so I knew I would enjoy being surrounded by science at Caltech. What I learned in my first year, however, is that science for fun is not enough. There are an infinite number of interesting questions in this world to keep scientists busy, just for the sake of gaining knowledge. But I learned quickly that knowing things is not satisfying to me unless there is a clear application. So after a year of graduate school had gone by and I had not found my calling, I emailed a handful of professors on campus to ask if *anyone* was studying something related to human disease. Grant Jensen wrote back to say he was working on HIV, and I knew I had found my niche.

I cannot imagine a specimen more interesting than viruses. Viruses (from the Latin word for "poison") are the most abundant type of biological entity. They are not technically classified as living organisms but are so seemingly "smart." They are at the mercy of their environment and yet have been a strong competitor in the game of evolutionary one-upmanship with every other life form. Since beginning my studies of viruses, I have been in constant awe of every detail that makes them so difficult to treat.

Since the day HIV was discovered, a cure has seemed ten years away. Thirty years later, it still seems far off. It has become the worst epidemic in modern human history. It is often discouraging to work on a puzzle that seems to have no solution, but the HIV community is so dedicated and supportive, and I will be proud to say I did my best to help. Learning about the structural biology of the virus has been fascinating and rewarding.

I am confident in the abilities of science to develop more effective treatments and maybe even a vaccine. I am more concerned with the peripheral issues (political, social, and economic) that compound the impact of the disease. For an HIV patient to survive, they need access to clean water and sanitation, sufficient nutrition, frequent visits to a doctor, and effective transportation. These should be universally accessible by all humans for general health. But perhaps the most devastating barrier to eradicating HIV is the stigma directed at patients. This factor makes AIDS a silent killer because people avoid testing or treatment out of fear of discrimination. To avoid social disgrace, some people avoid talking about prevention (most unfortunately, politicians) or taking easy precautions. Education and outreach programs are vital to raising awareness about the disease and methods of transmission, to prevent infection and misinformation that leads to social ostracism. The most successful countries to control the spread of AIDS did so by being honest about transmission andn prevention. For this reason, I will continue to research the molecular biology of HIV, but will focus on education and community outreach in post-PhD life.

ABSTRACT

The Human Immunodeficiency Virus (HIV) depends on the ability to exit infected cells, mature into an infectious state, and infect new host cells. The structural details of exiting and maturation (known as the "late stage events") remain elusive, but further understanding could lead to new therapies. HIV exits cells by hijacking a host cellular complex called ESCRT (Endosomal Sorting Complex Required for Transport), which evolved to constrict membranes in multivesicular body formation and cytokinesis. Electron cryotomography (ECT) was used to gain three-dimensional images of ESCRT in several contexts, including the physiological system of archaeal cell division. This study provided insight into the monomer interactions in the complex and led to a molecular mechanism of membrane constriction.

HIV is released from the cell as an immature particle with the main structural protein, Gag, forming a spherical shell around the RNA genome and enzymes. Gag is then cleaved into several proteins that refold and assemble into the conical capsid that is characteristic of the mature, infectious particle. The capsid is typically a closed cone, but unclosed varieties provide insight to the mechanism of assembly. By combining ECT, computer simulations, and fluorescence light microscopy, we analyzed features of unclosed capsids that suggest a "curling sheet" model of capsid assembly. These studies not only provided novel insight into the late stages of the HIV life cycle, but also contributed to the methods used by electron microscopists and researchers of HIV.

TABLE OF CONTENTS

INTRODUCTION

The Human Immunodeficiency Virus (HIV) is the retrovirus that leads to Acquired Immunodeficiency Syndrome (AIDS). AIDS was first reported in the United States in 1981, and since then, no vaccine or cure has been developed. Current treatments combine classes of drugs that block the virus in different ways to avoid creating strains of HIV that are immune to single drugs. While these drugs can expand a patient's lifespan by decades, they can be expensive, difficult to administer, and cause many side effects. These treatment regimens are therefore not suitable for under-developed countries. HIV is transmitted sexually, through blood-to-blood contact, through sharing needles, and from mother to child during pregnancy or delivery. There are many preventative measures to avoid infection such as condom use and clean needles, but since the beginning of the epidemic, more than 60 million people have become infected and 30 million have died (UNAIDS, 2011). HIV/AIDS has therefore become known as the most severe epidemic in modern times.

HIV/AIDS has been a difficult infection to cure for many reasons. The virus mutates at a high rate due to mistakes made in reverse transcription and no proofreading mechanism (Ammaranond and Sanguansittianan, 2012). For this reason, drug resistance is a common problem during treatment, and patients typically use a cocktail of three different drugs for treatment in order to avoid resistance. Another problem is that HIV inserts its own genome into the host DNA where it can remain dormant for decades, a mechanism called latency (Smith et al., 2012). In this stage, it is invisible to the immune system and any drugs in the body. In certain conditions, the latent virus can reactivate to spread the infection, so if a patient has a stable CD4 T-cell count and stops receiving treatment, the virus can return to kill cells again. One approach to depleting the latent reservoir could be to purposefully trigger the

reactivation of the virus and attack it with a potent drug. More studies need to be performed to learn more about the virus and develop effective drugs.

HIV has only nine genes and therefore relies heavily on the host cell throughout most of its lifecycle. The development of noninfectious but structurally native virus-like particles (VLPs) has allowed researchers to safely study the virus and its interactions with host cells (Young et al., 2006). In order to study the virus/host interactions, a comprehensive center called CHEETAH (Center for the Structural Biology of Cellular Host Elements in Egress, Trafficking, and Assembly of HIV) was developed. Twelve laboratories in the United States, including the Jensen Lab at Caltech, are involved in studying the structural biology of HIV in five different areas: (1) viral RNA and Gag trafficking, (2) virus assembly, (3) virus budding and late restriction, (4) virus structure, and (5) early events and tripartite motif 5-alpha (TRIM5α) restriction. The center met often throughout my PhD, which exposed me to the current research in each of these areas. I focused on viral structure and late events (viral budding and maturation) using electron cryotomography (ECT).

HIV Life Cycle

Knowledge of the HIV life cycle and viral structure are required for the development of effective treatments, but many details remain unknown. The immature particles contain a spherical shell of protein called Gag, and the membrane is coated with envelope protein (Env) spikes, which recognize the host cell's CD4 receptor and co-receptors to initiate viral fusion (Figure I1b). Individual Gag domains are cleaved during maturation and reform to create the conical capsid, which encloses two single strands of RNA and three enzymes (Figure I1c). This mature virion is now infectious.

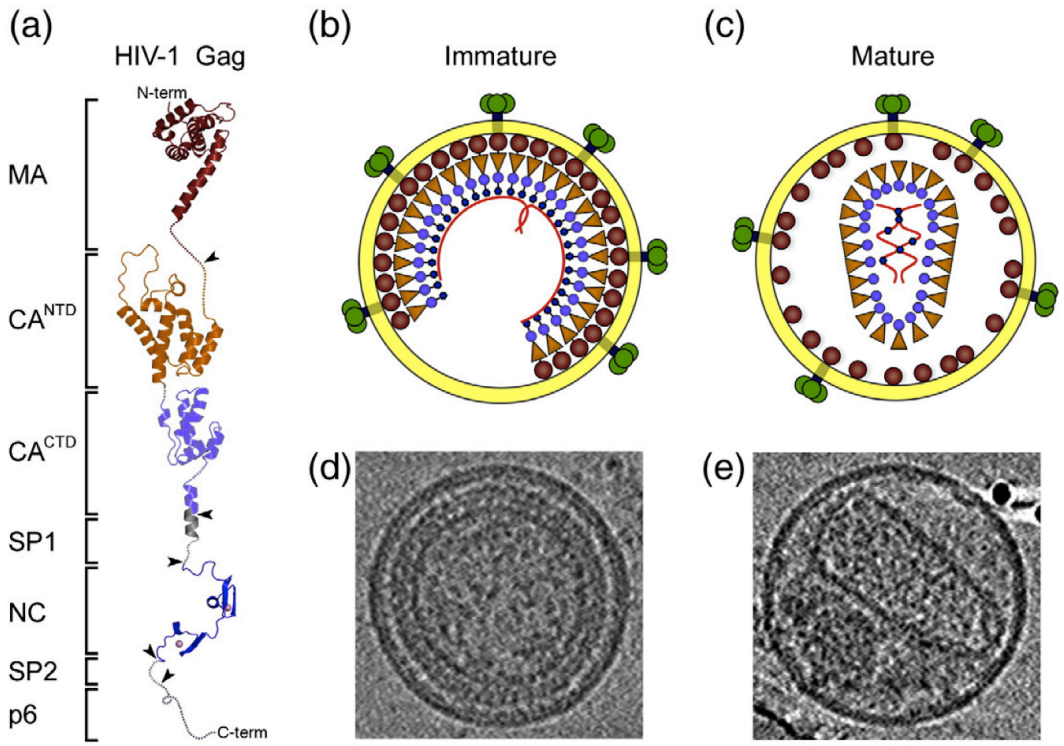

Figure I1. Structure of immature and mature HIV-1 virions. (a) Schematic tertiary structure of Gag domains. Models of immature (b) and mature (c) HIV-1 particles based on corresponding EM images in (d) and (e) of particles preserved in vitreous ice. Reprinted with permission from (Yeager, 2011).

An overview of the HIV life cycle is depicted in Figure I2. The capsid is released into the cell upon fusion, and then the RNA genome is reverse-transcribed into double-stranded DNA and transported to the nucleus for integration. HIV movement depends on the actin and microtubule network and employs the dynein motor protein for directed movement toward the nucleus (Mcdonald, 2002). The viral DNA integrates with the host DNA and is transcribed and translated into viral proteins and transported to the plasma membrane where they reassemble. The virions bud out of the cell and are released as immature, noninfectious particles. They then undergo a maturation process to form the conical capsid and become infectious. Since 2004 when Figure I2 was created, new knowledge has clarified our understanding of the life cycle. It is now thought that the capsid remains intact until it reaches the nucleus, and so reverse transcription occurs

inside the capsid (Arhel, 2010). Also, there are viral regulatory proteins that re-enter the nucleus to promote transcription of viral DNA (Karn and Stoltzfus, 2012). Immediately after transcription, only short mRNAs encoding the viral regulatory proteins Tat and Rev are produced. Tat activates further viral transcription, and Rev promotes export of unspliced mRNAs encoding the structural proteins from the nucleus to the cytoplasm.

Visualizing capsids inside infected cells has been challenging, and capsids are difficult to purify due to their instability, so many of the "deep cell events" remain elusive. For example, when I began my thesis work in 2007, it was unknown whether reverse transcription occurs inside the intact capsids, how and when uncoating of the capsid occurs, and how TRIM5α inhibits capsid function. Much of the evidence is still contradictory, but scientists are now favoring a model that reverse transcription occurs in capsids that remain intact until reaching the nuclear membrane (Arhel, 2010). TRIM5α is a species-specific restriction factor that acts early on the intact capsid (the rhesus monkey version restricts HIV). In 2004, it was thought that TRIM5α restricted infection by binding to capsids to inhibit uncoating (Goff, 2004; Stevenson, 2004), but current evidence indicates that TRIM5α actually promotes rapid and premature uncoating of capsids using the proteasome (Stremlau et al., 2006; Perron et al., 2007; Arhel, 2010; Black and Aiken, 2010). The details of TRIM5α restriction are now better understood from electron crystallography and fluorescence microscopy studies (Campbell et al., 2007; Campbell et al., 2008; Ganser-Pornillos et al., 2011).

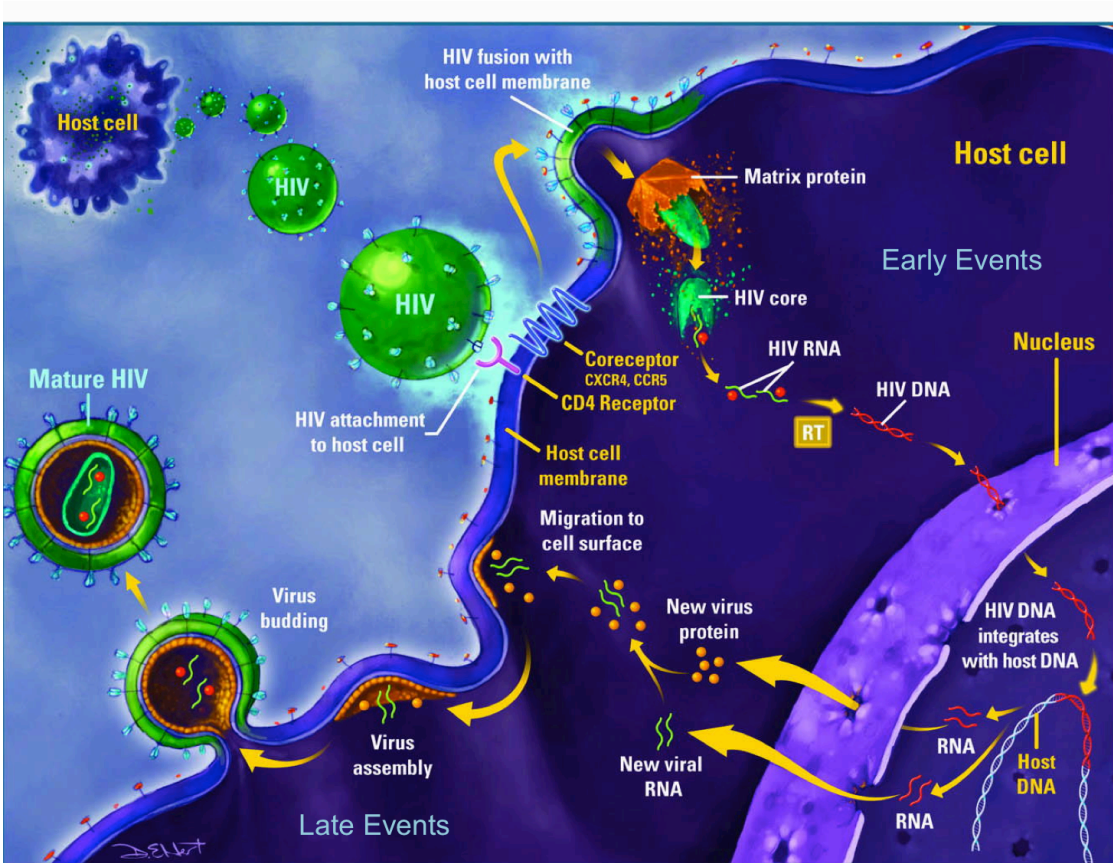

Figure I2: Overview of the HIV Life cycle. Adapted with permission from (depts.washington.edu/hivaids, 2004).

Focus on "Late Events"

The "late events" were the focus of my thesis, and the progress from the last four years will be outlined in the forthcoming chapters. Briefly, the assembling virus buds out of the cell as an immature virus by hijacking a human protein complex called ESCRT (Endosomal Sorting Complex Required for Transport). The ESCRT machinery consists of a family of proteins that is used to bend and constrict membranes in multivesicular body (MVB) formation, cytokinesis in eukaryotes and archaea, and viral budding. While the members of ESCRT were known at the time I began my graduate research, the molecular mechanism explaining the membrane constriction process was poorly

understood. My progress in developing a molecular mechanism, using the archaeon *Sulfolobus acidocaldarius* as a model organism, led to the proposal of an "hourglass" model of constriction (Chapter 1).

Once released, the virus undergoes a maturation process to begin another round of infection. Maturation is initiated by the protease enzyme, which cleaves domains of the structural protein called Gag to produce four new proteins (MA, CA, NC, and p6) (Figure I1a). The fully processed CA and NC proteins reassemble to form the conical capsid, which encapsulates the genome and enzymes. These processing steps were well understood when I began my thesis work, but the progression of forming the capsid remained unknown. Several models exist to try and explain the process of forming a capsid, including building from the wide end (Benjamin et al., 2005), building from the narrow end (Briggs et al., 2006), and building a curled sheet from the side (Levandovsky and Zandi, 2009). By studying the structure of unclosed capsids, I was able to gain insight into the maturation process and support the "curled sheet" model of assembly (Chapter 2).

Electron Cryotomography

Previous studies of HIV using electron microscopy (EM) involved chemically fixed, resin-embedded, and heavy-atom-stained samples (Figure I4b). Those images have greatly impacted our understanding of the viral structure and life cycle, but they were limited in resolution, contained artifacts from preparation, and were only two-dimensional. The development of electron cryotomography (ECT) has allowed important viral structures to be solved using three-dimensional, high-resolution (up to 4 nm) images of samples in a near-native state (Figure I4c).

Specimens are preserved for ECT by first plunge freezing them into a liquid cryogen. I summarized the process and considerations of plunge freezing in a chapter of *Methods in Enzymology* (Dobro et al., 2010) and in Chapter 3.3 here. Successful rapid freezing of the sample results in vitreous ice, which contains no ice crystals and therefore no damage to the specimen. Once in the microscope, targets are chosen and exposed to the electron beam while being rotated around an axis to collect images from multiple

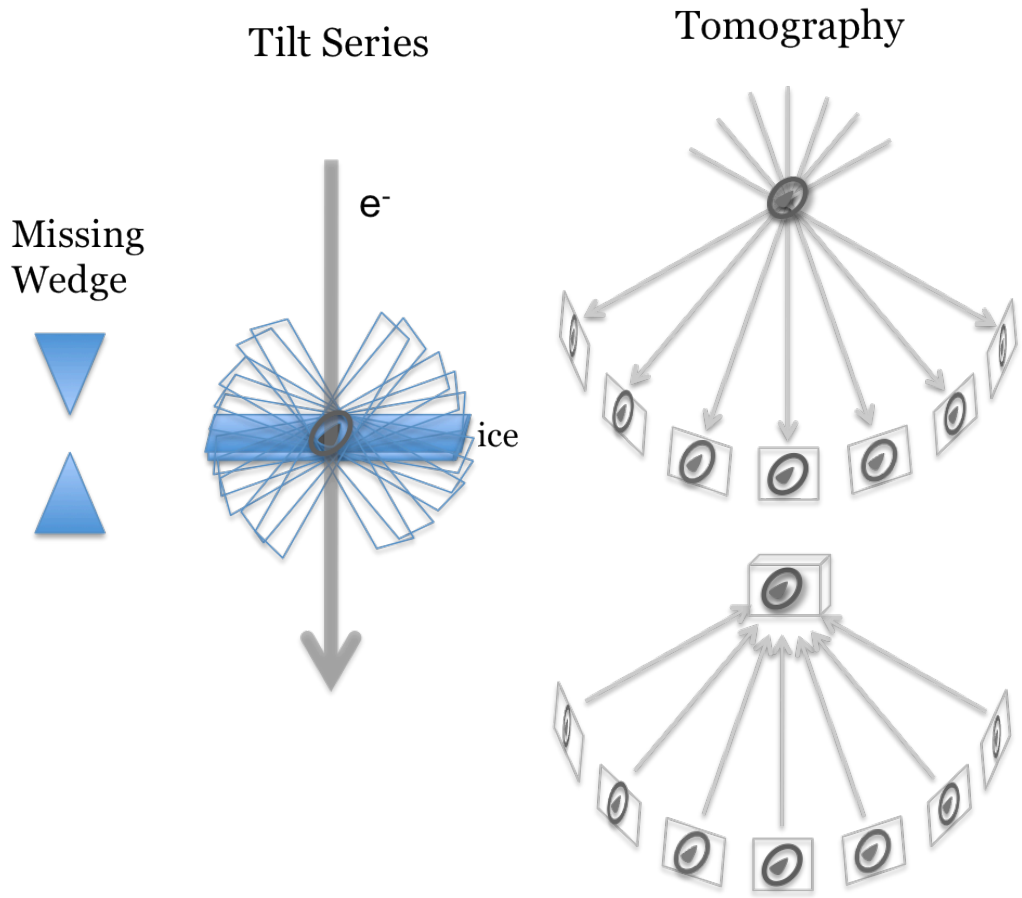

Figure I3: Tomographic Reconstruction. A tilt series is collected by rotating the sample around an axis. An electron beam is passed through the sample and gets scattered by the interaction with the sample's atoms. The images are detected on a CCD camera and recorded as digital images. These images are aligned and calculated into a three-dimensional representation using a back-projection algorithm. Due to the limit of angles the sample can be rotated, there is a "missing wedge" of information on the top and bottom of the resulting tomogram.

directions (tilt series). Stacks of images are then aligned using the positions of colloidal gold clusters in the sample and used to calculate a three-dimensional reconstruction called a tomogram using a back-projection algorithm (Figure I3). The resolution of tomograms depends on the sample thickness, the number of images, the signal-to-noise ratio, and the accuracy of the alignment of images.

There are several challenges of ECT that have limited our progress in the HIV field. First, electrons can only pass through samples less than 1 μm thick. HIV particles are about 120 nm in diameter and so can easily be imaged with ECT. Eukaryotic cells can be many micrometers thick, so only the HIV life cycle events that take place in the thinnest outer edges can be imaged by ECT. Samples could also be prepared for conventional EM and thin-sectioned to access the deeper areas of the cell, but this damages the sample. Additionally, samples can be cryo-sectioned, but this is technically very challenging. During the first half of my PhD, I worked to develop the technique of imaging thin edges of cells on EM grids (Chapter 3.4). Another challenge of ECT is that biological samples are sensitive to the electron beam and are damaged over time. For this reason, a low dose of electrons must be used and so the resulting images are very low in contrast. Also, the limited tilt range of +65° to −65° results in missing information known as the "missing wedge." This limits the resolution of the tomogram in an anisotropic manner. Despite these challenges, high-resolution images of immature and mature HIV have allowed us to gain detailed insight into the structure of HIV and related complexes.

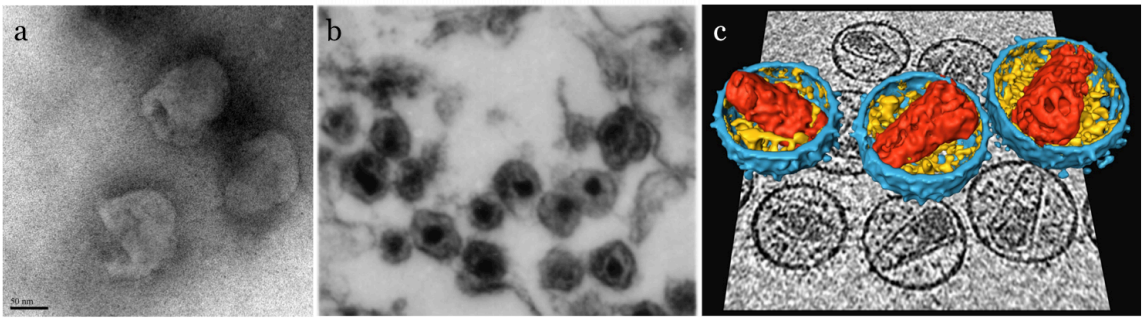

Figure I4: Comparison of electron microscopy methods of HIV particles. (a) Mature HIV particles "negatively stained" using 2% uranyl acetate results in distorted membranes and lack of structural detail. (b) Mature HIV particles prepared by fixing, heavy-atom staining, plastic embedding, and thin sectioning. Spherical particles with dark capsids are visualized with low resolution. Reprinted with permission from Davis et al., 1999. (c) Slices of tomograms of frozen, mature HIV particles and three-dimensional segmentations revealing high structural detail. Reprinted with permission from Briggs et al., 2006.

Summary

I have studied the structural biology of late events in the HIV life cycle using electron cryotomography. I described a new mechanism for membrane constriction by ESCRT using division in archaea as a model (Chapter 1) and I confirmed a "curled sheet" model of assembly for the maturing HIV capsid by analyzing unclosed HIV particles (Chapter 2). Throughout these studies, I contributed to methods such as purification of HIV particles (Chapter 3.2), plunge freezing for tomography (Chapter 3.3), and growing eukaryotic cells on EM grids (Chapter 3.4). I also contributed tomograms of *Helicobacter hepaticus* for publications about chemotaxis (Appendix A) and flagellar motors (Appendix B). These projects have contributed to a greater understanding of the structural components related to HIV budding and maturation.

REFERENCES

Ammaranond, P., and Sanguansittianan, S. (2012). Mechanism of HIV antiretroviral drugs progress toward drug resistance. *Fundam Clin Pharmacol 26*, 146–161.

Arhel, N. (2010). Revisiting HIV-1 uncoating. *Retrovirology 7*, 1–10.

Benjamin, J., Ganser-Pornillos, B. K., Tivol, W. F., Sundquist, W. I., and Jensen, G. (2005). Three-dimensional structure of HIV-1 virus-like particles by electron cryotomography. *Journal of Molecular Biology 346*, 577–588.

Black, L. R., and Aiken, C. (2010). TRIM5alpha disrupts the structure of assembled HIV-1 capsid complexes in vitro. *Journal of Virology 84*, 6564–6569.

Briggs, J. A., Grünewald, K., Glass, B., Förster, F., Kräusslich, H.G., and Fuller, S.D. (2006). The mechanism of HIV-1 core assembly: insights from three-dimensional reconstructions of authentic virions. *Structure 14*, 15–20.

Campbell, E.M., Dodding, M.P., Yap, M.W., Wu, X., Gallois-Montbrun, S., Malim, M.H., Stoye, J.P., and Hope, T.J. (2007). TRIM5alpha cytoplasmic bodies are highly dynamic structures. *Molecular Biology of the Cell*, 10, 2102–2111.

Campbell, E.M., Perez, O., Anderson, J.L., and Hope, T.J. (2008). Visualization of a proteasome-independent intermediate during restriction of HIV-1 by rhesus TRIM5alpha. *Journal of Cell Biology 180*, 13, 549–561.

Davis, D., Yusa, K., Gillim, L.A., Newcomb, F.M., Mitsuya, H., and Yarchoan, R. (1999). Conserved cysteines of the Human Immunodeficiency Virus Type 1 protease are involved in regulation of polyprotein processing and viral maturation of immature virions. *J Virol 73*, 9, 1156–1164.

Depts.washington.edu/hivaids (2004). HIV Web Study, U. Washington.

Dobro, M.J., Melanson, L.A., Jensen, G., and McDowall, A.W. (2010). Plunge freezing for electron cryomicroscopy. *Meth Enzymol 481*, 63–82.

Ganser-Pornillos, B.K., Chandrasekaran, V., Pornillos, O., Sodroski, J.G., Sundquist, W.I., and Yeager, M. (2011). Hexagonal assembly of a restricting TRIM5alpha protein. *Proc Natl Acad Sci* USA *108*, 534–539.

Goff, S.P. (2004). HIV: Replication trimmed back. *Nature 427*, 791–793.

Karn, J., and Stoltzfus, C.M. (2012). Transcriptional and Posttranscriptional Regulation of HIV-1 Gene Expression. *Cold Spring Harb Perspect Med 2*, 1–17.

Levandovsky, A., and Zandi, R. (2009). Nonequilibirum assembly, retroviruses, and conical structures. *Phys Rev Lett 102*, 198102-1–198102-4.

Mcdonald, D. (2002). Visualization of the intracellular behavior of HIV in living cells. *The Journal of Cell Biology 159*, 441–452.

Perron, M., Stremlau, M., Lee, M., Javanbakht, H., Song, B., and Sodroski, J. (2007). The human TRIM5alpha restriction factor mediates accelerated uncoating of the N-tropic murine leukemia virus capsid. *Journal of Virology 81*, 2138–2148.

Smith, M.Z., Wightman, F., and Lewin, S.R. (2012). HIV reservoirs and strategies for eradication. *Curr HIV/AIDS* Rep *9*, 5–15.

Stevenson, M. (2004). TRIMming HIV-1's mainsail. *Nat Immunol 5*, 355–356.

Stremlau, M., Perron, M., Lee, M., Li, Y., Song, B., Javanbakht, H., Diaz-Griffero, F., Anderson, D.J., Sundquist, W.I., and Sodroski, J. (2006). Specific recognition and accelerated uncoating of retroviral capsids by the TRIM5alpha restriction factor. *PNAS 103*, 6, 5514–5519.

UNAIDS (2011). AIDS at 30: Nations at the crossroads. Joint United Nations Programme on HIV/AIDS. http://www.unaids.org/unaids_resources/aidsat30/aids-at-30.pdf.

Yeager, M. (2011). Design of in vitro symmetric complexes and analysis by hybrid methods reveal mechanisms of HIV capsid assembly. *Journal of Molecular Biology 410*, 534–552.

Young, K.R., McBurney, S.P., Karkhanis, L.U., and Ross, T.M. (2006). Virus-like particles: designing an effective AIDS vaccine. *Methods 40*, 98–117.

CHAPTER 1:

STRUCTURE OF THE ESCRT COMPLEX

1.1

INTRODUCTION

For HIV particles to be released from host cells, they hijack the human complex of proteins called ESCRT (Endosomal Sorting Complex Required for Transport). ESCRT is typically used for membrane constriction in multivesicular body formation and cytokinesis in eukaryotes and archaea. The protein family members and interactions are well characterized (Morita and Sunquist, 2004), but the molecular mechanism remains unclear. Several models have been proposed, but evidence is contradictory, and ESCRT has never been imaged with high resolution in a physiological system. In this chapter, I discuss our analysis of the ESCRT structure using evidence from electron cryotomography of *in vitro* assemblies and dividing archaeal cells. Our observations led to a molecular mechanism called the "hourglass" model and may have broad implications in our understanding of cell biology. Chapter 1.2 is the manuscript that will be submitted for peer review. Additional figures that will not be submitted for publication are included in Chapter 1.3 for reference.

This work invites many follow-up experiments to provide more solid evidence that the cytokinetic belt observed in archaea is ESCRT; to characterize the belt in other species, including human cells; and to compare the ESCRT complex in other contexts. A few experiments were conducted to approach these open topics and are outlined in Chapter 1.4.

REFERENCES

Morita and Sunquist. (2004) Retrovirus Budding. *Annu. Rev. Cell. Dev. Biol.* **20** (1) 395–425.

1.2

MOLECULAR MECHANISM OF ARCHAEAL CELL DIVISION BY ESCRT

Megan J. Dobro[1], Rachel Y. Samson[2], Zhiheng Yu[1,3], John McCullough[4], H. Jane Ding[1], Parkson Lee-Gau Chong[5], Stephen D. Bell[2], Grant J. Jensen[1,6*]

[1]Division of Biology and [6]Howard Hughes Medical Institute, California Institute of Technology, 1200 E California Blvd, Pasadena, CA, 91125, USA

[2]Sir William Dunn School of Pathology, South Parks Road, Oxford OX1 3RE, UK

[3]present address: CryoEM Shared Resources, Janelia Farm Research Campus, HHMI, 19700 Helix Drive, Ashburn, VA, 20147, USA

[4]Department of Biochemistry, University of Utah, 15 N Medical Drive, East RM 4100, Salt Lake City, UT, 84112-5650, USA

[5]Department of Biochemistry, Temple University School of Medicine, 3420 N. Broad Street, Philadelphia, PA 19140, USA

*correspondence: jensen@caltech.edu, 626-395-8827

Summary

The endosomal sorting complex required for transport (ESCRT) is evolutionarily conserved from archaea to eukaryotes. The complex drives membrane scission events in a range of processes including cytokinesis in metazoa and some archaea. Using electron cryotomography (ECT) we reveal that several human ESCRT-III proteins self-assemble into nested tubes and cones *in vitro*. Furthermore, we find that the archaeal ESCRT-III recruiting protein, CdvA, polymerized into helical filaments on liposomes. These *in vitro* assemblies revealed surprisingly versatile monomer interactions including filament formation and filament coiling. To observe ESCRT assemblies in a physiological context, we used ECT to image *Sulfolobus acidocaldarius* and observed a distinct protein belt at the leading edge of division furrows in constricting cells. The known dimensions of ESCRT-III proteins constrain their possible orientations within each of these structures and lead to an "hourglass" model of how ESCRT proteins drive membrane scission in dividing archaeal cells.

Introduction

The endosomal sorting complex required for transport (ESCRT) is a set of proteins that bend and separate membranes. ESCRT-mediated membrane scission is a highly-conserved process involved in cytokinesis in eukaryotes and archaea, multivesicular body (MVB) formation, and viral budding (reviewed in: Hurley, 2010; Morita and Sundquist, 2004; Wollert et al., 2009b). In MVB formation, ESCRT-I and -II deform the membrane to form buds, ESCRT-III cleaves the buds, and Vps4 (written "Vps4" in yeast and "VPS4" in humans), a AAA+ ATPase and the only enzyme in the system, recycles ESCRT-III for additional rounds of budding (Wollert and Hurley, 2010).

While the molecular mechanisms that drive membrane deformation and cleavage by the ESCRT machinery remain unclear, several models have been proposed. In 2008, Hanson et al. used “deep-etch” electron microscopy to visualize the plasma membrane of cells overexpressing ESCRT-III proteins and found circular arrays of filaments (Hanson et al., 2008). In 2009, Wollert et al. reconstituted ESCRT-III-driven membrane constriction *in vitro* on giant unilamellar vesicles (Wollert et al., 2009a), showing that ESCRT-III proteins in high concentration were sufficient to produce intralumenal vesicles. These two studies led to the model of scission known as “spiral constriction” (Hanson et al., 2009; Wollert et al., 2009a). In this model, ESCRT-III filaments form a flat spiral on a membrane that grows (polymerizes) and coils inward, pinching out a membrane bud. Vps4 was apparently recruited to recycle ESCRT-III subunits for further rounds of budding, but was not necessary for the actual mechanism of budding (Wollert et al., 2009a). The related “dome" model is based on ESCRT-III’s ability to form dome-shaped caps *in vitro* (Lata et al., 2008b), suggesting that as ESCRT-III coils, it forms a dome rather than a flat coil as it pinches membranes (Fabrikant et al., 2009).

A third model arose from the work of Saksena et al., who used fluorescence spectroscopy to determine the order that yeast ESCRT components assemble on the membrane (Saksena et al., 2009). They found that ESCRT-III binds to the ESCRT-II complex and oligomerizes on the membrane into a filament. They also showed that other ESCRT-III proteins cap the filament and recruit the AAA+ ATPase, Vps4, which disassembles the filament. These observations led to the “purse string" model in which the ESCRT-III filament forms a ring or spiral that is disassembled by Vps4 from one end. The disassembly causes a decrease in the circumference of the ring, much like pulling the drawstring on a purse would close the opening. In this model, Vps4 drives constriction and is therefore vital to the molecular mechanism.

Recently, a fourth model was proposed based on SAXS data that showed the ESCRT-I/-II supercomplex has an arched shape (Boura at el., 2012). In this model, a "whorl" of ESCRT-III is created and Vps4 may promote filament self-association to deform the membrane into a dome-shape. For this reason, the whorl model is considered a modified dome model, and the ESCRT-III filaments form lengthwise along the neck of the budding vesicle rather than perpendicular to the neck growth as other models predict.

Electron microscopy (EM) has been used in attempts to visualize the structure of ESCRT assemblies in several systems. Overexpression of ESCRT-III proteins in eukaryotic cells resulted in spiral-shaped structures (Bodon et al., 2011; Hanson et al., 2008) and ring-shaped densities were observed in HIV buds arrested in cells lacking some ESCRT-III components (Morita et al., 2011). Guizetti et al. used tomography to obtain three-dimensional EM images of the cytokinetic "midbody" in eukaryotic cells and found 17-nm-thick helical filaments (Guizetti et al., 2011). The composition of the observed filaments remains unclear, however, since 17 nm is much thicker than any filaments formed by ESCRT proteins imaged previously (Bajorek et al., 2009b; Bodon et al., 2011; Hanson et al., 2008; Lata et al., 2008b; Morita et al., 2011). While fixing, staining, and sectioning can lead to artifacts and distortions, electron cryotomography (ECT) of plunge-frozen samples can be used to obtain three-dimensional images of certain intact cells in a near-native state (Gan and Jensen, 2012). ECT has been used to analyze HIV-1 budding sites in human cells, for instance, but curiously no structure was found that could be attributed to the ESCRT machinery (Carlson et al., 2010). Due to these inconsistent results, the structure and mechanism of ESCRT complexes in cells remain elusive.

More success has been found in imaging ESCRT proteins *in vitro*. In humans, ESCRT-III proteins are called charged MVB proteins (CHMPs) and increased sodium

tolerance-1 (IST1). CHMP2 and CHMP3 together form helical tubes *in vitro* (Bajorek et al., 2009b; Lata et al., 2008b). X-ray crystal structures revealed protein packing that involved multiple dimer interactions (Muziol et al., 2006). These structures were fit into the helical tubes observed by ECT to suggest that monomers interact roughly lengthwise to form filaments of the 1-start helix (Lata et al., 2008b). The IST1 N-terminal domain is structurally similar to other CHMPs (Xiao et al., 2009; Bajorek et al., 2009b) and has been suggested to play a dual role in regulating Vps4-recycling of ESCRT-III: it recruits Vps4 to the ESCRT machinery for depolymerization, but also negatively regulates Vps4 by forming a heterodimer with it in the cytoplasm to block binding with ESCRT proteins (Dimaano et al., 2008). CHMP1B has also been shown to recruit VPS4 to depolymerize the complex (Bajorek et al., 2009a; Stuchell-Brereton et al., 2007). One common property of ESCRT-III proteins is their ability to polymerize *in vitro*. Variations of CHMP1A, CHMP2A, CHMP3, CHMP4B, and IST1 have assembled into helical filaments, tubes, and cones, but it is unclear how the monomers polymerize to form these assemblies (Bajorek et al., 2009b; Lata et al., 2008b; Pires et al., 2009). In order to understand how various ESCRT-III monomers interact with each other, we used ECT to analyze assemblies of the IST1 N-terminal domain, CHMP2A/3 complexes, and CHMP1B. We find that all three of these ESCRT-III proteins, and therefore likely the entire ESCRT-III family, form filaments that wrap helically into cones or tubes with non-specific lateral and radial contacts.

In order to gain additional insight, we sought to image the ESCRT complex *in vivo*. Because human cells are typically too thick to image with ECT, a thinner sample was sought. In 2008, it was shown that the archaeal species *Sulfolobus acidocaldarius* uses ESCRT homologs for cell division (Samson et al., 2008), and it has since been shown that these homologs are conserved throughout the Crenarchaeal kingdom (Ellen et al., 2009; Lindås et al., 2008; Makarova et al., 2010). Archaea like *S. acidocaldarius*

average about a micrometer in diameter and are therefore more suitable for ECT. Crenarchaea contain ESCRT-III and Vps4 homologs (Samson et al., 2008; Lindås et al., 2008), and also have a unique cell division protein, CdvA, which contains a membrane binding domain that is predicted to be largely alpha-helical in nature (Samson et al., 2011). CdvA recruits ESCRT-III to the membrane, serving a function similar to ESCRT-I and -II in eukaryotes (Samson et al., 2011). To withstand extreme conditions, the membranes of thermoacidophilic archaea like *S. acidocaldarius* contain bipolar tetraether-linked lipids (Zhai et al., 2012). A major component of these lipids, called polar lipid fraction E, can form liposomes of varying sizes. Negative stain EM revealed that CdvA gave rise to a lattice-like structure on the surface of the liposomes. ESCRT-III alone did not bind to liposomes, but once recruited by CdvA led to substantial deformation (Samson et al., 2011). Here we show cryotomograms of CdvA polymerized on membranes. Like human ESCRT-III, CdvA formed filaments of similar dimensions that wrapped helically around liposomes.

Previous immunofluorescence studies have shown that all three archaeal components (ESCRT-III, CdvA, and Vps4) localize to the mid-cell during cell division and form a cytokinetic ring (Samson et al., 2008; Samson et al., 2011). By imaging plunge-frozen, dividing *S. acidocaldarius* cells with ECT, we were able to visualize the three-dimensional architecture of this ESCRT system throughout cell division. We show that ESCRT-III polymers, assembled both *in vitro* and in the division complex in *S. acidocaldarius* cells, form both tubular and conical assemblies. These advances point to a dome-like "hourglass" model for ESCRT-driven cell division.

Results and Discussion

In vitro assemblies of ESCRT-III

Purified human ESCRT-III proteins were assembled (see Materials and Methods), and the assemblies were then either negatively stained or plunge-frozen for electron microscopy. Mixtures of truncated CHMP2A and CHMP3 have previously been shown to form 1-start helices, at times terminated by dome-like caps, as well as loose spirals and cones (Bajorek et al., 2009b; Lata et al., 2008b). Using full-length proteins, our negative stain images confirm those results, showing both tubes and cones with striations. In one case, a cone was observed nesting inside another cone (Figure 1.1A). The existence of cones reveals that the lateral contacts must be non-specific, since each turn has a different circumference in a cone, so monomers in adjacent turns cannot all be in a single register. The observation of nesting is important since the radius of each concentric helix is different, each must contain different numbers of monomers per turn, so radially-adjacent monomers also cannot be in a single consistent register, and the radial contacts must therefore be non-specific as well (Figure S1). This is a rare type of protein interaction, but has been reported before in the protein of the basal disk of the bacterial flagellar motor (Engelhardt et al., 1993).

The IST1 N-Terminal Domain (NTD) formed hollow tubes with different inner and outer diameters (Figure 1.1B). Side views of tubes in negative stain showed striations spaced 5 nm apart and oriented about 13˚ away from perpendicular to the long axis of the tubes (all measurements reported are from density "peak" to "peak", since these are reliable in EM images but the exact position of the edges of densities are not). Tomographic slices perpendicular to the long axis of tubes exhibited concentric rings spaced 3.5 nm apart radially (Figure 1B, top view). (Note that because of the complex point-spread-function, which includes effects of both defocus and the "missing wedge" of data, densities are surrounded by fringes, which have the effect here of emphasizing the outermost and innermost rings and suppressing the contrast of the middle rings. In addition, the "missing wedge" of data reduces the resolution in the direction parallel to

the beam, obscuring the rings across the "top" and "bottom" of the tubes). IST1 therefore likely forms nested helices as well. According to these dimensions, IST1 monomers bind each other roughly lengthwise (to form a filament), laterally (between the coils of each helix), and radially (to the helix of just smaller or just larger radius). Again, the nested helices suggest a non-specific radial interaction between monomers.

CHMP1B formed long tubes with "barbed" variable outer diameters but a consistent 12-nm-diameter hollow inner channel, with clear striations 4.7 nm apart along the long axis (Figure 1.1C upper and lower left). Several short tubular segments froze perpendicularly to the EM grid, providing views down the long axis. Such views exhibited "bull's-eye" patterns of concentric rings 3 nm apart radially (Figure 1.1C upper right and Figure S1). Careful segmentation revealed that the structures were 1-start helical ramps (as in a parking garage for example) rather than stacks of independent disks (Figure 1.1C lower right and Movies 1.1 and 1.2). CHMP1B tubes were barbed, however, exhibiting gradual changes in outer diameter. Such decreases in diameter could be due to outer helices terminating, revealing smaller helices within, but because there did not appear to be uniform radial steps, and in analogy to CHMP2A/3, the barbs more likely represent helical cones. The bull's-eye patterns of concentric rings and segments of the tubes with constant diameter however suggest that CHMP1B also forms concentric cylindrical helices. (Projections down the axis of a cone with a decreasing diameter do not exhibit distinct circular rings when viewed from the top because each new turn of the helix overlaps with the previous turn, so there is no gap created between layers.) The simplest interpretation is that individual filaments form cylinders and cones in different regions as illustrated in Figure 1.1C upper middle.

The dimensions of the known crystal structure of CHMP3 are about 2.5 nm × 3.5 nm × 7.1 nm (Muziol et al., 2006; Bajorek et al., 2009b). Because the structures of all CHMP family members are predicted to be very similar, these dimensions can be used to

constrain the possible orientations of the monomers within the filaments. The two different types of dimer contacts present in the X-ray crystal structures demonstrate the diversity of monomer interactions, reproduced in Figure S2. Lata et al. fit these dimer pairs into their EM map of CHMP2AΔC/3ΔC, suggesting that dimers can bind roughly lengthwise to form the filaments of a 1-start helix (Lata et al., 2008b). Orange pill shapes will be used in several figures to represent the scale of the repeating unit, with the proposed membrane-binding region shown as a black line for lengthwise or top views, and black dots in end-on views. The pitch of the CHMP1B tubes is 4.7 nm from the side view, and the radial distance between nested helices (rings in the bull's-eye patterns) is 3 nm. The 7.1-nm-long axis of the monomers cannot be perpendicular to the filament axis since it is too long. The monomers fit well into the filaments if they bind roughly lengthwise, but no more detail about the orientation of the monomers and their packing is discernable in these images. Importantly, the presence of stacked cones and nested cylinders again reveals that CHMP1B filaments bind non-specifically both radially (Figure S1) and laterally. There must be flexible diagonal contacts as well in the transition between tubes to cones, as demonstrated by the positioning of black circles in the Figure 1.1C illustration.

In summary, IST1, CHMP2A/3, and CHMP1B (and therefore probably all ESCRT-III-like proteins) can form nested helices *in vitro*. CHMP2A/3 and CHMP1B also form cones. Our interpretation is that ESCRT-III monomers form slender helical filaments with non-specific lateral and radial contacts.

CdvA-coated liposomes

In the archaeon *Sulfolobus acidocaldarius,* the ESCRT-like protein CdvA recruits ESCRT-III to the mid-cell membrane for constriction (Samson et al., 2011). Purified

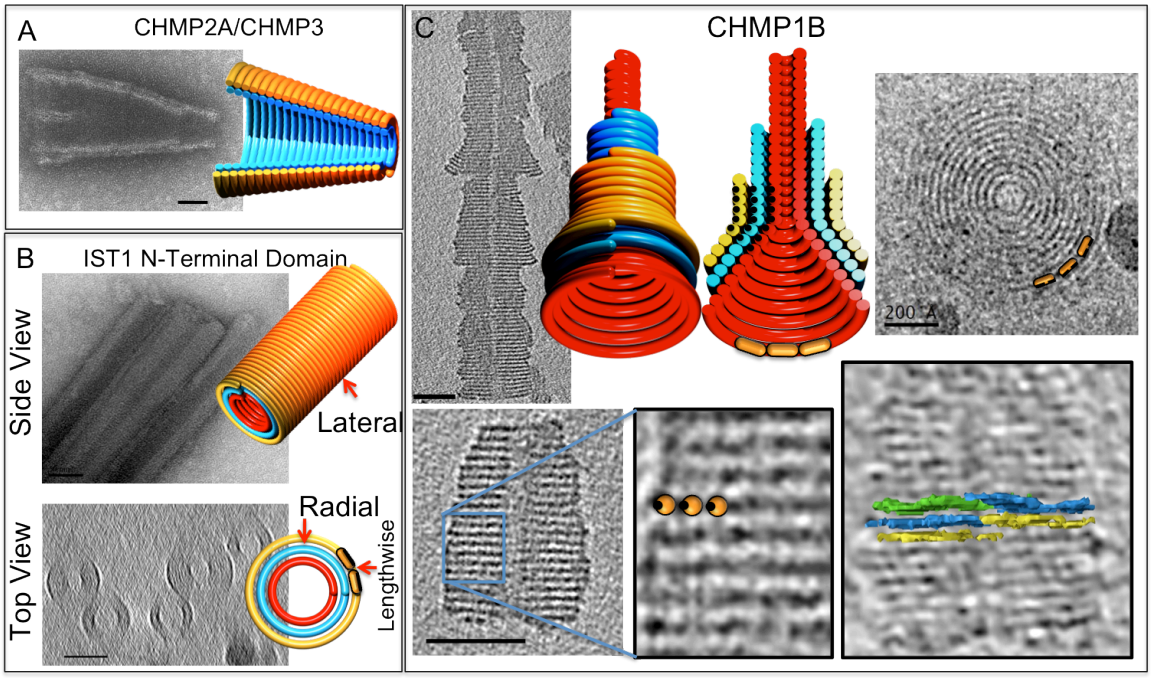

Figure 1.1. Electron microscopy of human ESCRT-III reveals tubes and cones *in vitro*. Illustrations in red, blue, and orange show our three-dimensional (3D) interpretation. (A) Mixtures of full length CHMP2A/CHMP3 as seen by negative stain in 2D. (B) 2D projection, negative stain image of IST1 N-Terminal Domain (Side View) and a slice through a cryo EM 3D tomogram (Top View). (C) Cryo EM images of assembled CHMP1B; Side view (upper and lower left) with a magnified inset (lower middle) and end-on view (upper right) of tomographic slices containing orange pill shapes to represent the dimensions of the repeating unit. The dashed black line or circle drawn inside the pill shapes represents the likely membrane-binding region. Illustrations showing segmentation of layers of the CHMP1B cone (lower right) and an illustration depicting CHMP1B assemblies as helical filaments of decreasing diameter (cones) or consistent diameter (tubes) (upper middle) are also shown. All scale bars are 50 nm unless otherwise noted.

CdvA did not assemble by itself, but in the presence of lipids it formed filaments (Figure 1.2 and Movie 1.3). Liposomes were made of a major component of tetraether lipids called polar lipid fraction E that were isolated from *S. acidocaldarius*. Slender CdvA filaments wrapped around liposomes in helices with a spacing of about 8 nm. As a

control, plain liposomes without CdvA were imaged, but no wrapping filaments were ever seen, supporting the interpretation that the filaments were in fact CdvA. Archaeal CdvA contains a predicted α-helical membrane-binding domain analogous to human

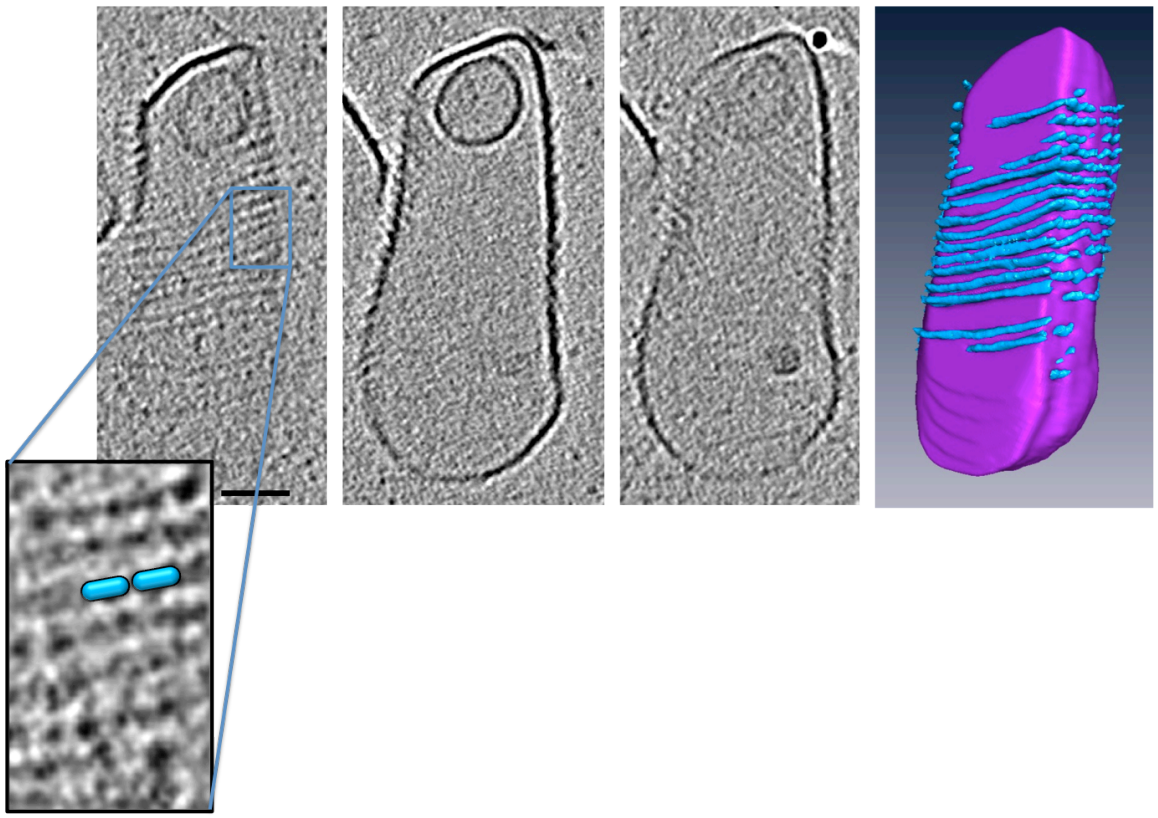

Figure 1.2. Tomographic slices through a liposome wrapped with CdvA filaments. Purified CdvA was added to tetraether liposomes and formed filaments around the liposomes with an 8-nm-spacing from peak to peak. Three planes of one liposome are shown- the top, middle, and bottom. The liposome and filaments were segmented to view in three dimensions. The dimensions of the CHMP3 repeating unit were oriented in the filaments based on size (blue pill shape). The rotation and binding interaction are unknown, but monomers are likely binding roughly lengthwise along the filaments since perpendicularly would not fit. Scale bar is 50nm.

ESCRT-III and therefore may be structurally similar. The dimensions of the crystal structure fit well within the helical filaments of CdvA. The increased spacing of the filaments (from 4.7 nm to 8 nm) may be due to the presence of the membrane.

Dividing Sulfolobus

Sulfolobus acidocaldarius cells flattened somewhat on EM grids and were therefore small enough to be imaged intact. Cells were synchronized for division as previously described (Duggin et al., 2008) and plunge-frozen at the time of division (as determined by flow cytometry). Tilt series were collected of 12 dividing cells and 159 non-dividing cells. The dividing cells exhibited different degrees of ingression, ranging from un-constricted (1.6 μm remaining to divide) to nearly divided (362 nm remaining to divide)(Figure 1.3). In each dividing cell, the ingressing membrane was coated with a belt approximately 3.5-nm thick, 150–400 nm wide, and spaced from the membrane about 6 nm into the cytoplasm. Though the belts likely wrapped around the entire circumference of the cells, they were obscured across the tops and bottoms of the cells due to the missing wedge (Figure 1.3 and Movie 1.4). As cell division progressed (measured by the distance between opposing cleavage furrows) the width of the belt increased (Figure 1.4A), but its thickness remained constant. The total surface area of the belt decreased (Figure 1.4B), however, indicating a net loss of material from the belt. The curvature across the width of the belt also increased as the cell progressed through division and the membrane folded more deeply. Interestingly, the cleavage furrow was always more advanced and differently shaped on one side of the cell than the other, suggesting flexibility. This was the case in cells prepared by traditional methods (fixed, embedded, and sectioned) as well, so it is not likely an artifact of flattening during plunge-freezing. The S-layer was often incomplete at the site of ingression, and many budding vesicles were observed on the side of the cells, adjacent to the ingression site where the membrane is at maximum curvature.

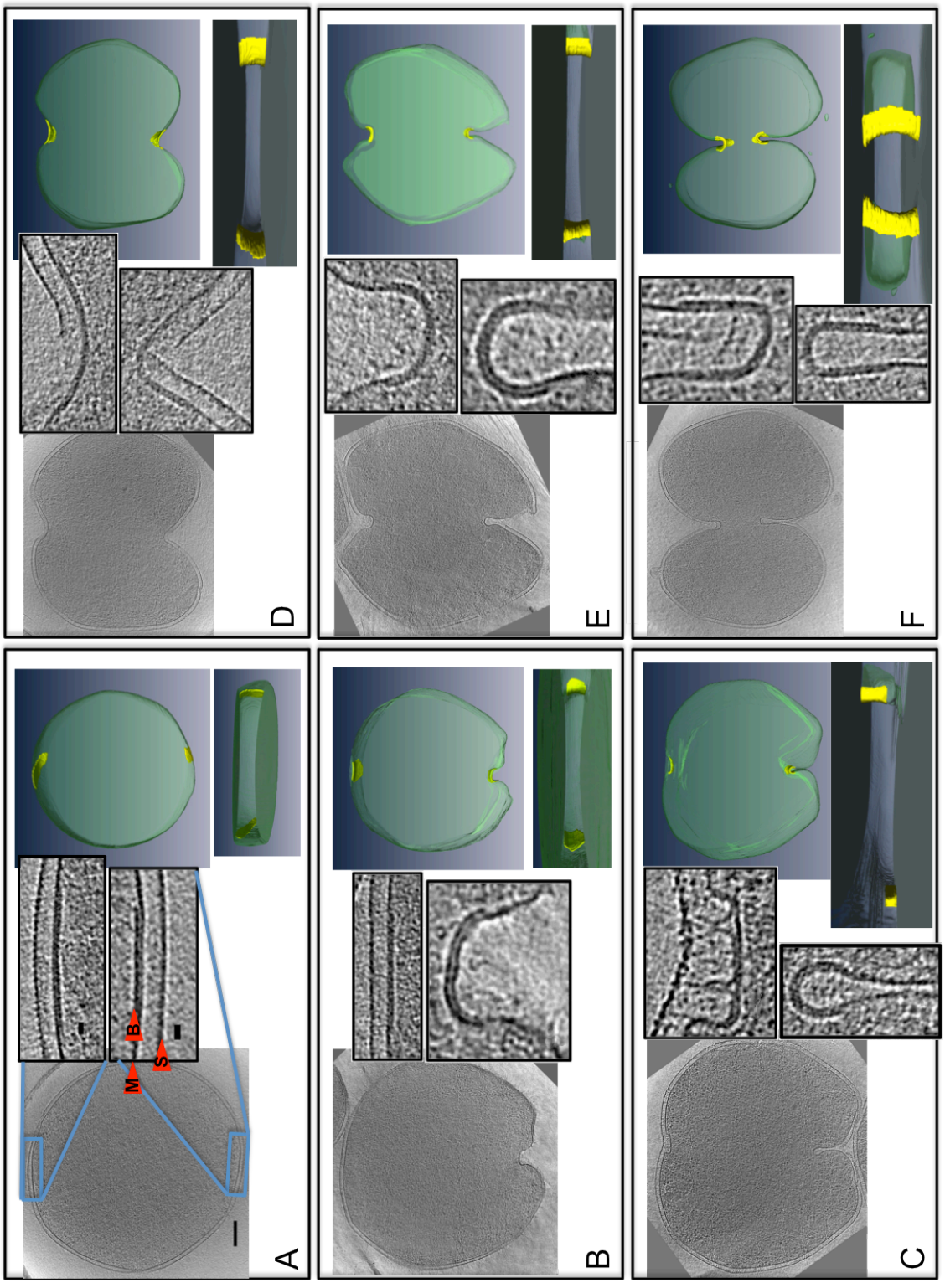
A
B
C
D
E
F
M
B
S

Figure 1.3. Montage of dividing *Sulfolobus acidocaldarius* cells. Panels show from left to right: central slices through tomograms; insets of magnified division furrows revealing protein density on the membrane; and top and side views of segmentations of the cell membrane and protein density. Scale bars are 200 nm for the whole cells, and 20 nm for the insets. (A) A non-dividing cell containing a flat band of protein. The three layers of the insets shown are the belt ("B"), membrane ("M"), and S-layer ("S"). (B) A cell that has begun division, showing ingression on one side only. (C) A cell that shows one side ingressing deeper into the cell with a small radius of curvature and the other side still very shallow and flat. The segmentation shows one side higher than the other because half of the cell was laying on top of carbon while the other side was in a hole. This created a steep incline of membrane facing the electron beam, so the protein could not be observed from top to bottom due to the missing wedge. (D – F) Cells further along in the division process with both sides ingressing and becoming more narrow.

The simplest interpretation is that this belt is the archaeal ESCRT system for cell division. Immunofluorescence studies have shown that the ESCRT system localizes to a ring at the mid-cell region specifically during division (Samson et al., 2011). The belt was present in every dividing cell imaged but only one non-dividing cell (out of 159), and it is likely that the one non-dividing cell containing this protein density was preparing to divide. Additionally, other species of archaea and bacteria that do not divide using the ESCRT system have not exhibited this structure when dividing (Li et al., 2007; Tocheva et al., 2011).

Our working hypothesis is that the belt consists of helical filaments wrapped around the cytokinetic ring in dividing cells. It is unknown how ESCRT-III and CdvA are oriented with respect to each other and the membrane, but since CdvA recruits ESCRT-III to the membrane, one likely scenario compatible with the observed structures is that it lies between the other two (Figure 1.5). Since ESCRT-III paralogs can bind to each other (Samson et al., 2008), it is not necessary that CdvA binds to every ESCRT-III. CdvA and ESCRT-III are not likely to be on the same plane within the belt, since it is

unclear how CdvA would then bind the membrane (too far away). If they were on the same plane directly against the membrane, no gap would have been seen between the membrane and protein belt. The *in vitro* assemblies proved that ESCRT proteins interact radially to form nested assemblies (Figure 1.1), consistent with our hypothesis that ESCRT-III filaments are binding CdvA which are binding the membrane.

If this belt is the ESCRT machinery as we have suggested, it is puzzling why no such belt has been observed at sites of viral budding in wildtype cells (Gelderblom et al., 1989, Carlson et al., 2010). Eukaryotic cells are significantly thicker and the resolution of previous ECT studies may conceivably have been too poor, but this seems unlikely since the studies targeted budding sites at the thin edges of cells. Fixed, embedded, and sectioned cells are thinner, but structural details are often lost in these preparative procedures. It is known for example that several bacterial cytoskeletal filaments are not preserved by these methods (Pilhofer et al., 2010). Since ESCRT-III proteins are about 2 nm wide, and there may only be a few turns of the filament needed to constrict the small neck of viral buds, the density may be too small to resolve with ECT. Since human ESCRT-III can bind to membranes directly (no requirement for ESCRTI-II/CdvA), it could possibly have also been too close to the membrane to be resolved by ECT (Figure S3). The CdvA spacer in *Sulfolobus* may have enhanced the visibility of the ESCRT-III belt here.

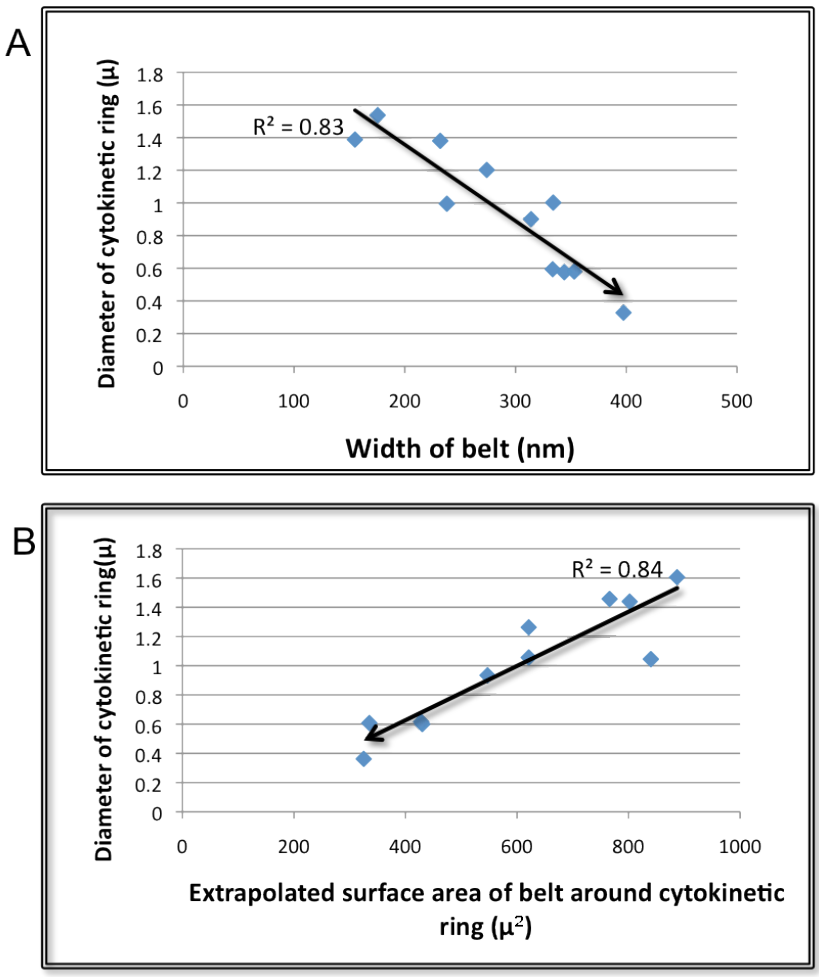

Figure 1.4. Cytokinetic ring loses material as division progresses. "Progression" was measured based on the diameter of the cytokinetic ring. As the ring diameter decreased, the protein belt lengthened (A) but the total surface area of the belt decreased (B).

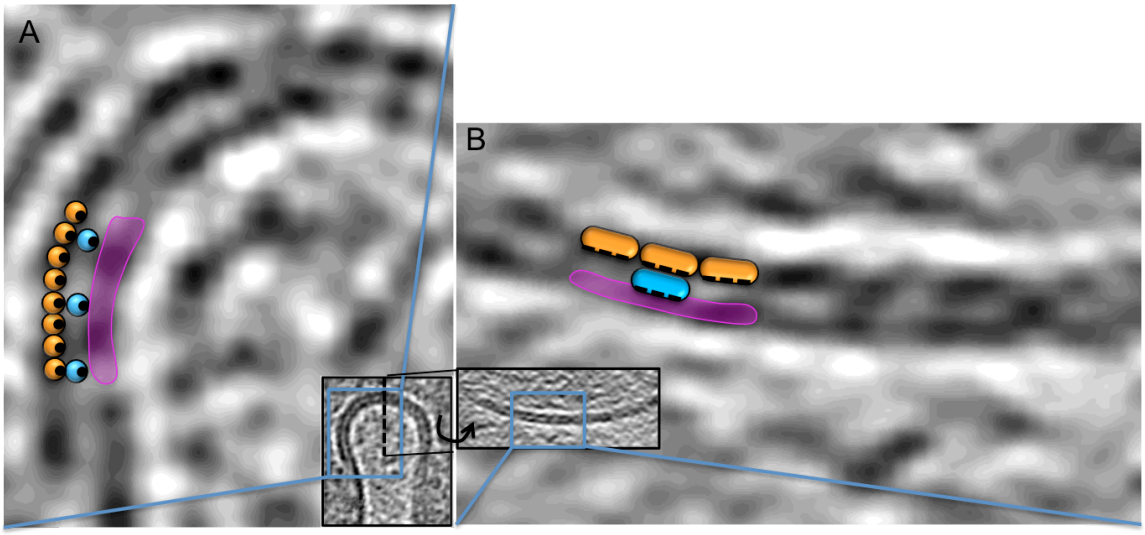

Figure 1.5. Possible orientations of monomers to form wrapping filaments in the cytokinetic belt. (A) A tomographic slice through a dividing cell and the protein belt were enlarged to orient the protein monomers. Part of the membrane layer is highlighted in purple. The crystal structure of ESCRT-III was fit into the EM density based on size. If the filaments are wrapping around the cell to form the belt, this angle views the filaments head-on. The rotation and interactions are unknown, so the size is shown as circles and the direction of the membrane is shown by the black dot. Both CdvA and ESCRT-III must fit to build the cytokinetic belt, and since CdvA recruits ESCRT-III to the membrane, it is likely between them. ESCRT-III paralogs can bind each other and therefore would not require CdvA to bind every ESCRT-III. CdvA and ESCRT-III must not be on the same plane since CdvA would be too far away to bind the membrane. (B) The protein belt was rotated 90° around the Y-axis to show the filaments lengthwise wrapping around the cell from left to right. Here, the direction of the membrane is shown as black lines. These interactions are similar to the nesting assemblies seen *in vitro*.

Molecular Mechanism

Previously proposed models of ESCRT-driven membrane division do not agree well with the structures observed here in *S. acidocaldarius*. The “spiral constriction” model predicts that a flat spiral of ESCRT would form a flat ingressing membrane on one side of the division ring. Only this flat side would be coated with protein (Figure 1.6A). The “purse string” model predicts a single ring of a protein filament in the midsection of the cell and the ingressing membrane would come to a sharp point (Figure 1.6C). In this model, it is proposed that the constriction is caused by Vps4 “pulling” on the filament by depolymerizing one side. Even if the filament could form a spiral as thick as the belt observed instead of just a ring, relying on Vps4 to pull from one side would require that the filament slide past itself throughout the entire spiral to cause the constriction, which seems unlikely. The recent “whorl” model proposes a whorl of ESCRT-III filaments would form (Figure 1.6D). A tomogram of a cell with a whorl of filaments in the division region would have revealed areas of the ingressing membrane coated with a thin filament, and other empty areas. Neither of these morphologies were observed in dividing cells.

In contrast, the “dome” model (Fabrikant et al., 2009)(Figure 1.6B) is compatible with our results if duplicated in a “two-dome” or "hourglass" model as we propose in Figure 1.6E and Movie 1.5. In the hourglass model, ESCRT proteins form two conical helices that form the belt and meet at the midplane. Because each new turn of the spiral has a smaller diameter, and the membrane attaches to the spiral via CdvA, the membrane ingresses progressively as the helices grow (Figure 1.7 and Movie 1.5). Incoming monomers join the tips of the growing helices at the center of the belt and push the existing filaments outward. As the conical helices spiral inward, the belt would grow wider as seen in the cellular tomograms. Presumably Vps4 recycles monomers

from the helices to allow further growth at the tips, accounting for the severe impact of expression of a trans-dominant allele of Vps4 on cell division (Samson et al., 2008) and our observations that while the belt width increases during constriction, the overall surface area of the belt reduces.

The *in vitro* assemblies showed that ESCRT filaments can form conical helices and bind non-specifically both laterally and radially. This strongly supports the hourglass model, since it is based on growing spirals and the shape of the belt seen in the cellular tomograms was highly variable, suggesting flexibility in filament contacts. In early dividing cells, the protein belt is flat in cross-section, which would be similar to the lateral interaction of the monomers in the cylindrical helices *in vitro*. Cells further into division exhibit a sloped belt in cross-section, similar to the cones observed *in vitro*, indicating diagonal interactions of lateral monomers in the ring during division. Stacked (nested) cones were not seen *in vivo*, however, as the thickness of the belt remained constant throughout division. The model also predicts there should be two very small "V"-shaped openings at the growing tips of the conical helices, which we did not detect, but they would have likely been too small to resolve with ECT.

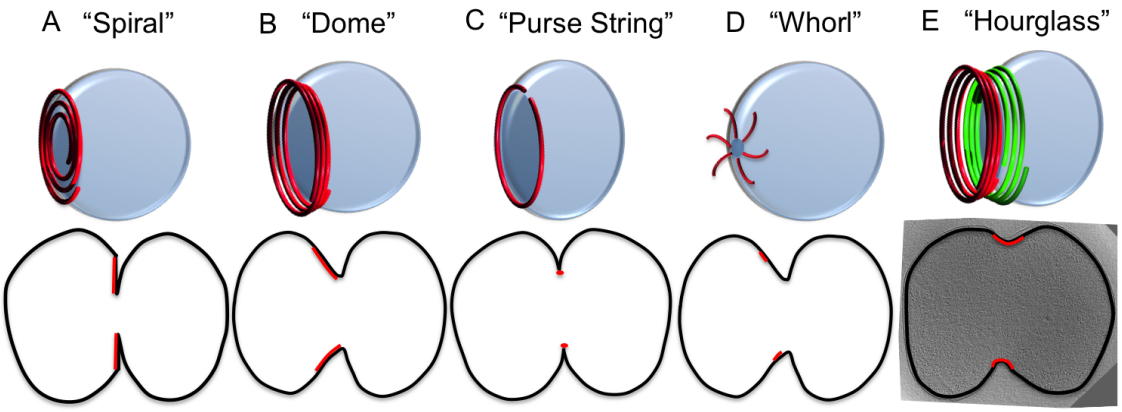

Figure 1.6. Comparison of the "hourglass" model to existing models. The top row illustrates the proposed model, and the bottom row illustrates what would have been seen in a tomographic slice of a dividing cell if the model were employed. Black lines represent membrane and red lines represent the cytokinetic belt. (A) A flat spiral decreases in diameter, creating a flat protein-coated membrane on one side. (B) A dome is formed by a spiral of decreasing diameter, coating the membrane on one side. (C) A thin, polar ESCRT filament decreases in diameter, pulling the membrane to a sharp "V"-shaped point. (D) Very recent model of whorl pattern that tightens to constrict the membrane, forming filaments that may or may not be observed in a tomographic slice. (E) Two abutted spirals with a decreasing diameter form a "U"-shaped belt in dividing cells. A slice though a tomogram of a dividing cell is shown to demonstrate the actual observations.

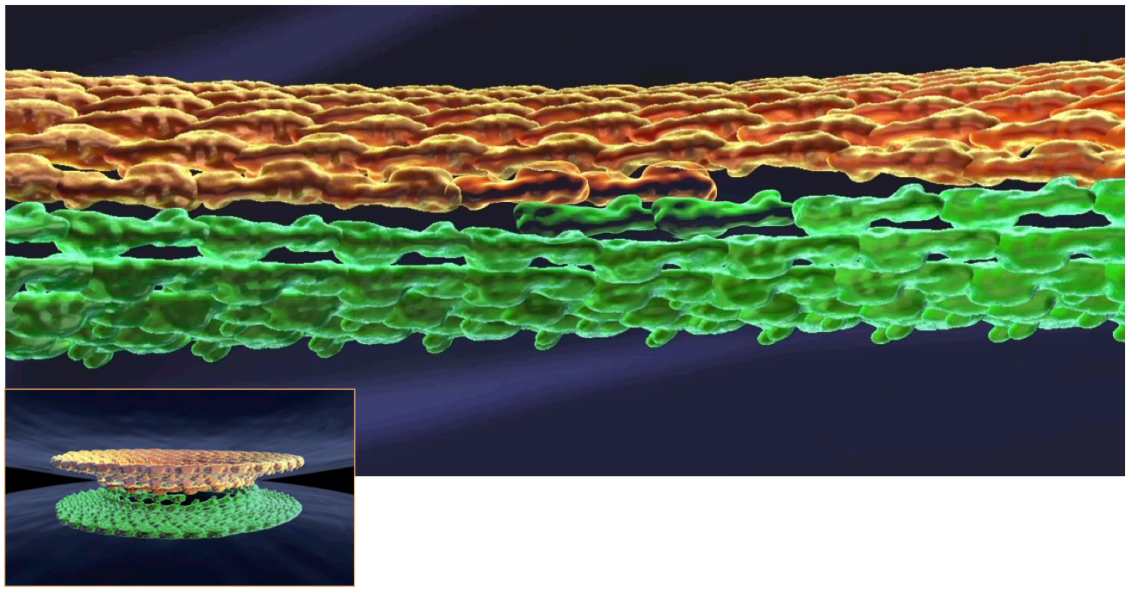

Figure 1.7. Proposed mechanism for cell division by the ESCRT system. ESCRT forms two abutted spirals decreasing in diameter in the middle, ingressing the membrane as they grow.

The hourglass model is also consistent with other observations in the literature. It was shown that ESCRT-I and –II bind to membranes first and recruit ESCRT-III, which forms filaments (Saksena et al., 2009). In the hourglass model, CdvA binds to the membrane first and recruits ESCRT-III, which forms filaments that coil. The proposed mechanism does not rely on Vps4 for constriction per se, but Vps4 is essential to recycle outer ESCRT-III monomers so they can be fed back into the growing spirals in the middle. This would explain why Vps4 mutants result in failed cell division in *S. acidocaldarius* (Samson et al., 2008) (there are likely too few monomers to complete constriction without some recycling), but small vesicles can bud into giant unilamellar vesicles without Vps4 (Wollert et al., 2009a). A limited number of buds were released into the vesicles but Vps4 was required for recycling of the ESCRT-III proteins for additional rounds of budding.

One potential problem with the model is how the activity of Vps4 is regulated so it does not unravel the helix faster from the tail than it grows at the tip. One possibility is that the filaments only become accessible to Vps4 when bound to membranes of a certain curvature. There is an inflexion point in the ingressing membrane where the curvature inverts from convex to concave, and the edge of the belt is often found at these points. Once the ESCRT-III filaments reach this point, their tails may become susceptible to disassociation by Vps4.

The hourglass model may also apply to other contexts where the ESCRT machinery acts, including, for instance, cytokinesis in eukaryotes. ESCRT proteins do not localize to the intercellular bridge in eukaryotes until the membranes are ~1 μm apart (Guizetti and Gerlich, 2012), a diameter similar to the constriction belt observed here in *S. acidocaldarius*. Thus the actin/myosin contractile ring may have evolved to constrict very large eukaryotic cells sufficiently for the ESCRT machinery to take over. It remains unclear, however, how to reconcile the hourglass model with the 17-nm putative

ESCRT filaments reported previously (Guizetti et al., 2011). The results are similar in that both models involve a helical filament of ESCRT-III that drives constriction, but 17 nm is larger than any reported ESCRT filament. The filaments were identified as ESCRT-III because CHMP2A RNAi-treated cells did not contain these filaments, but perhaps the filaments are composed of, or consist largely of, other proteins that depend on CHMP2A for assembly.

The role of the ESCRT pathway in MVB biogenesis and viral budding are also likely driven by a "dome" mechanism. While there are known differences in protein sequences between the human, yeast, and archaeal ESCRTs, the functions performed are very similar. Archaea do not have sequence homologs to ESCRT-0, -I, or –II, but CdvA performs the same function of recruiting ESCRT-III to the membrane. The fundamental difference in archaeal cell division is that one cell splits into two equally-sized cells both containing ESCRT proteins, whereas viral budding and MVB formation is one cell budding a smaller vesicle that will not contain ESCRT-III proteins (Wollert and Hurley, 2010). In viral budding and MVB formation, the membrane is also flat and ESCRT–I and –II bind first to initially deform the membrane and recruit ESCRT-III (Saksena et al., 2009). If ESCRT-III binds at a budding neck region where the membrane is already bent, then it is topologically similar to cytokinesis in eukaryotes and archaea because it encircles an opening between two compartments. There may be only a single dome rather than an hourglass, however, since the ESCRT machinery originates from one side only.

Materials and Methods

Purification, Assembly, and Imaging of *in vitro* ESCRT-III Proteins

CHMP1B, CHMP2A, CHMP3, CHMP3$^{1-150}$, and IST1N^{NTD} were purified as previously described (Bajorek et al., 2009b). CHMP2A and CHMP3 co-assemblies were formed by

concentrating both proteins to 20mg/mL (CHMP2A = 830 uM; CHMP3 = 790 uM), mixing (1:1 v/v) and incubating at room temperature for 30 mins. Monomeric $IST1_{NTD}$ was assembled by dialyzing concentrated protein (265 uM for negative stain image and 240 uM for cryo image) against 50 mM Tris pH7.0, 100 mM NaCl, 5% (v/v) glycerol, 5 mM BME for 12 hours at 4 °C. Monomeric CHMP1B was assembled by concentrating the protein to 440uM in 10 mM Tris pH 8.0, 100 mM NaCl, 5 mM BME and incubating for 24 hours at 4 °C.

CHMP1B tomograms were collected with 4–6 μm defocus, 150 $e^-/Å^2$, and pixel size of 1 nm. CHMP2A/3 tubes were negatively stained on glow discharged carbon/formvar grids with 2% uranyl acetate and imaged at 52,000 × magnification. IST1N tubes were similarly stained and imaged, as well as plunge frozen and imaged using electron cryotomography. The parameters of tomographic data collection were 41,000 × magnification, -3.5 μm defocus, tilt ± 60°, 2° tilt increments, a dose ranging between 120–240 $e^-/Å^2$, and pixel size of 0.5 nm. Tomograms were reconstructed using etomo or Raptor and were binned by two. Software packages Amira and IMOD were used for making supplemental movies.

Growth Conditions and Synchronization of *S. acidocaldarius*

S. acidocaldarius DSM639 was grown in Brock's medium, pH 3.2 at 78 °C and synchronized as described in (Duggin et al., 2008). Specifically, 75 mL of culture at approximately OD_{600} = 0.1 were applied to a poly-D-lysine-coated membrane within the baby machine apparatus. After pumping Brock's medium through the apparatus for 3.5 hours at approximately 0.8 mL/min, newly divided cells were collected on ice over a period of 30 minutes. Synchronized grow-out was initiated by transferring the vessel containing the cells from ice to a water bath heated to 78 °C.

Protein Purification

S. acidocaldarius CdvA (residues 69–238) was purified as described in (Samson et al., 2011).

Preparation of *S. acidocaldarius* Liposomes

Polar lipid fraction E (PLFE) tetraether lipids were isolated from *S. acidocaldarius* cells and PLFE liposomes were prepared as previously described (Samson et al., 2011).

Affinity Purification of Antibodies

Affinity columns were prepared and antisera were purified as described in (Samson et al., 2008).

EM Sample Preparation, Data Collection, and Tomographic Reconstruction

EM R2/2 copper Quantifoil grids were made hydrophilic by using a Harrick plasma cleaner for 30 seconds. The synchronized cells were mixed 3:1 with 10μm colloidal gold particles and 5% BSA. A 3 μL droplet of the cell mixture was applied to each grid, then

blotted and plunge frozen into liquid ethane using a Gatan Cryoplunge 3. The grids were stored in a liquid nitrogen-cooled dry shipper and shipped to Caltech for imaging.

EM images were collected using a Polara 300kV FEG transmission electron miroscope (FEI Company) equipped with an energy filter and a lens-coupled 4k × 4k Ultracam (Gatan). Tilt series were recorded from −65° to +65° with an increment of 1° at −15 μm under focus using the Leginon software package (Suloway et al., 2005). Cumulative doses of up to 200 $e^-/Å^2$ were used.

The tilt series were binned by two and 3D tomograms were calculated using the IMOD software package (Kremer et al., 1996). Dividing cells were 3D rendered using Amira (Visage Imaging, Inc., San Diego, CA)

Acknowledgements

This work was supported in part by NIH Grant P50 GM082545 to GJJ, NSF grant DMR1105277 to PLC and a gift to Caltech from the Gordon and Betty Moore Foundation. We thank Wesley I. Sundquist for advice and critical reading of the manuscript, Kay Grunewald for use of laboratory equipment and Morgan Beeby, Jason Porath, and Jean Choi for their help with illustrations.

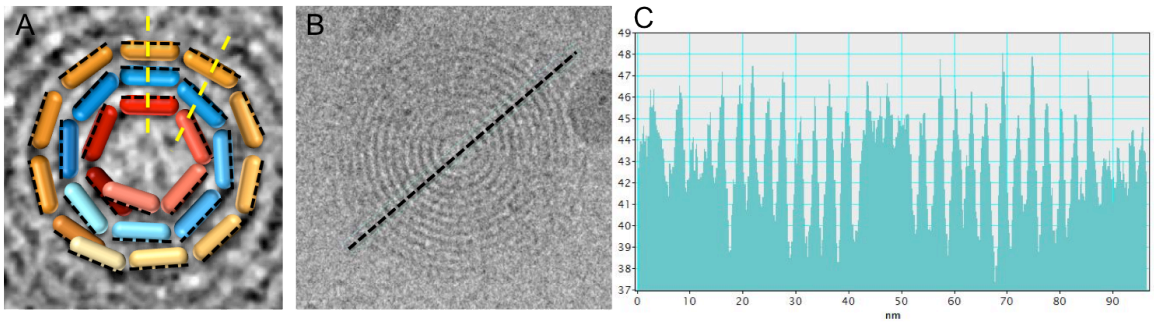

Figure S1. Related to Figure 1.1C. (A) The bull's-eye pattern that results when viewing a CHMP1B tube from the top view indicates concentric helices. The first three layers were expanded to demonstrate possible monomer interactions. Because each layer is larger than the previous, monomers in radial filaments cannot be in a single register. The vertical, yellow dotted line shows the monomers could start in register, but by the next monomer (diagonal dotted line), they are already out of register, demonstrating a non-specific radial interaction. (B) The smallest-diameter CHMP1B helix has a circumference of 38 nm, and interestingly, the subsequent rings increase in circumference by 19 nm, half the circumference of the smallest ring. A line scan intensity profile measures the intensity of the signal across the dotted line, which is plotted in the graph (C), showing a regular spacing of filaments 3 nm apart.

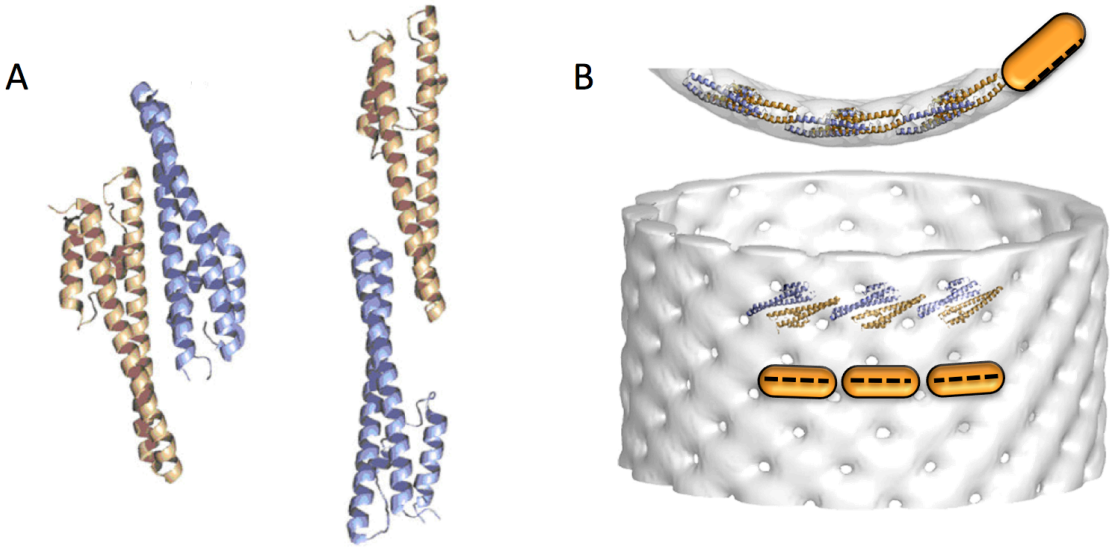

Fig S2. Related to Figure 1.1C. (A) The X-ray crystal structure of CHMP3 contained two dimer interactions, supporting the ability of the protein to bind itself in many ways (Muziol et al., 2006). (B) The crystal structure was fit into the EM reconstruction model of CHMP2AΔC/3ΔC tubes to show roughly lengthwise binding to form the filament (Lata et al., 2008b). The membrane binding domains are facing outward, as indicated by the dotted black line.

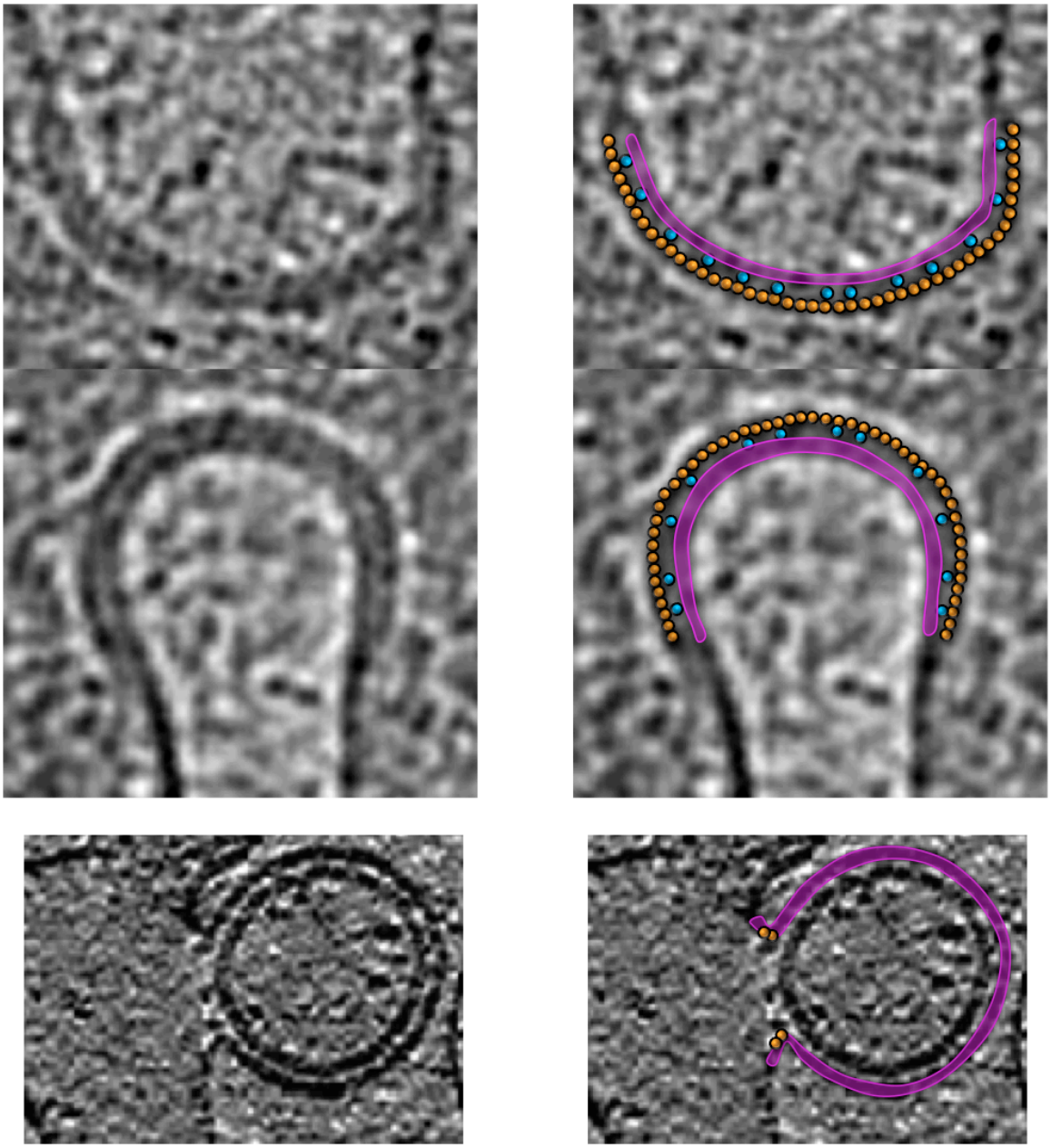

Figure S3. Related to Figure 1.5. The left panel shows slices through a tomogram of "neck" regions where ESCRT is driving membrane constriction. In archaea, ESCRT-III (orange) cannot bind directly to the membrane (purple), so CdvA (blue) is necessary for recruitment. In humans, ESCRT-III can bind directly to the membrane, and probably embeds halfway into the membrane, leaving less than 2 nm jutting out from the membrane. The image shown is gag budding from wildtype cells, from (Carlson et al., 2010). Since the density would be right up against the membrane, and is so small, it is not likely to be detected by ECT. There are also fewer filaments required to bud the relatively small HIV particle. Therefore, archaea seem to be an advantageous system for imaging ESCRT since there is a spacer protein, making ESCRT-III more visible, and the cells are large so there is more material needed for constriction.

1.3

ADDITIONAL INFORMATION NOT SUBMITTED FOR PUBLICATION

In order to provide more information about the experiments and results, additional figures are included here that were not included in the submission for publication.

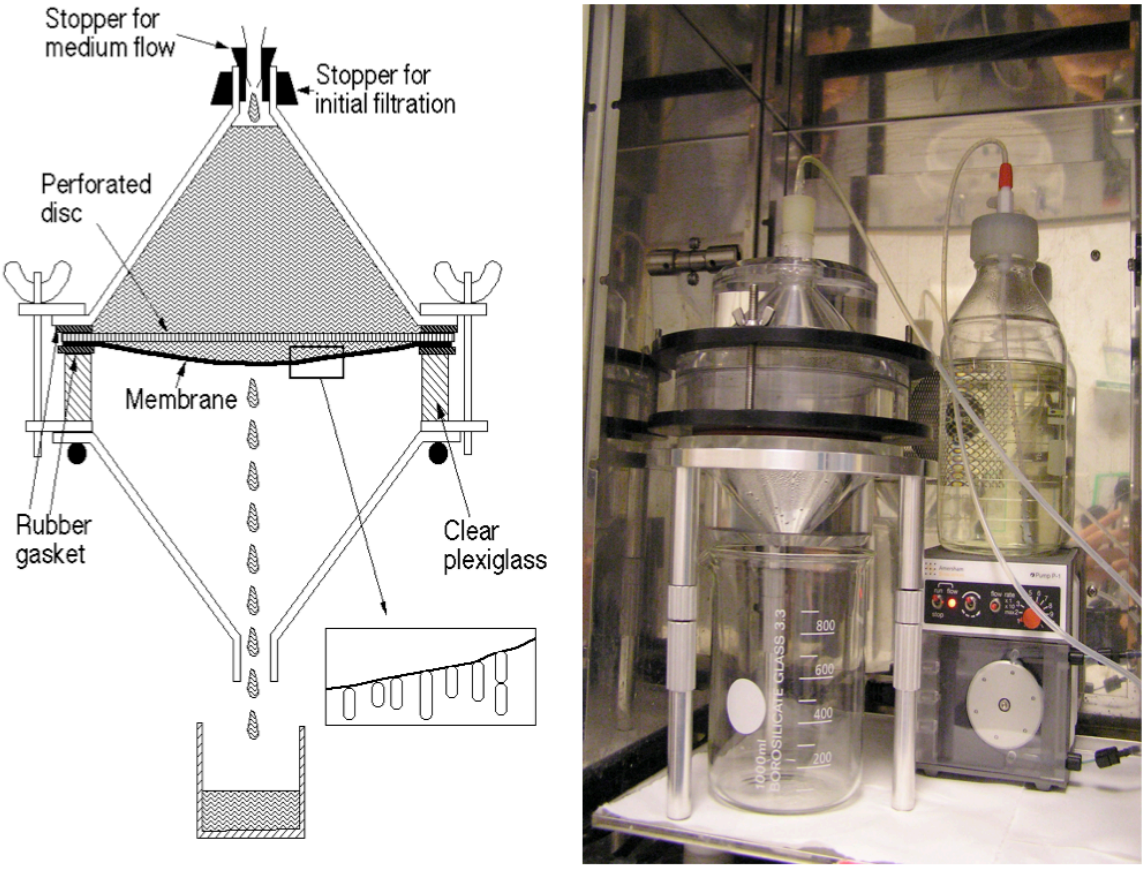

Figure 1.8. Baby machine set up. Cells are adhered to a nitrocellulose membrane using poly-L-lysine. The membrane is flipped upside down and placed between the wide ends of two funnels. Warm medium is dripped over the membrane, and as new cells are born, they detach and fall into a collection cup on ice. Details for setup were previously described (Duggin et al., 2008).

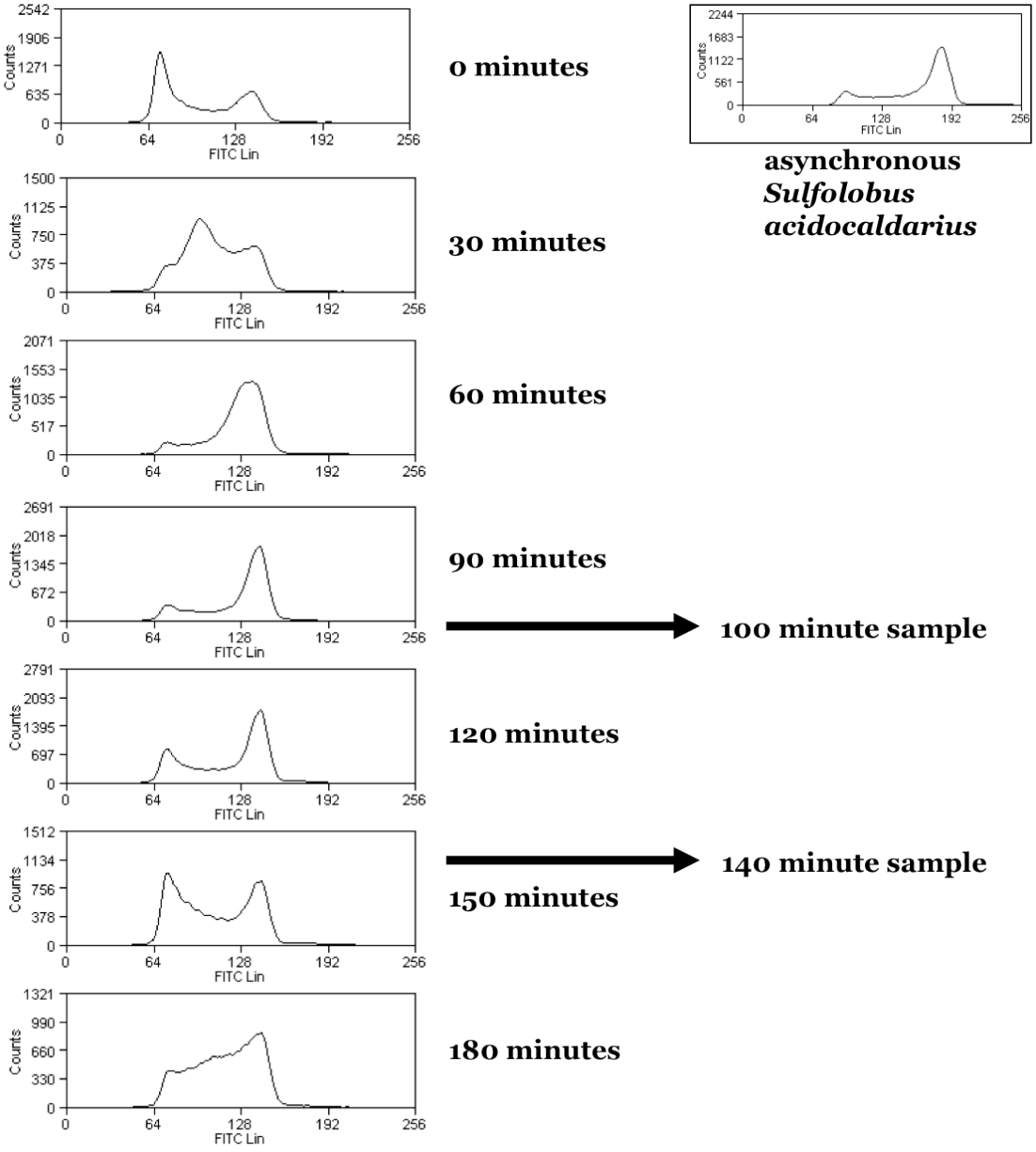

Figure 1.9. Flow cytometry of synchronized cells. An aliquot from each collection of cells was fixed in ethanol and saved for flow cytometry. Additional aliquots were plunge frozen for electron cryotomography at 100 mins and 140 mins. The sample collected at 140 mins was the most enriched for dividing cells, so that sample was the focus of tomography.

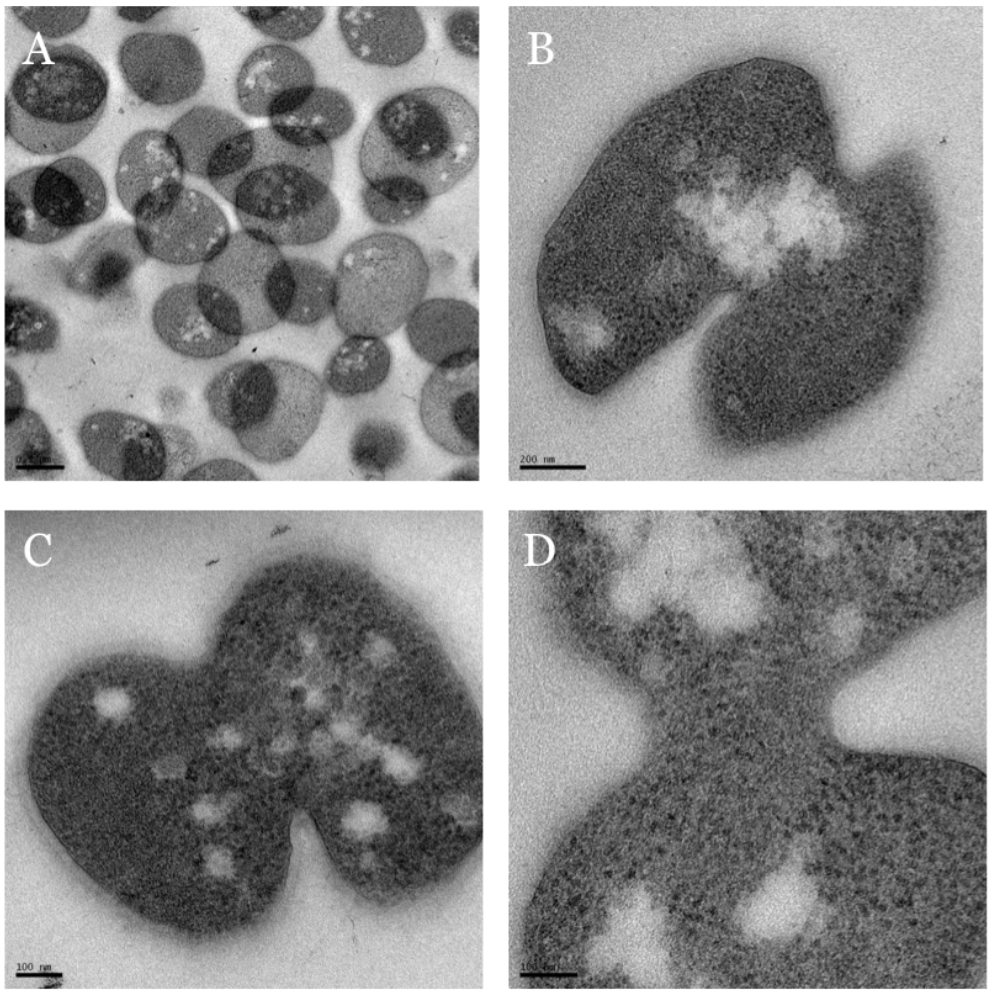

Figure 1.10. Thin sections of fixed, stained, and embedded cells. (A) Asynchronized *S. acidocaldarius* cells provide large numbers for imaging, but rarely dividing cells. (B)-(C) Examples of the few dividing cells observed. Asymmetric division morphology is preserved, but structural detail of the division belt is lost (D).

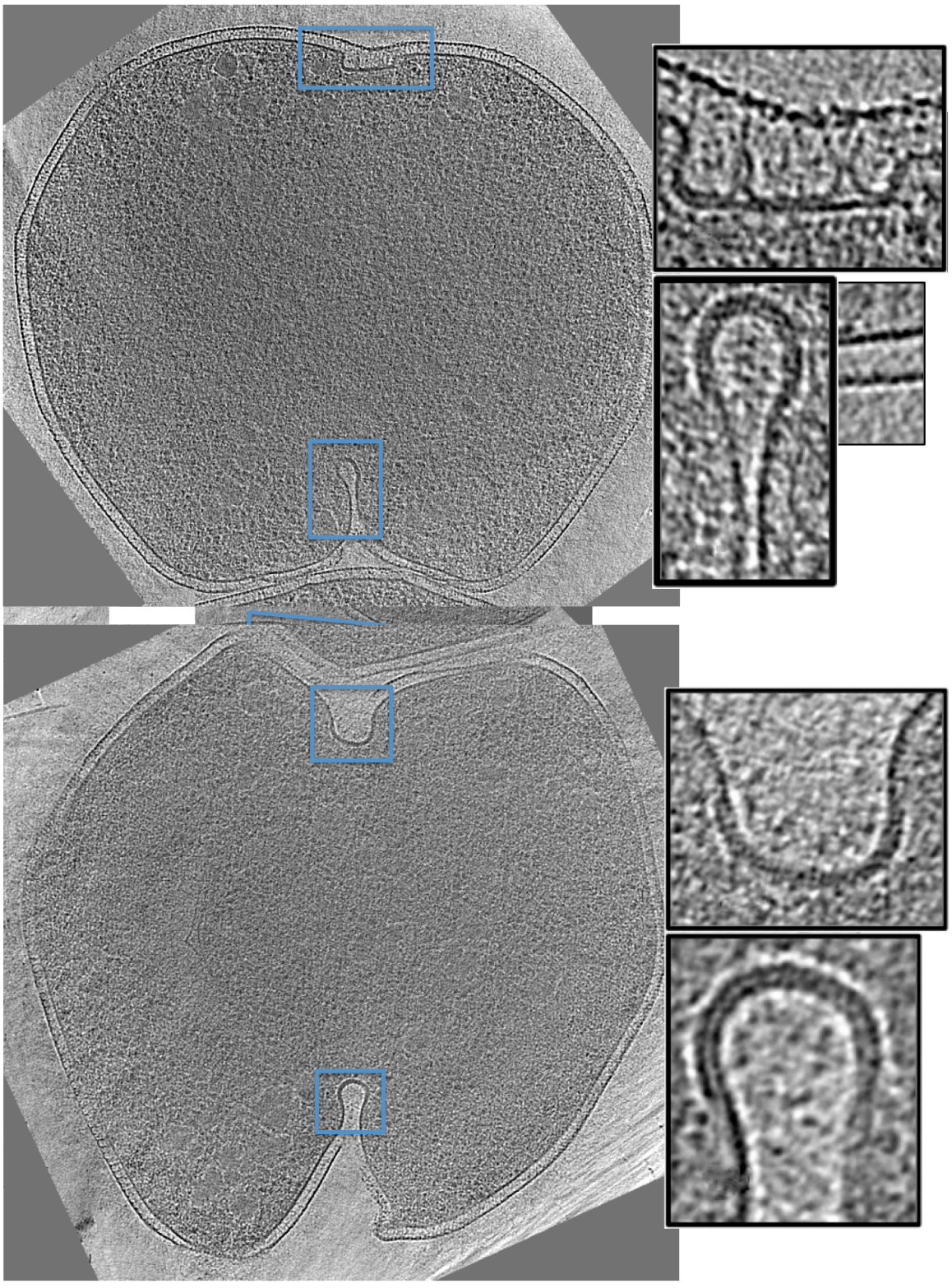

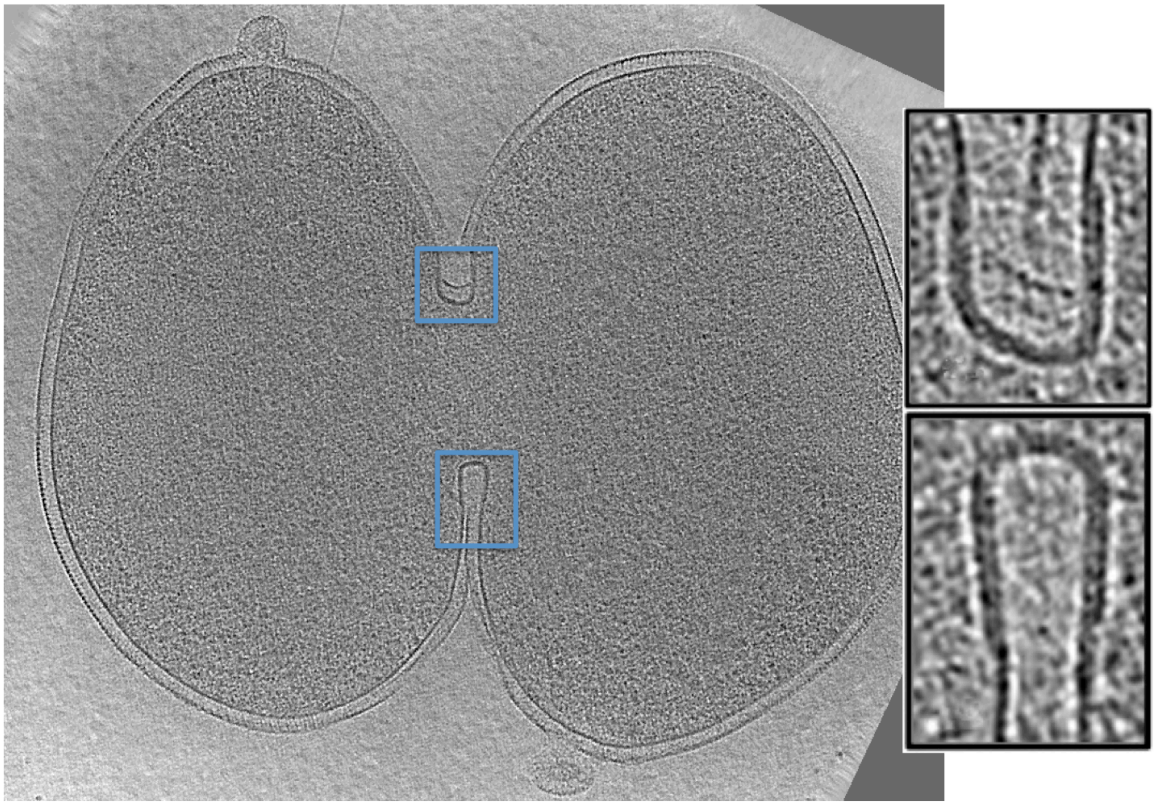

Figure 1.11. Expanded views of dividing cells. Several examples of dividing cells are shown as enlarged versions. The insets show a cross-section of the division belt, with the location indicated by blue rectangles.

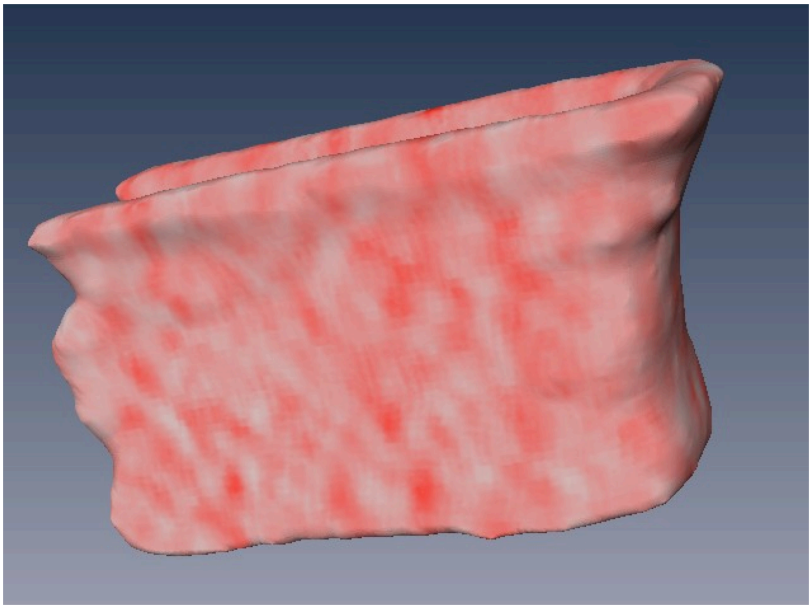

Figure 1.12. Projection of density reveals no pattern. One division furrow was segmented by hand using Amira. The surrounding few pixels were projected onto the segmentation to try and reveal a lattice pattern from the protein. No pattern was observed.

1.4

NEXT STEPS

Further Electron Cryotomography Studies to Identify the Cytokinetic Belt

We were able to characterize the morphology of the cytokinetic ring, but it has not been conclusively shown that the belt observed contains ESCRT. The following experiments are proposed for future steps in order to more confidently identify the belt.

ESCRT was observed in a dynamic system using dividing *Sulfolobus acidocaldarius* cells, but ESCRT has not been seen in any other dividing archaea cells. The Crenarchaea are known to have genes for ESCRT. Some lack genes for other division machinery like FtsZ, while others contain those genes but have been shown to favor ESCRT for division (Pelve et al., 2011). In order to compare the morphology of the cytokinetic ring in archaea, electron cryotomography (ECT) could be used to collect tomograms of other species as they are dividing. Images of other dividing Crenarchaea will teach us if the belt we observed is specific to *S. acidocaldarius* or conserved across species.

Nitrosopumilus maritimus is known to use ESCRT for division even though it contains FtsZ. Cells are very small and therefore a good candidate for ECT. I received cells from David Stahl's lab and collected two-dimensional projection images. I found that none of the cells were dividing and many were lysed, probably from osmotic shock or mechanical pressure during blotting (Figure 1.12). The Stahl Lab is trying to create a protocol for harvesting cells that will enrich for intact, dividing cells. I also imaged a newly discovered species of Crenarchaea, *Thermogladius shockii*, which is also sufficiently small for ECT. It is unknown if *T. shockii* divides using ESCRT because it has never been sequenced, but according to its phylogeny, it is very likely. Unfortunately,

there were contamination problems and I rarely captured cells on EM grids. There are many other species that are candidates for ECT due to their size and use of ESCRT for division. If the cytokinetic belt observed in *S. acidocaldarius* is present in other species that use ESCRT for division, but not in species that use other systems instead, this would be further evidence for the identification of the belt as ESCRT.

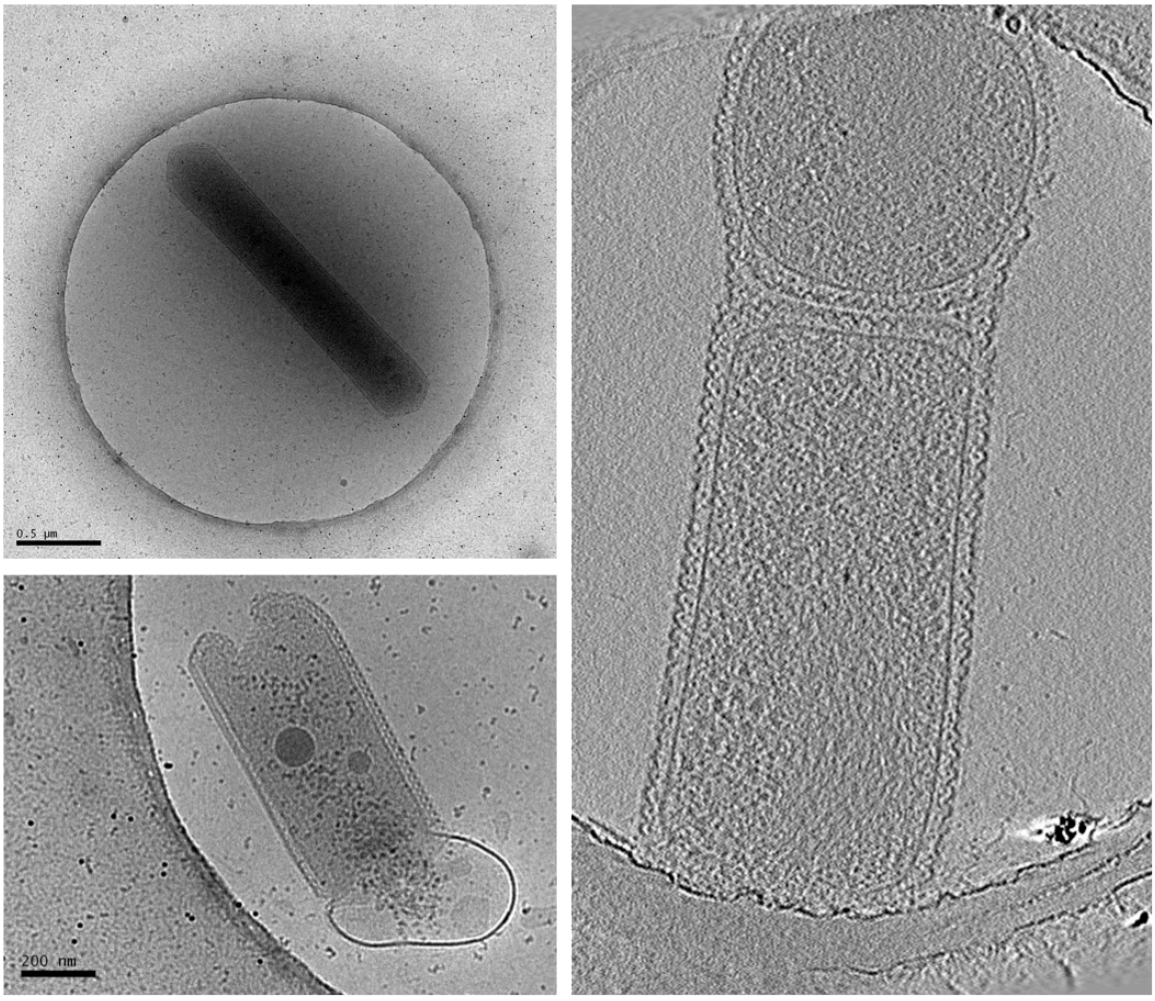

Figure 1.12. *Nitrosopumilus maritimus*. Left two panels are projection images of *N. maritimus* showing how long many grow when they are about to divide (top) and the common morphology observed in lysed cells (bottom). The right panel is a tomographic slice of a budding cell, indicating unfavorable conditions (courtesy of Zhiheng Yu). Healthy division was never observed among *N. maritimus*.

The belt observed in *S. acidocaldarius* could also be identified by immunolabeling. An antibody is attached to a protein of interest, and a secondary antibody carries a fluorescent tag or an electron-dense gold bead to the site for imaging. Immunofluorescence labeling of CdvA, ESCRT-III, and Vps4 revealed that all three form a ring at the midbody in dividing cells (Samson et al., 2011). I successfully repeated the immunofluorescence of CdvA to test the integrity of the ring and robustness of the protocol (Figure 1.13).

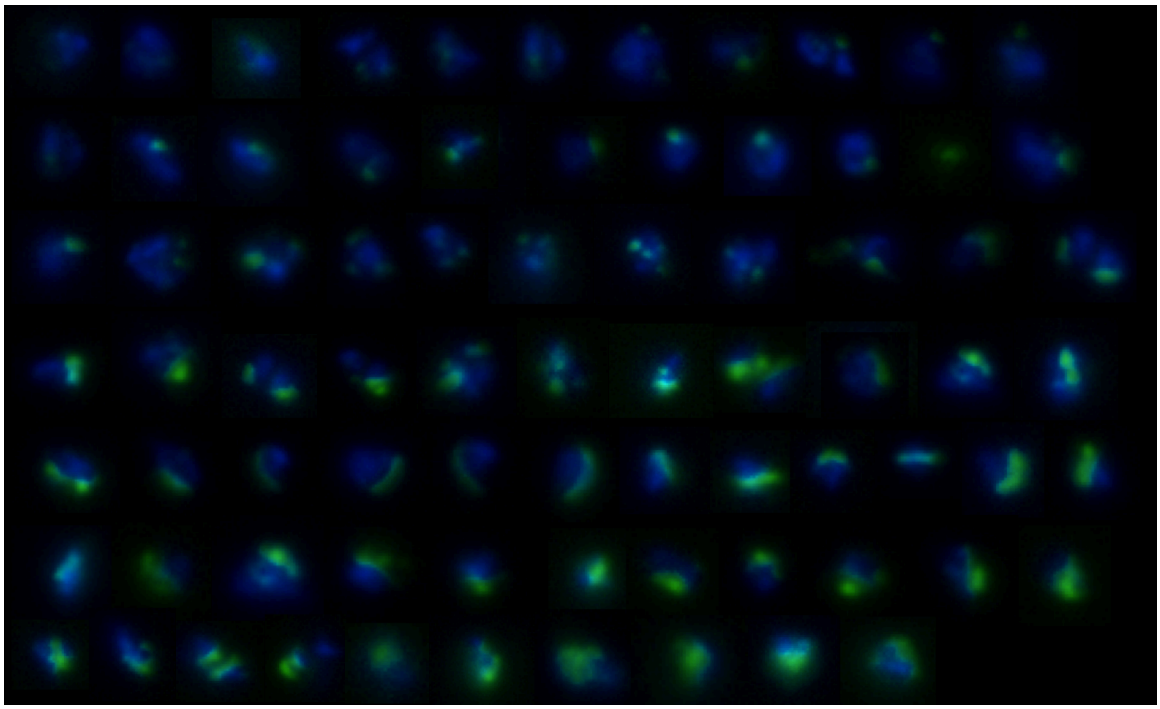

Figure 1.13. Immunofluorescence of CdvA in *S. acidocaldarius*. Panel of immunofluorescently-labeled CdvA ranging from spots to belts.

Since the immunofluorescence was successful, I next tried to immunogold label CdvA for imaging with ECT. Unfortunately, the cells did not permeabilize enough for the gold beads to flow into the cell and bind to CdvA (Figure 1.14). The protocol was repeated several times with more vigorous permeabilization, but the cells were either completely intact or completely lysed. Further optimization would be needed to permeabilize the

cells in order for gold beads to flow inside but maintain the structure of the division belt. I also tried cryosectioning the cells with the help of Mark Ladinsky. We high-pressure froze pellets of cells, thin-sectioned them, and added antibodies on top of the sections. However, the cells did not maintain their shape during preparation and we were unable to conclude whether the gold beads successfully bound to CdvA. A different preparation may successfully label the belt for further identification. However, it is known from immunofluorescence that each ESCRT component localizes to a ring at the division site. Since the antibodies used for immunolabeling are relatively long and flexible, this approach may not discern each of the components.

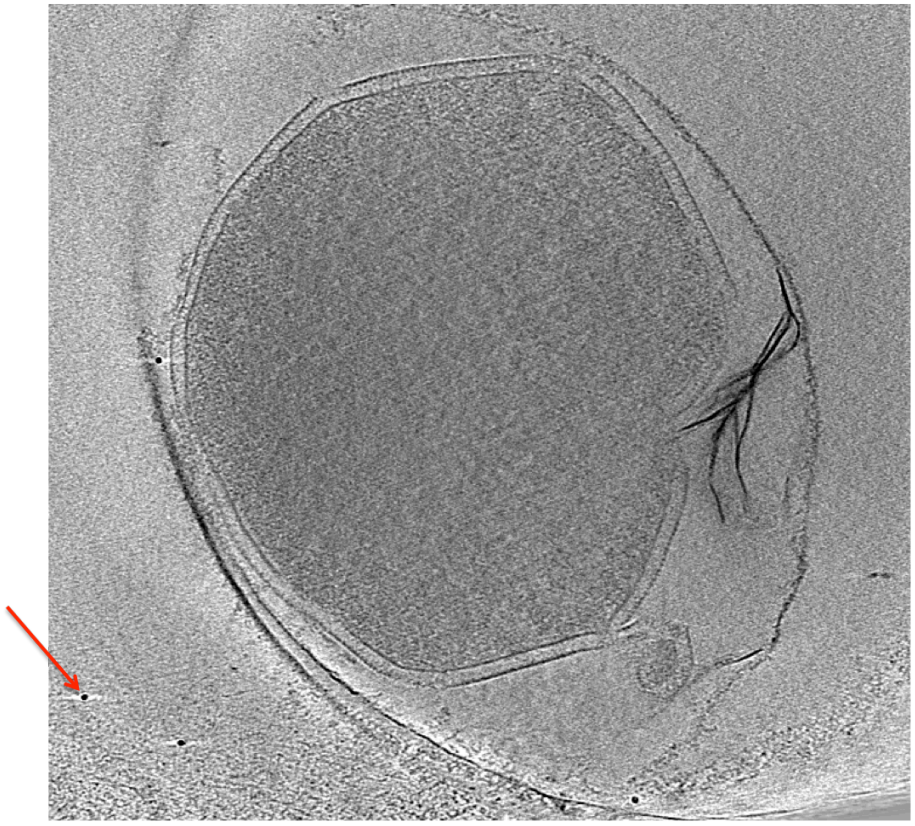

Figure 1.14. Immunogold labeling of CdvA in *S. acidocaldarius*. A permeabilized cell was still too intact for gold beads to flow inside to bind to CdvA. Red arrow points to an example of a secondary antibody carrying a gold bead.

Another approach to identifying the belt in *S. acidocaldarius* would be to study the vesicles secreted by these cells. In 2009, Ellen et al. analyzed vesicles secreted by several Sulfolobus species using mass spectrometry (Ellen et al., 2009). It was found that the vesicles contained ESCRT-III proteins and Vps4, but not CdvA. Therefore, budding vesicles could be analyzed using ECT to compare any density observed to the division belt. If a similar belt is found, then CdvA must not be a main structural component of the division belt since it is not involved in vesicle budding. If no belt is found, or it is less significant, CdvA must be the main component of the division belt or be responsible for recruiting larger amounts of ESCRT-III than is used for vesicle secretion. Another possibility is that vesicles employ a different mechanism for budding than cells do for division, and the proteins may arrange in a different morphology altogether. I have analyzed budding vesicles in *S. acidocaldarius* and found filaments through the middle of the neck and sometimes through the membrane attaching to the S-layer (Figure 1.15A). The vesicles that have completed budding have varied in morphology, some containing S-layer. Some vesicles without S-layer appeared to have a layer in addition to the membrane that is very similar to the division belt (Figure 1.15B). The density and dimensions are the same as the layer observed on ingressing membranes. Because of the variation of vesicles observed, it is not possible to make conclusions about ESCRT's involvement or analyze the composition of the division belt. For future steps, vesicles that have been harvested, purified, and analyzed with mass spectroscopy would be better candidates for ECT. Knowing which ESCRT components were present, we could analyze the membrane to compare with the division belt.

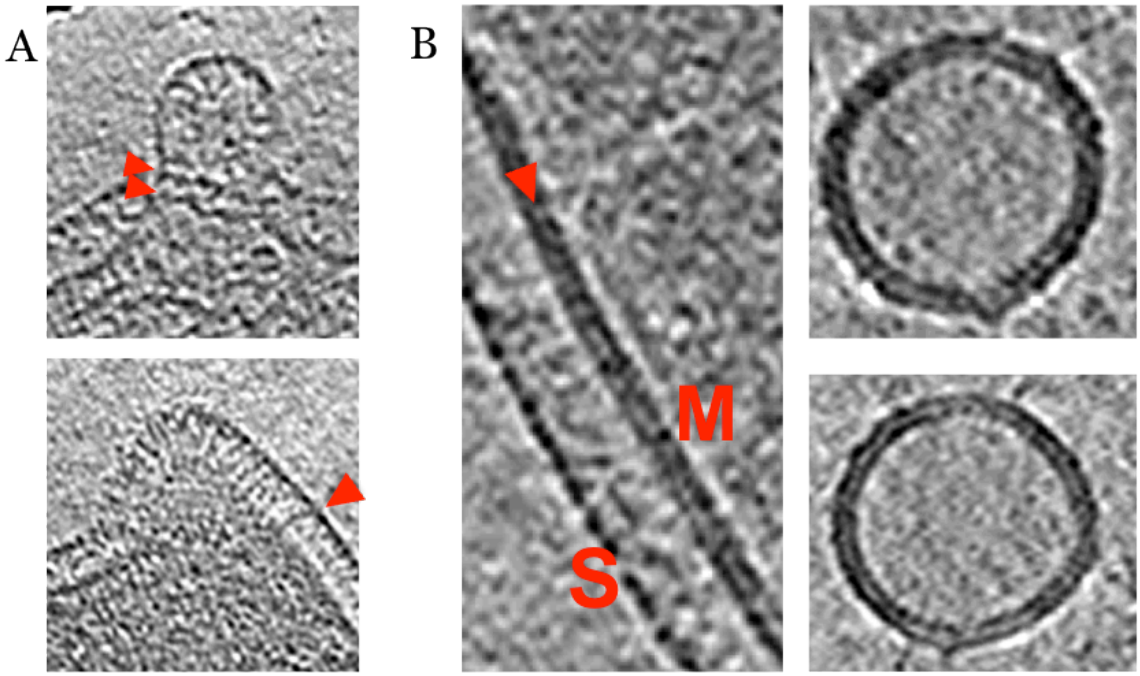

Figure 1.15. Tomographic slices through vesicles from *S. acidocaldarius*. (A) Budding vesicles have filaments through the middle of the neck (arrowheads), but no belt similar to that seen in dividing cells. The top panel is budding without S-layer. The bottom panel is maintaining its S-layer and the filament shown runs through the S-layer. (B) Released vesicles sometimes have a layer very similar to the belt in dividing cells. The left panel is the belt seen in dividing cells, indicated by the arrowhead. The S-layer and membrane are labeled. The right two panels are examples of vesicles with a similar density on the membrane.

In 2011, Samson et al. performed liposome-binding assays with CdvA and ESCRT-III on tetraether lipids from *S. acidocaldarius*. CdvA bound to liposomes, ESCRT-III had no effect, and the two added together resulted in extensive deformation of the liposomes. I repeated the experiment of adding CdvA to liposomes in order to compare the density formed with that observed in cells. Unfortunately, the protein did not bind well to liposomes, and the protocol should be repeated with new protein. CdvA assembled into filaments but were rarely found on liposomes (Figure 1.16). Using antibodies, I labeled the CdvA with gold beads and found that the gold beads clustered in the aggregates of filaments but did not bind to the liposomes, confirming that the CdvA

was not binding to liposomes (Figure 1.16C). In one tomogram, liposomes were wrapped by bundles of CdvA, which gave insight to the dimensions of the density CdvA would form on membranes by itself (Figure 1.16D). Future experiments with new protein (that had been confirmed to bind to liposomes with binding assays) would support the observations from the one tomogram of CdvA-coated liposomes. Additionally, once CdvA is consistently binding liposomes, we could add ESCRT-III and rapidly plunge freeze to observe the two together and compare with the belt in dividing cells. This may also capture the process of membrane deformation, which would provide an *in vitro* system for comparing to cells.

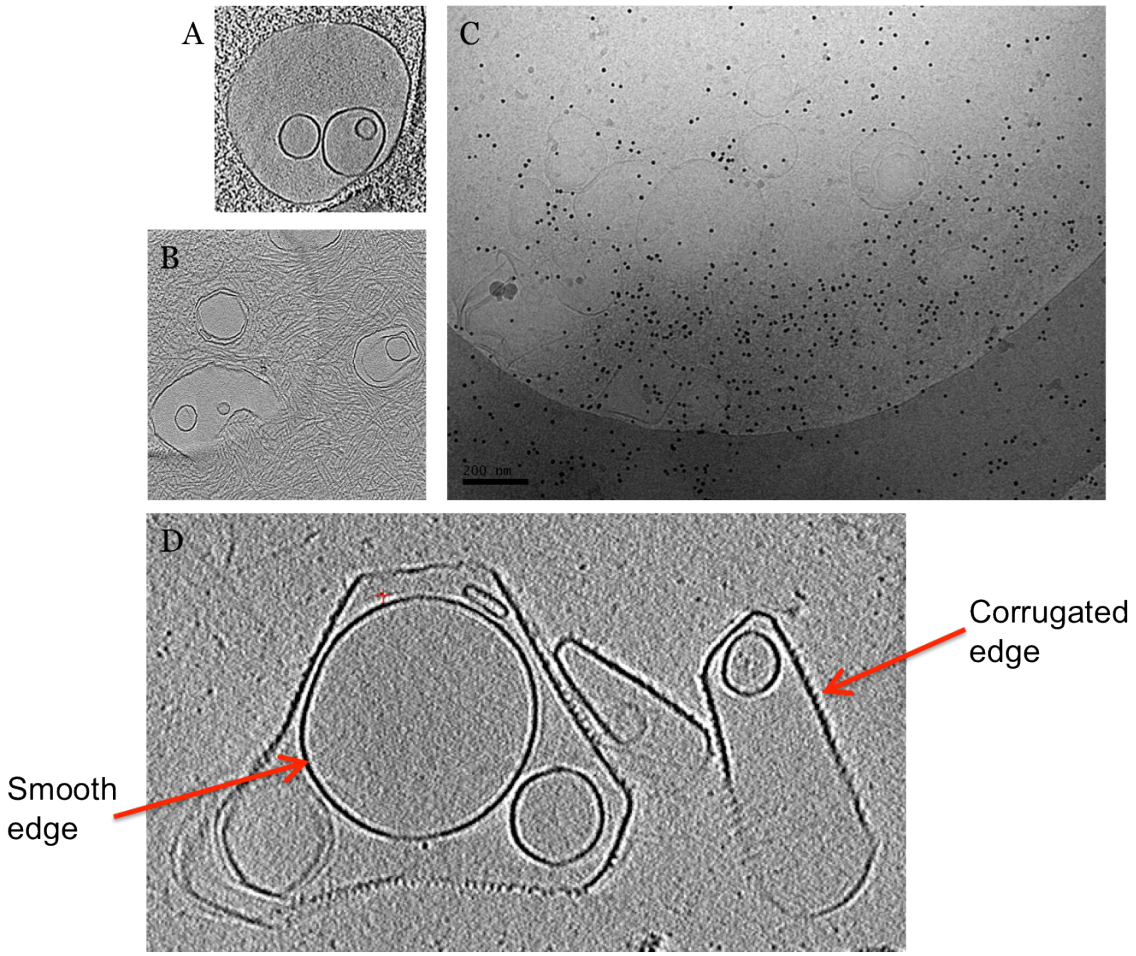

Figure 1.16. CdvA bound to tetraether liposomes. (A) Slice through a tomogram of plain liposomes without CdvA added. (B) Slice through a tomogram of liposomes with CdvA added. CdvA assembled into filaments around the liposomes. (C) Projection image through liposomes with immunogold-labeled CdvA. The 10-nm-gold beads are concentrated in the CdvA aggregates but not bound to the liposomes. Therefore, the CdvA is not binding to the liposomes. Scale bar is 200 nm. (D) Slice of a tomogram through liposomes coated in filaments that wrap around the liposomes in bundles with an 8-nm-spacing. The outer liposomes appear to have a corrugated edge while the inner liposomes unexposed to the filaments are smooth. The filaments are likely CdvA since there are no filaments around the liposomes without CdvA added.

Other Approaches to Characterize the Cell Division Machinery

The Crenarchaeal phylum is one of the most abundant forms of life on earth and yet we know very little about how these cells divide. Many of these organisms lack typical genes for cell division, so the machinery used was unknown until recent publications revealed the presence of ESCRT genes (Samson et al., 2008; Lindas et al., 2008). Biochemical assays have since shown ESCRT plays an essential role in cell division in *Sulfolobus acidocaldarius*. In future projects, I plan to use a variety of techniques to explore the role of ESCRT in other species.

A survey of species could involve immunofluorescence to determine the localization of ESCRT and FtsZ throughout the cell cycle. ESCRT and FtsZ antibodies recognize antigens across a variety of species and therefore could determine the cell division machinery in species not yet sequenced. Using confocal microscopy, proteins may reveal a transient distribution, a solid ring at the division site, a punctate pattern, or other localization pattern. Based on the observations of each protein complex throughout the cell cycle, we could provide evidence for which system is being used and how it might function. In species that encode for FtsZ but rely on ESCRT for division, such as *N. maritimus*, examining fluorescence throughout the cell cycle may reveal a localization pattern and potential novel role for FtsZ. Mapping these species with phylogenetic trees will determine the evolutionary relationship between division systems.

There are many available assays to further investigate the cell division process. The known sequences of archaea could be analyzed to search for cell division genes. Species able to be synchronized may be used for Western blots to determine which proteins are up regulated and therefore likely active throughout the cell cycle. Further analysis of a species could also involve growth curves and flow cytometry to determine length of time spent in each phase. Overexpression or mutant vectors for ESCRT have

been created for Crenarchaea by collaborators and could be transformed to observe morphology changes in cells.

It is intriguing that ESCRT is involved in so many biological processes and is conserved across archaea and eukaryotes. An interesting study would be to compare the gene sequences and physical structure of ESCRT in both domains to answer the question: How is ESCRT conserved across domains? To compare the structure of the division machineries, tissue culture techniques could be used to grow eukaryotic cells expressing fluorescently tagged ESCRT. Fluorescence imaging of dividing cells may reveal the length of time and abundance of ESCRT proteins at the site of cytokinesis. The localization pattern could be compared with that seen in archaeal species to determine structural conservation throughout evolution. Bioinformatics and computational approaches could be used. Genome sequence analysis and phylogenetic trees will provide an evolutionary approach.

REFERENCES

Bajorek, M., Morita, E., Skalicky, J. J., Morham, S. G., Babst, M., and Sundquist, W. I. (2009a). Biochemical analyses of human IST1 and its function in cytokinesis. *Mol Biol Cell 20*, 1360–1373.

Bajorek, M., Schubert, H. L., McCullough, J., Langelier, C., Eckert, D. M., Stubblefield, W. M., Uter, N. T., Myszka, D. G., Hill, C. P., and Sundquist, W. I. (2009b). Structural basis for ESCRT-III protein autoinhibition. *Nat Struct Mol Biol 16*, 754–762.

Bodon, G., Chassefeyre, R., Pernet-Gallay, K., Martinelli, N., Effantin, G., Hulsik, D. L., Belly, A., Goldberg, Y., Chatellard-Causse, C., Blot, B., *et al.* (2011). Charged multivesicular body protein 2B (CHMP2B) of the endosomal sorting complex required for transport-III (ESCRT-III) polymerizes into helical structures deforming the plasma membrane. *J Biol Chem 286*, 40276–40286.

Boura, E., Rozycki, B., Chung, H. S., Herrick, D. Z., Canagarajah, B., Cafiso, D. S., Eaton, W. A., Hummer, G., Hurley, J. H. (2012) Solution structure of the ESCRT-I and –II supercomplex: Implications for membrane budding and scission. *Structure 20*, 874–886.

Carlson, L.-A., De Marco, A., Oberwinkler, H., Habermann, A., Briggs, J. A. G., Kräusslich, H.-G., and Grünewald, K. (2010). Cryo electron tomography of native HIV-1 budding sites. *PLoS Pathog 6*, 1–11.

Dimaano, C., Jones, C. B., Hanono, A., Curtiss, M., and Babst, M. (2008). Ist1 regulates Vps4 localization and assembly. *Mol Biol Cell 19*, 465–474.

Duggin, I. G., McCallum, S. A., and Bell, S. D. (2008). Chromosome replication dynamics in the archaeon *Sulfolobus acidocaldarius*. *Proc Natl Acad Sci* USA *105*, 16737–16742.

Ellen, A. F., Albers, S.-V., Huibers, W., Pitcher, A., Hobel, C. F. V., Schwarz, H., Folea, M., Schouten, S., Boekema, E. J., Poolman, B., *et al.* (2009). Proteomic analysis of secreted membrane vesicles of archaeal Sulfolobus species reveals the presence of endosome sorting complex components. *Extremophiles 13*, 67–79.

Engelhardt, H., Schuster, S.C., Baeuerlein, E. (1993). An Archimedian spiral: the basal disk of the Wolinella flagellar motor. *Science 262*, 1046–1048.

Fabrikant, G., Lata, S., Riches, J. D., Briggs, J. A. G., Weissenhorn, W., Kozlov, M. K. (2009) Computational model of membrane fission catalyzed by ESCRT-III. *PLoS Comp Biol* 5, 1–11.

Gan, L., and Jensen, G. (2012). Electron tomography of cells. *Q Rev Biophys 45*, 27–56.

Gelderblom, H. R., Ozel, M., C., Pauli, G., (1989). Morphogenesis and morphology of HIV. Structure-function relations. *Arch Virol 106*, 1–13

Guizetti, J., and Gerlich, D. W. (2012). ESCRT-III polymers in membrane neck constriction. *Trends Cell Biol 22*, 133–140.

Guizetti, J., Schermelleh, L., Mäntler, J., Maar, S., Poser, I., Leonhardt, H., Müller-Reichert, T., and Gerlich, D. W. (2011). Cortical constriction during abscission involves helices of ESCRT-III-dependent filaments. *Science 331*, 1616–1620.

Hanson, P. I., Roth, R., Lin, Y., and Heuser, J. E. (2008). Plasma membrane deformation by circular arrays of ESCRT-III protein filaments. *J Cell Biol 180*, 389–402.

Hurley, J. (2010). The ESCRT complexes. *Crit Rev Biochem Mol Biol 45*, 463–487.

Kremer, J. R., Matronarde, D. N., McIntosh, J. R. (1996). Computer visualization of three-dimensional image data using IMOD. *J Struct Biol* 116, 71–76.

Lata, S., Roessle, M., Solomons, J., Jamin, M., Gottlinger, H. G., Svergun, D. I., and Weissenhorn, W. (2008a). Structural basis for autoinhibition of ESCRT-III CHMP3. *J Mol Biol 378*, 818–827.

Lata, S., Schoehn, G., Jain, A., Pires, R., Piehler, J., Gottlinger, H., and Weissenhorn, W. (2008b). Helical structures of ESCRT-III are disassembled by VPS4. *Science 321*, 1354–1357.

Lata, S., Schoehn, G., Solomons, J., Pires, R., Göttlinger, H. G., and Weissenhorn, W. (2009). Structure and function of ESCRT-III. *Biochem Soc Trans 37*, 156–160.

Li, Z., Trimble, M. J., Brun, Y. V., and Jensen, G. (2007). The structure of FtsZ filaments in vivo suggests a force-generating role in cell division. *EMBO* J *26*, 4694–4708.

Lindås, A.-C., Karlsson, E. A., Lindgren, M. T., Ettema, T. J. G., and Bernander, R. (2008). A unique cell division machinery in the Archaea. *Proc Natl Acad Sci* USA *105*, 18942–18946.

Makarova, K. S., Yutin, N., Bell, S. D., and Koonin, E. V. (2010). Evolution of diverse cell division and vesicle formation systems in Archaea. *Nat Rev Micro 8*, 731–741.

Morita, E., Sandrin, V., McCullough, J., Katsuyama, A., Baci Hamilton, I., and Sundquist, W. I. (2011). ESCRT-III protein requirements for HIV-1 budding. *Cell Host Microbe 9*, 235–242.

Morita, E., and Sundquist, W. (2004). Retrovirus Budding. *Annu Rev Cell Dev Biol 20*, 395–425.

Muziol, T., Pineda-Molina, E., Ravelli, R. B., Zamborlini, A., Usami, Y., Gottlinger, H., Weissenhorn, W. (2006). Structural basis for budding by the ESCRT-III Factor CHMP3. *Dev Cell* 10, 821–830.

Pelve, E. A., Lindas, A-C., Martens-Habbena, W., de la Torre, J. R., Stahl, D. A., Bernander, R. (2011) *Mol Micro* **82** (3) 555–566.

Pilhofer, M., Ladinsky, M. S., McDowall, A. W., and Jensen, G. (2010). Bacterial TEM: new insights from cryo-microscopy. *Methods Cell Biol 96*, 21–45.

Pires, R., Hartlieb, B., Signor, L., Schoehn, G., Lata, S., Roessle, M., Moriscot, C., Popov, S., Hinz, A., Jamin, M.*, et al.* (2009). A crescent-shaped ALIX dimer targets ESCRT-III CHMP4 filaments. *Structure 17*, 843–856.

Saksena, S., Wahlman, J., Teis, D., Johnson, A., and Emr, S. (2009). Functional reconstitution of ESCRT-III assembly and disassembly. *Cell 136*, 97–109.

Samson, R. Y., Obita, T., Freund, S. M., Williams, R. L., and Bell, S. D. (2008). A role for the ESCRT system in cell division in archaea. *Science 322*, 1710–1713.

Samson, R. Y., Obita, T., Hodgson, B., Shaw, M. K., Chong, P. L., Williams, R. L., and Bell, S.D. (2011). Molecular and structural basis of ESCRT-III recruitment to membranes during archaeal cell division. *Mol Cell 41*, 186–196.

Stuchell-Brereton, M. D., Skalicky, J. J., Kieffer, C., Karren, M. A., Ghaffarian, S., and Sundquist, W. I. (2007). ESCRT-III recognition by VPS4 ATPases. *Nature 449*, 740–744.

Suloway, C., Pulokas, J., Fellmann, D., Cheng, A., Guerra, F., Quispe, J., Stagg, S., Potter, C. S., and Carragher, B. (2005). Automated molecular microscopy: the new Leginon system. *J Struct Biol 151*, 41–60.

Tocheva, E. I., Matson, E. G., Morris, D. M., Moussavi, F., Leadbetter, J. R., and Jensen, G. (2011). Peptidoglycan remodeling and conversion of an inner membrane into an outer membrane during sporulation. *Cell 146*, 799–812.

Wollert, T., and Hurley, J. (2010). Molecular mechanism of multivesicular body biogenesis by ESCRT complexes. *Nature 464*, 864–869.

Wollert, T., Wunder, C., Lippincott-Schwartz, J., and Hurley, J. (2009a). Membrane scission by the ESCRT-III complex. *Nature 458*, 172–177.

Wollert, T., Yang, D., Ren, X., Lee, H. H., Im, Y. J., and Hurley, J. (2009b). The ESCRT machinery at a glance. *J Cell Sci 122*, 2163–2166.

Xiao, J., Chen, X. W., Davies, B. A., Saltiel, A. R., Katzmann, D. J., and Xu, Z. (2009). Structural basis of Ist1 function and Ist1-Did2 interaction in the multivesicular body pathway and cytokinesis. *Mol Biol Cell 20*, 3514–3524.

Zhai, Y., Chong, P. L., Taylor, L. J., Erlkamp, M., Grobelny, S., Czeslik, C., Watkins, E., and Winter, R. (2012). Physical properties of archaeal tetraether lipid membranes as revealed by differential scanning and pressure perturbation calorimetry, molecular acoustics, and neutron reflectometry: Effects of pressure and cell growth temperature. *Langmuir 28*, 5211–5217.

CHAPTER 2:

HIV CAPSID ASSEMBLY

2.1

INTRODUCTION

The human immunodeficiency virus (HIV) packages its genome and enzymes into a conical structure called the capsid. It is unknown what role the capsid plays in the HIV lifecycle, but without it, the virus is noninfectious. HIV exits cells in an immature, noninfectious state without a capsid and must undergo a maturation process in order to assemble the capsid and infect a new cell. There have been many studies in the last few years to determine the structure of the mature HIV capsid (Pornillos, et al., 2001; Benjamin et al., 2005; Briggs et al., 2006) however it remains unknown how the capsid assembles. Understanding this process will lead to further understanding of the viral lifecycle and possibly to the development of a new therapeutic or prophylactic drug.

In order to characterize the assembly process of HIV capsids, I conducted two projects. In the first, I analyzed cryotomograms of unclosed (aberrant) HIV and EIAV capsids. This was important because the unclosed capsids represent misassembly and provide evidence to help deduce steps of the successful process. This study was in combination with collaborations in coarse-grain modeling and fluorescence microscopy *in vivo*. Chapter 2.2 is the manuscript currently undergoing revisions for the *Journal of Molecular Biology*.

In the second project, I initiated a set of experiments to repeat a study performed in 1999 (Davis, 1999). The authors claimed to have imaged intermediate maturation steps in HIV capsids, but the imaging technology at the time did not allow for high enough resolution to gain any knowledge about the intermediate structure. By repeating the protocol and imaging with state-of-the-art electron cryotomography, I expected to resolve the intermediate maturation stages. However, this project was not completed since the results could not be consistently repeated by Western blot, and more work

needs to be done to optimize the conditions. Chapter 2.3 summarizes my work to repeat the experiment.

2.2

UNCLOSED HIV-1 CAPSIDS SUGGEST A CURLED SHEET MODEL OF ASSEMBLY

Zhiheng Yu[1#], Megan J. Dobro[2#], Artem Levandovsky[3], Cindy M. Danielson[4], Virginie Sandrin[5], Jiong Shi[6], Christopher Aiken[6], Roya Zandi[7], Thomas J. Hope[4], Grant J. Jensen[2,8*]

[1] CryoEM Shared Resources, Janelia Farm Research Campus, HHMI, 19700 Helix Drive, Ashburn, VA 20147, USA

[2]Division of Biology and [8]Howard Hughes Medical Institute, California Institute of Technology, 1200 E California Blvd, Pasadena, CA 91125, USA

[3]2442 Iowa Ave, Q12, Riverside, CA. 92507, USA

[4]Department of Cell and Molecular Biology, Feinberg School of Medicine, Northwestern University, 303 East Superior Ave, 9-290 Lurie, Chicago, IL, 60611, USA

[5]Department of Biochemistry, University of Utah, 15 N Medical Drive, East RM 4100, Salt Lake City, UT, 84112-5650, USA

[6]Department of Pathology, Microbiology and Immunology, Vanderbilt University School of Medicine, A-5301 Medical Center North, Nashville, TN 37232-2363, USA

[7]Department of Physics and Astronomy, University of California, Riverside, CA 92521, USA

[#]authors contributed equally to work

*Correspondence should be addressed to GJ: jensen@caltech.edu, 626-395-8827

Abstract

The RNA genome of retroviruses is encased within a protein capsid. The function of this capsid is unknown, but one possibility is that it protects the RNA from degradation. To study the assembly and function of this capsid, electron cryotomography (ECT) was used to image noninfectious HIV particles and isolated equine infectious anemia virus (EIAV) cores. While the majority of cores appeared closed, a variety of unclosed forms were also seen including rolled sheets, extra flaps, and tip holes. Simulations of nonequilibrium growth of elastic sheets recapitulated each of these aberrations and further predicted the occasional presence of seams, for which evidence was seen in the cryotomograms. Together, these findings suggest a new pathway for HIV assembly that involves the union in space of two edges of a curling sheet. Consistent with the observation that viral capsids can be incomplete, we observed that a fluid-phase marker of capsid integrity was lost in a subset of cytoplasmic HIV complexes captured by TRIM5alpha. This reveals that approximately 25% of capsids within the cytoplasm have holes large enough to allow GFP to leak out of the conical capsid structure. Since a quarter of all capsids contain holes large enough for GFP to pass through, it is likely that ribonucleases in the cytoplasm could also enter the viruses. Therefore, the main role of the HIV-1 capsid may not be to protect the viral genome, as previously thought.

Author Summary

The viral capsid is the protein shell that encloses the genetic material and enzymes and enters the infected cell. The structure of the HIV-1 capsid has been well characterized and is an important potential target for retroviral therapy, however the mechanism of capsid assembly remains unknown. Using electron cryotomography, simulations, and *in vivo* fluorescent imaging, we analyzed the structural details of irregular capsids from HIV-1 particles and equine infectious anemia virus. We show that

capsids are capable of forming rolled sheets and extra flaps, and sometimes contain holes, in addition to closed capsids. These structures provide present evidence consistent with a curling sheet mechanism for the assembly of conical capsids of HIV-1. In addition, the frequency of holes in the capsid large enough for GFP to easily pass through indicates the role of capsid may not be to protect the viral genome, as previously believed.

Introduction

The major structural protein of HIV is the Gag polyprotein, which organizes the budding virion and binds to the membrane through its myristoylated N-terminus. The particle buds from the cell as an immature, noninfectious virion, and then matures to produce the infectious particle. During viral maturation, Gag is cleaved in five positions by the viral protease (PR), thereby producing the MA, CA, and NC proteins (Vogt, 1997; Pettit et al., 1998) as well as several smaller peptides (SP1, SP2, and p6). MA, CA, and NC then reassemble to form the mature virion in which the myristoylated MA protein remains associated with the membrane; NC binds to the viral RNA; and CA forms the conical capsid that forms the outer shell of the core particle that encloses NC, the RNA genome, reverse transcriptase (RT) and integrase (IN) and Vpr (Vogt, 1997). Proteolytic cleavage at either end of CA induces conformational changes that allow CA to assemble into the hexamers and pentamers that comprise the conical capsid (Gitti et al., 1996; Gamble et al., 1997; Swanstrom and Wills, 1997; Bartonova et al., 2008).

The HIV capsid is crucial for the delivery of the RNA genome to a newly infected cell, interactions with host cell restriction factors, reverse transcription (Zhang et al., 1996; Forshey et al., 2002; Arhel et al., 2007) and transport to the nucleus (Mcdonald, 2002; Dismuke and Aiken, 2006). It is therefore a potential drug target (Sundquist and Hill, 2007). The conical capsid is an intriguing structure but authentic capsids have been difficult to study owing to their heterogeneity and instability during purification. High-

resolution information about the structure of the mature capsid could give insight into its assembly process, and perhaps even into the purpose of the capsid altogether.

Direct imaging of *in vitro* CA assemblies (tubes, planar sheets, and *in vitro*-assembled cones) using electron microscopy (EM) led to the model that capsids are closed fullerene cones (Cardone et al., 2009; Ganser et al., 2003; Ganser et al., 1999; Ganser-Pornillos et al., 2007; Li et al., 2000). Most of the cone comprises CA hexamers, but twelve pentamers are also incorporated to close the shell: typically five at the narrow end and seven at the broad end. Crystal structures have provided high-resolution details of the CA domains as well as hexamers and pentamers (Gitti et al., 1996; Momany et al., 1996; Gamble et al., 1997; Ganser-Pornillos et al., 2007). Taken together, these studies have established the interactions of each CA domain and clearly defined the hexagonal lattice of the capsid shell. It remains unclear, however, how the capsid cone self-assembles from its constituent protein subunits. It has been assumed that the infectious capsid cone is completely closed (Ganser et al., 1999; Li et al., 2000; Sundquist and Hill, 2007) in part because when many surface mutations in CA were tested for effects on features such as morphology and infectivity, mutations that affected capsid morphology also rendered the preparations noninfectious (von Schwedler et al., 2003).

Two "end-to-end" models for capsid assembly have been proposed. In 2005, Benjamin et al. studied HIV particles using electron cryotomography (ECT), observing similarities in the size and shape of the wide end of the capsid, uniform positioning of the wide end 11 nm away from the envelope, a cone angle of 18°–24° around the long axis, a frequent hole at the tip of the narrow end, and the NC/RNA complex density situated inside the capsid toward the wide end. These observations led to a model of capsid assembly nucleating around NC/RNA density at the wide end and growing toward the narrow end. Additionally, multiple and sometimes nested (multilayered) capsids were

also seen. In 2006, Briggs et al. confirmed these results, also reporting a cone angle of 19° around the long axis and the NC/RNA density situated in the broad end. Noting that cores always spanned the full distance across the typically spherical membrane envelope, however, they proposed that capsid assembly begins at the narrow end and grows across the viral particle until it reaches the membrane on the opposite side, which then redirects growth toward closure of the wide end.

A third proposal is that assembly does not follow a strictly "end-to-end" pathway but the CA hexamers form a curved sheet that curls over and seals without a template (see Figure 2.4) (Levandovsky and Zandi, 2009). According to this model, new protein subunits attach to sites that maximize the number of intermolecular bonds. The assembly is done under nonequilibrium conditions in which once a pentamer or hexamer is formed, it can no longer dissociate or switch to the other one. As the curved sheet composed of CA hexamers grows, at some point inclusion of pentamers becomes necessary to relieve accumulated stress. Simulations of capsid growth following such simple rules have recapitulated spherical, conical, or tubular shapes depending on the intrinsic curvature of the protein subunits. In the case of cones, since the subunits "prefer" to form hexamers rather than pentamers, edges of growing sheets curl around and unite before the top and bottom tips close (see Figure 2.4). It is important to note that the switching between hexamers and pentamers during the growth process is crucial for formation of highly symmetric spherical capsids with icosahedral symmetry, where their structures are well explained through equilibrium theories.

The structure of the capsid gives insight to its function. Although it has been suggested that the capsid protects the RNA from host nucleases (Tanchou et al., 1995), if there are often gaps in the shell large enough for nucleases to pass through, the capsid cone would not be an effective barrier. Ribonucleases are generally 35-45 Å (Laurents et

al., 2009; Tanaka et al., 2004) in their smallest dimensions, and are therefore too large to fit through the holes of the closed hexagonal lattice (~25Å) (Li et al., 2000). However, it has been unclear whether larger gaps in the assembled structure are common.

Electron cryotomography (ECT), in which vitreously-frozen samples are tilted along an axis to collect three dimensional (3D) information, is the highest resolution technique available to image unique objects such as retroviral capsids (Owen, 2008; Pilhofer et al., 2010). As mentioned above, we previously used ECT to visualize the diversity of 3D structures seen within HIV-1 particles, with a particular focus on the capsids that exhibited the canonical cone shape (Benjamin et al., 2005). Equipped with an improved camera on our cryo-EM, here we have re-imaged HIV-1 particles in hopes of obtaining higher resolution. To reduce ice thickness and remove surrounding density, we have also isolated and imaged cores from equine infectious anemia virus (EIAV). EIAV cores were used because they are more stable and easier to purify than their HIV-1 analogs. Although there are subtle differences in the crystal structures of EIAV CA and HIV-1 CA, both have the same overall fold, contain the highly conserved major homology region and assemble into capsids of very similar structure (Egberink et al., 1990; Goudsmit et al., 1986). It is thought therefore that EIAV cores are good models of HIV (Jin et al., 1999). The new data and higher resolution called our attention in particular to interesting similarities between the minority classes of unclosed cores and the predictions of a nonequilibrium growth of an elastic sheet model published two years ago (Levandovsky and Zandi, 2009). Evidence is presented here from both HIV-1 and EIAV that some retroviral cores are unclosed, exhibiting features such as rolls and gaps and perhaps seams. Using GFP as an intravirion fluid phase marker, we confirm that a subset of capsids in the cytoplasm have holes large enough for GFP to leak out of the structure. These observations point to an assembly process that involves opposite edges of a sheet

curling over and joining, as predicted by the nonequilibrium studies of growth of an elastic sheet.

Results

Capsid Imaging

Electron cryotomograms were recorded of 37 HIV-1 particles with the new lens-coupled CCD camera. For safety, the viral particles were made noninfectious with single amino acid mutations in reverse transcriptase and RNase, but the remaining genes were

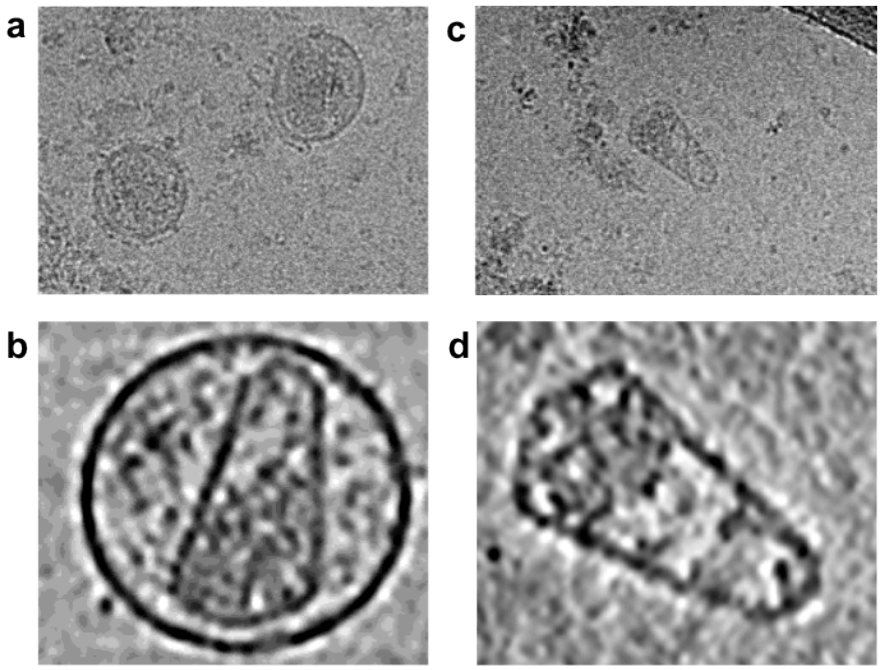

Figure 2.1. Cryotomographic reconstructions. Top row: Cryo-EM projection images through frozen-hydrated HIV-1 VLPs (a) and purified EIAV cores (c). Bottom row: Enlarged slices through the corresponding 3-D reconstructions of HIV-1 VLPs (b) and purified EIAV cores (d) showing typical cone-shaped cores with nucleoprotein density concentrated near the base.

wildtype. To reduce the material around the capsid and promote thinner ice, the larger and more robust cores from EIAV virions were purified and 22 were imaged. Figure 2.1 shows representative projection images and tomographic slices through these samples.

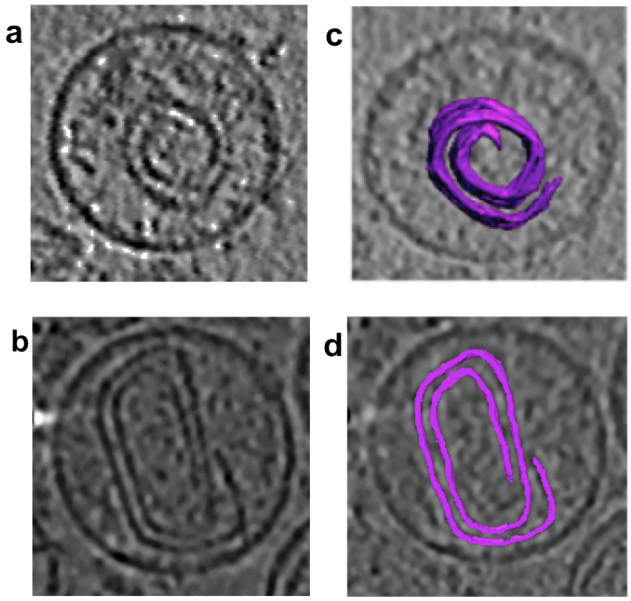

Figure 2.2. Rolled sheets. (a)–(b) Tomographic slices through HIV-1 VLPs containing rolled capsid sheets. (c)–(d) Corresponding 3D segmentations.

In 2 of the HIV-1 particles, instead of the typical conical cores, rolled sheets without closed caps at the top or bottom were seen (Figure 2.2). The rolled sheets were clear in the tomograms (Figure 2.2a and b), but were segmented in 3D for emphasis (Figure 2.2c and d). In another 2 of the 37 HIV-1 particles, extra capsid sheets were seen next to more nearly closed cores (Figure 2.3). The extra sheets adopted curvatures similar to the cores next to them (curved in Figure 2.3a and flat in Figure 2.3b), but were apparently unconnected. Such extra sheets are perhaps to be expected, since there are likely ~3500 CA monomers in a full immature shell and only 1000-1500 are required to make a typical cone-shaped capsid. (The exact numbers of CA monomers in immature shells is uncertain: the size of immature particles and the 8-nm hexagonal Gag lattice could allow up to ~5000 monomers (Benjamin et al., 2005), but tomography of immature particles

revealed that the Gag lattice is incomplete (Wright et al., 2007), so the actual number of CA monomers is likely lower (Briggs et al., 2004; Kelly et al., 2006; Wright et al., 2007)). The remaining particles imaged were cone-shaped, and were either intact or contained holes.

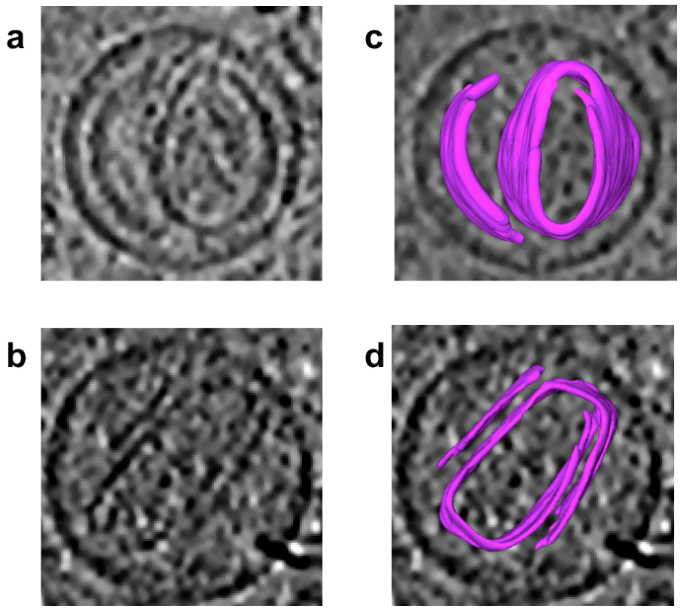

Figure 2.3. Extra capsid sheets. (a)–(b) Tomographic slices through HIV-1 VLPs exhibiting an extra capsid sheet. The extra sheet adopts a similar curvature to the capsid but is not connected. (c)–(d) Corresponding 3D segmentations.

Simulation of Capsid Growth

The presence of capsid gaps and defects were predicted by simulations of nonequilibrium growth of elastic CA sheets by Levandovsky and Zandi (Levandovsky and Zandi, 2009b). These simulations explored how compressible triangular-prism-shaped 3-D "subunits" (Figure 2.4a) modeled as spring networks designed to mimic CA proteins would link together and grow into 3-D structures (Movie 2.1). The choice of subunits was based on the fact that CA proteins must be flexible enough to be able to assemble

and sit in different or “non-equivalent” positions along the curving body of the conical capsid. During assembly, subunits were added one by one to a growing sheet, and the spring network was allowed to relax before the next prism was added.

The process of assembly was chosen to be irreversible in that once a pentamer or hexamer formed, it could no longer dissociate. To take into account the intrinsic curvature of protein subunits, tapered prisms with a larger “top” than “bottom” were considered (Figure 2.4a). The curvature of the growing shell depended upon the intrinsic curvature or “preferred dihedral angle” between protein subunits. As the curved sheet grew, strain within the network increased, until it became energetically more favorable to close a pentameric ring than to squeeze in a sixth subunit to form a hexamer.

In later stages of growth, the elastic sheet comprised a considerable number of hexamers and a few pentamers, and curled until the edges met (Figure 2.4f). Finally, the tops and bottoms of the resultant structures filled in even though the energetic costs of sealing the caps was high compared to building the lateral walls (Figure 2.4h). Depending on the protein subunit’s intrinsic curvature, spherical, tubular or conical structures formed, recapitulating the various shapes exhibited by retroviral capsids (Levandovsky and Zandi, 2009).

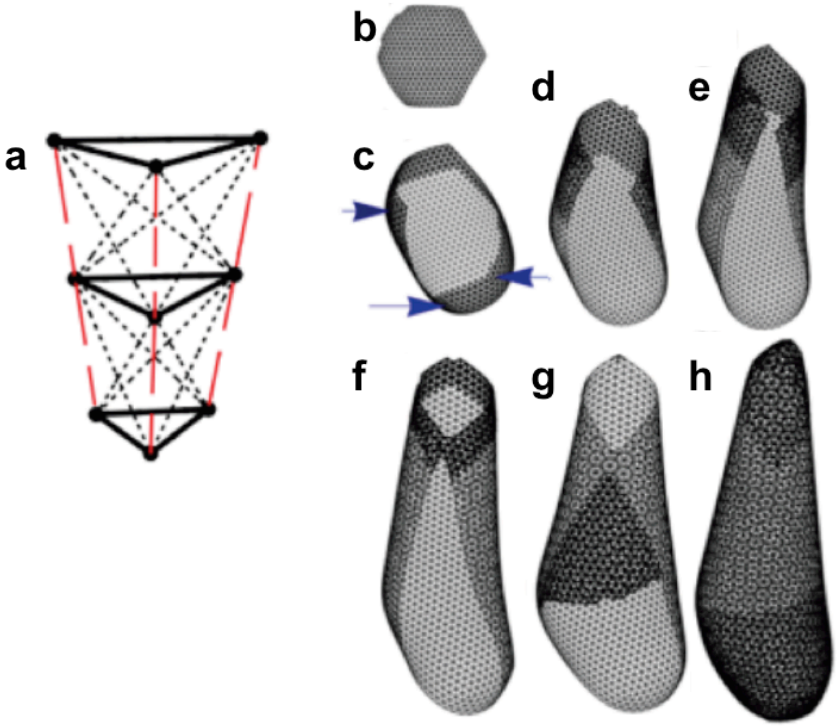

Figure 2.4. Nonequilibrium growth of elastic sheets. (a) 3-D triangular prism monomers modeled by nine points connected by three different types of springs, each with their own parameterized spring constant. (b-h) Snapshots of sheet growth and capsid completion. Triangular prisms are added one-by-one to the edge where the most contacts will be formed, and then strain in the spring network is allowed to redistribute after each addition (b). Because the prisms are angled, eventually insertion of a pentamer becomes favored (blue arrows in (c)). Later sheets curl over on themselves and two edges meet (f), followed by tip closure (h). Reproduced from Levandovsky and Zandi, 2009.

Stochasticity was introduced into these simulations by randomly choosing where the next prism would join from amongst equal positions along the edge of the growing sheet. Although only closed structures were discussed in the original paper (Levandovsky and Zandi, 2009), unclosed structures were observed frequently with introduction of stochasticity. In some cases, the edges of the curling sheet failed to unite in space, producing structures that closely resembled the rolled sheets shown in Figure 2.5. In addition, high curvature tips always closed last, and were much more costly to form (in

terms of compression and stretching of subunits) than lateral walls (Figure 2.6c). In some cases, different growth rates around the edge of the closing structure led to mismatches at the tip (Figure 2.6a). Evidence of similar issues in the closure of real capsids was present in the tomograms (Figure 2.6b). As reported by Benjamin et al. in 2005, when 16 conical cores were aligned at their narrow tips as well as possible (Figure 2.6e) and averaged, the lateral walls of the capsid remained clear, but there was a conspicuous absence of density at the tip where the alignment should have been best (Figure 2.6f). This suggests that tips frequently (perhaps usually) remain unclosed.

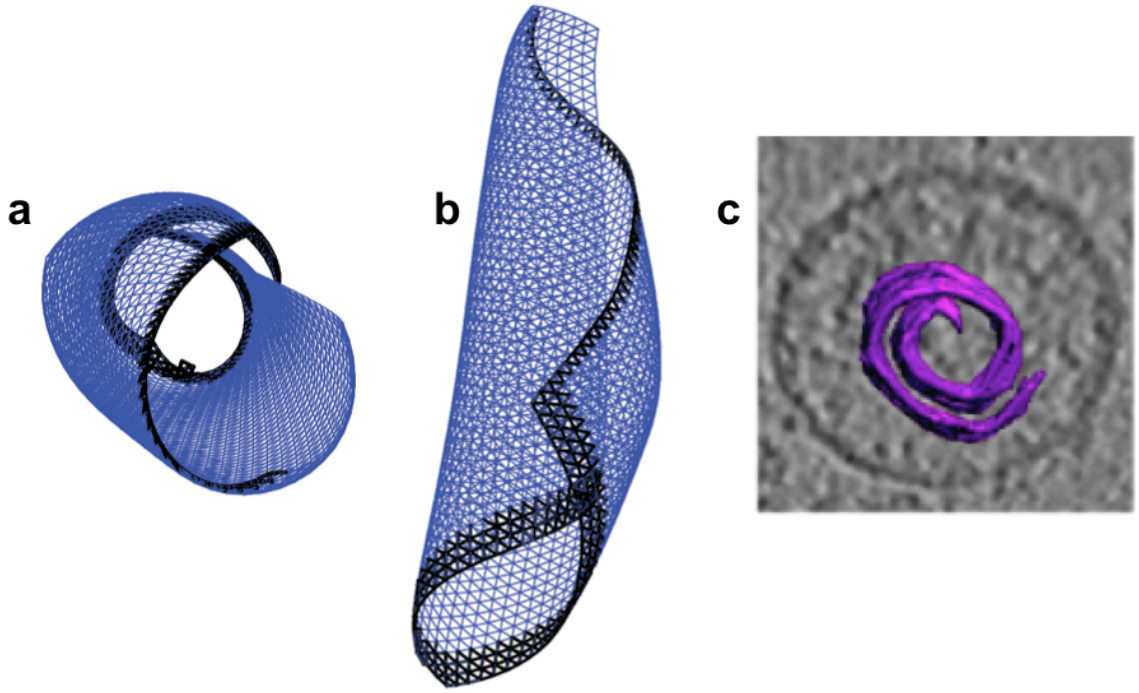

Figure 2.5. Example of a simulated rolled sheet. (a) Example simulated structure where the curling edges of the growing sheet failed to meet, resulting in a roll. (b) Same structure as in "a," rotated 90°. (c) 3D segmentation of an apparently similar capsid roll seen in an actual HIV VLP (same as in Figure 2.2c)

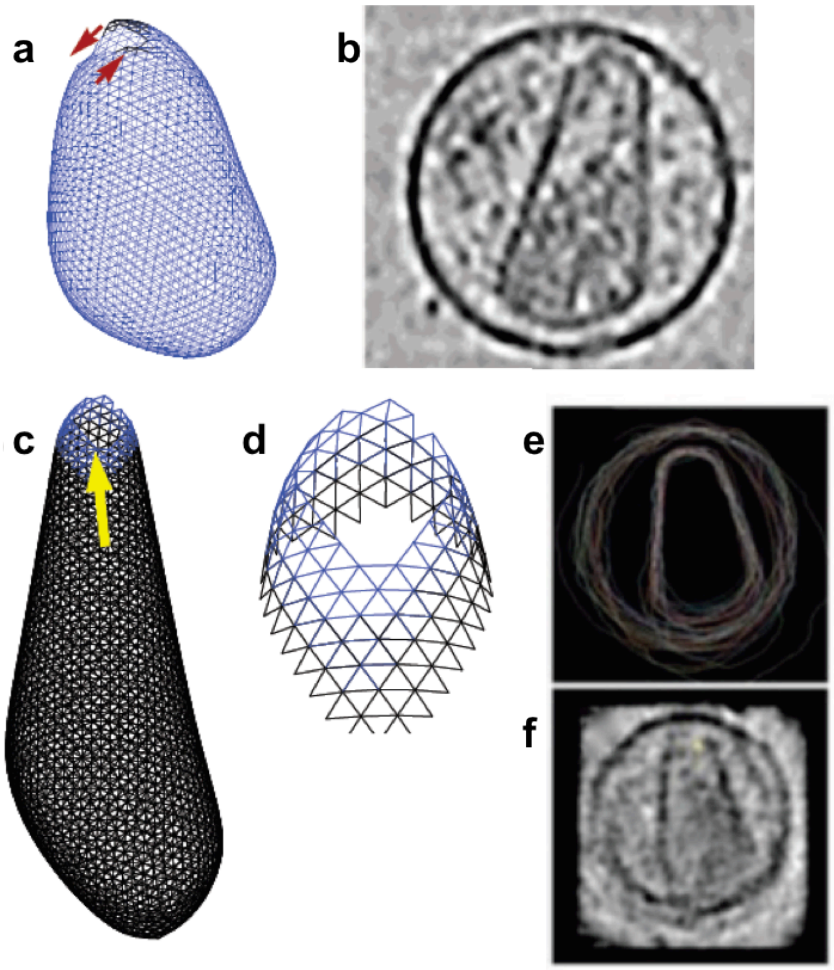

Figure 2.6. Tip holes are predicted by closure strains. (a) Example simulated structure illustrating how nonequilibrium growth can lead to tips with strained gaps. (b) Tomographic slice through an apparently similar VLP. (c) Second example of a simulated structure just before tip closure. (d) Enlarged view of tip in panel (c). (e) Traces of 16 cone-shaped cores and their corresponding envelopes aligned to best superimpose their tips. (f) Resulting average density showing hole in the tip. (e) and (f) reproduced from Benjamin et al., 2005.

Seams

As mentioned in the previous section, the assembly process involves subunits randomly placed in one of the equivalent positions along the edge of the growing sheet, and this can lead to the distribution of capsid shapes. When two edges of the sheet met in the simulations, a line of defects (holes) sometimes formed (Figure 2.7 and Movie 2.2). For example, merging edges in Figure 2.7a are not smooth but have small protrusions leading to the formation of a seam in Figure 2.7b.

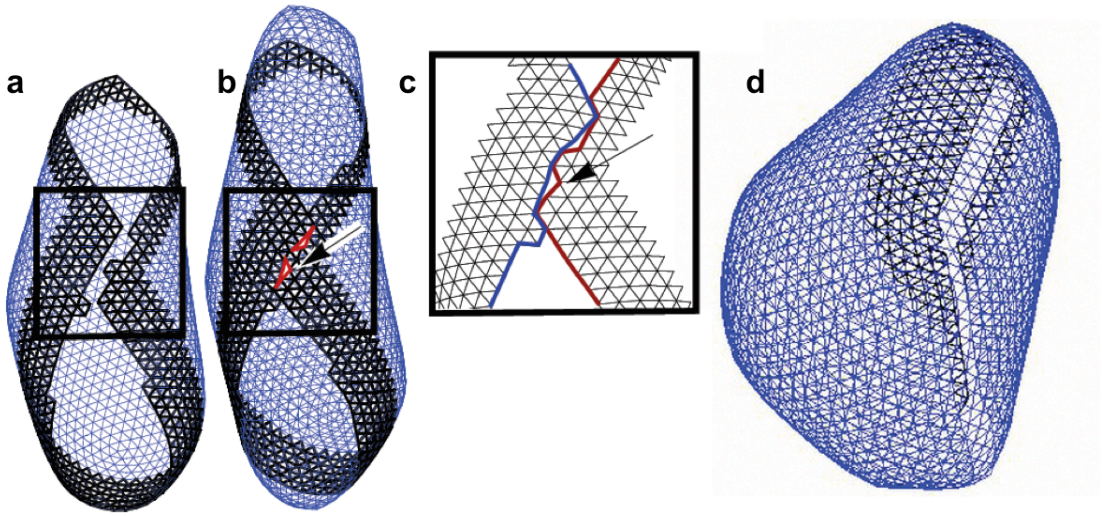

Figure 2.7. Misalignments in simulations can result in seams of small gaps. (a) and (b) Snapshots of a simulation, just before and after merging, where misalignment of the curling edges prevent complete closure. (c) Enlarged view of final seam. (d) Second example of a long seam.

While the resolution obtained in the cryotomograms was insufficient to verify with certainty whether such defects exist in real viral particles, evidence supporting their existence was found in both the EIAV purified cores and the HIV-1 particles (Figure 2.8). Isosurfaces of each core were generated by thresholding the density of tomographic data to a level where the shape of the capsid was most clearly apparent. Typically, hexamers were discernable over parts of the surface (Figure 2.8c and d), confirming the expected

lattice structure of mature cores (Ganser et al., 1999; Ganser-Pornillos et al., 2007; Pornillos et al., 2011). When the threshold was lowered further, however, holes would usually appear uniformly over the entire surface, indicating that there were no special surfaces with lower density. In a subset of cases, however, the first holes appeared in a strikingly seam-like row as the threshold was lowered. Figure 2.8a shows tomographic slices though one EIAV core with density missing along a line parallel to the z-axis. Figure 2.8b shows the isosurface of that capsid and the positions of the planes shown in panel a. The seam of holes is easily detected at this threshold while the rest of the capsid is almost completely closed, exhibiting ridges that correspond to the hexameric CA lattice (backside shown in panel c). The insert shows the low-pass-filtered, mature HIV CA hexagonal lattice as determined by electron crystallography (Ganser-Pornillos et al., 2007). The individual CA hexamers have a diameter of 8 nm, which is consistent with the individual bumps seen on these capsid segmentations, showing we were able to resolve hexamers of CA in these samples.

The frequency of seams in cores is difficult to ascertain because the holes emerged in a continuum of different configurations, ranging from randomly positioned to approximately straight rows. Nevertheless, among the 37 HIV-1 virions, 8 appeared to have seams and among the 22 EIAV cores 10 appeared to have seams. More seams may have been detected in the EIAV cores because images had better signal-to-noise ratios because the samples were thinner. Putative seams were observed in many orientations with respect to the missing wedge, arguing against their being an artifact of the limited tilt range of electron microscope samples (Arslan et al., 2006). Furthermore, the seams in the EIAV cores were probably not purification artifacts because seams were also observed in the intact HIV-1 virions.

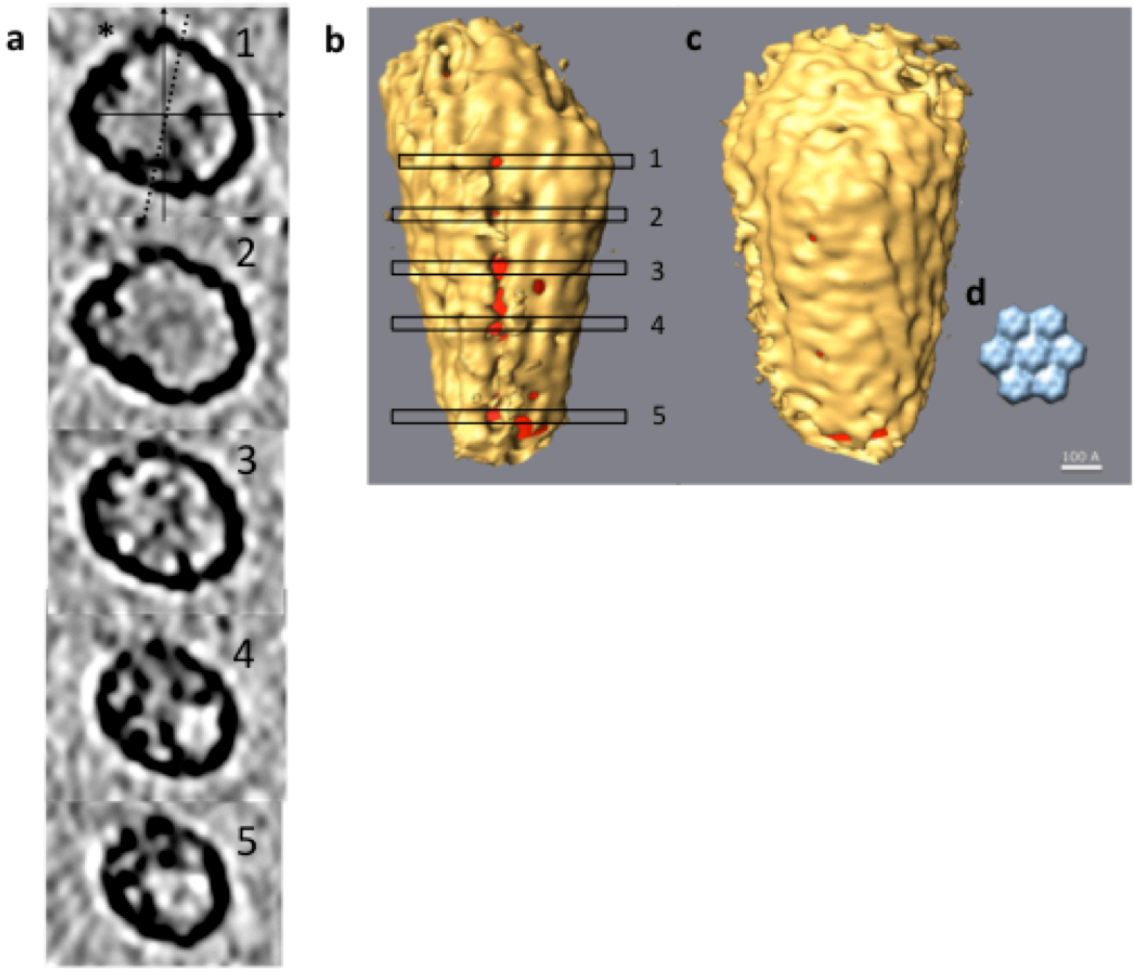

Figure 2.8. Evidence of a seam in a real core. (a) Tomographic slices of an isolated EIAV core perpendicular to the seam. The asterisk indicates the location of the various holes along the putative seam. This particular core froze in the ice with its long axis approximately perpendicular to the plane of the sample. The solid lines show the x- and y-axes, and the dotted line shows the tilt axis, showing that the seam is unlikely to be an artifact of the missing wedge. (b) Isosurface of the core with the seam facing front with the locations of the tomographic slices shown in (a) marked. The interior of the core is colored red to aid visualization. (c) Backside of the same capsid showing an otherwise mostly complete shell, including a putative pentamer (in center between levels 1 and 2). (d) Low-pass-filtered crystal structure of a CA hexamer for comparison.

Capsid Integrity in Cells

To determine whether authentic HIV capsids are intact during the early stages of infection, we developed a system in which GFP is initially present within the capsid, thereby allowing us to identify capsids with lattice gaps that are larger than GFP by loss of this fluid phase marker. This system utilized a virus developed by Chen and coworkers that contains GFP between MA and CA, flanked by HIV protease target sites (Hübner et al., 2007). In this system, GFP is packaged into the immature virion as a domain of Gag and then incorporated within the capsid following viral protease cleavage. As shown in Figure 2.9, a significant amount of free GFP co-sediments with viral cores purified from detergent-stripped virions, revealing that a subset of the protein resides within the viral capsid.

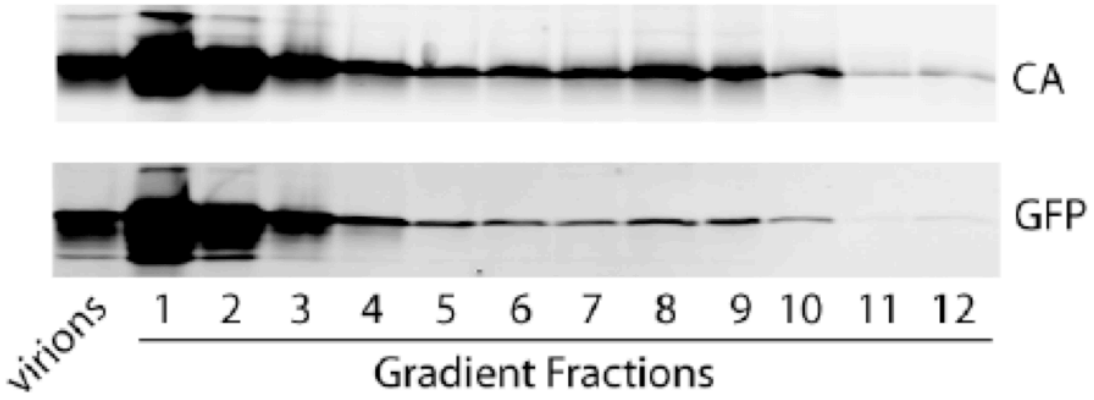

Figure 2.9. GFP comigrates with iGFP HIV cores in a sucrose gradient. Concentrated iGFP particles were subjected to equilibrium centrifugation through a layer of Triton X-100 into a linear sucrose density gradient. Fractions from the gradient were precipitated and analyzed by immunoblotting. Top panel shows detection of p24 (CA) while bottom panel shows detection of GFP. Numbers designate fractions collected from the top of the gradient. Capsids sediment to fractions 7-10. The first lane contains proteins extracted from intact iGFP virions.

To test whether these capsids retain their GFP during the early stages of viral infection, we utilized an assay in which uncoated cores are identified and captured by the restriction factor, rhTRIM5α, but prevented from dissociation by treatment with the proteasome inhibitor MG132. We have previously shown that under these conditions, rhTRIM5α recognizes and sequesters intact capsid cores, thereby blocking infection (Campbell et al., 2008). These captured complexes appeared to represent intact conical capsids because they contain abundant amounts of the CA protein as revealed by immunofluorescence staining.

To determine whether GFP is retained within the capsids that are captured by rhTRIM5α, we infected HeLa cells that stably expressed HA-tagged rhTRIM5α with the iGFP virus that was also been labeled with mCherry-Vpr. As rhTRIM5α recognizes the assembled capsid lattice, particles that label with mCherry-Vpr and rhTRIM5α must be mature viral cores that have not lost their capsids. Completely closed capsids should also contain free GFP, whereas cores with seams or other large openings would be expected to lose the free GFP while retaining mCherry-Vpr, enabling us to estimate the fraction of incompletely closed capsids. An example of this type of analysis is shown in Figure 2.10, where multiple mCherry-Vpr labeled complexes have been captured within rhTRIM5α cytoplasmic bodies. Image analysis software was used to count rhTRIM5α-associated virions and categorize them as either positive for both mCherry-Vpr and GFP (closed capsids), mCherry-Vpr only (incompletely closed capsids), or GFP only (incomplete mCherry-Vpr labeling). These analyses revealed that 25.0 ± 0.8 (s.e.m.)% of the mCherry-Vpr labeled cores lacked detectable GFP, and therefore likely represented cores that had capsid gaps large enough to lose GFP while retaining a largely intact capsid lattice. These results support the idea that a subset of authentic viral capsids has gaps that are large enough to allow loss of GFP from the core interior.

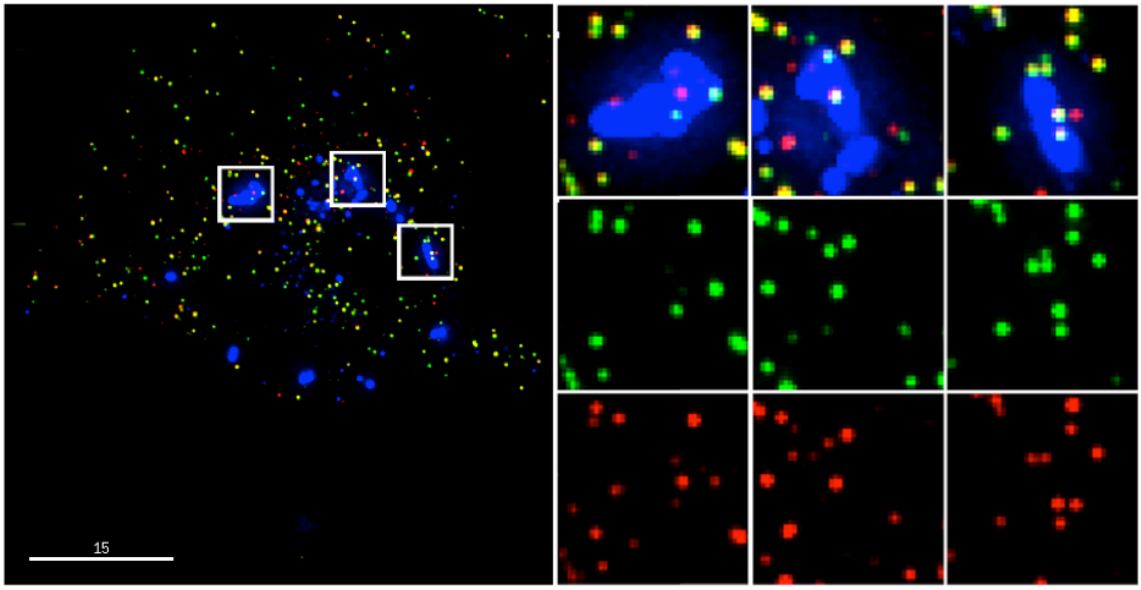

Figure 2.10. Capture of HIV capsids by TRIM5 alpha in the presence of proteasome inhibition. Only fused particles are captured in the complexes as previously reported. Captured mCherry-Vpr complexes were scored for the presence of the fluid phase marker GFP. We find that 25.0 ± 0.8 (s.e.m.) percent of the complexes lose the GFP marker indicating they are unclosed capsids.

Discussion

In 2005, Benjamin et al. proposed an end-to-end model in which the nucleation point of assembly is at the broad base of the cone and grows toward the narrow end. The evidence for this model was that conical cores had a consistent shape at the base, the density of the presumed nucleoprotein was frequently concentrated in the base, and holes were often seen at the narrow tip. In 2006, Briggs and colleagues suggested an opposite end-to-end model in which the capsid starts with a nucleation point at the narrow end of the core, and subunits are added with a consistent angle around the longitudinal axis until the opposing membrane is reached and growth is deflected inwards, leading to closure. However, strict nucleation models are inconsistent with the fact that HIV-1 CA can form cones of similar size and shape *in vitro* in the absence of membranes (Ganser et al., 1999).

Similarly, if capsids are assembled in a strictly end-to-end fashion, the unclosed capsids observed here (rolls, extra sheets, unclosed tips, and seams) would not be expected to form. Additionally, HIV capsids are variable in size and shape, which further supports the idea that they are assembled free from a fixed template. Instead, the unclosed forms seen here point to a model that involves the union in space of the edges of a curling sheet, as seen in recent simulations of the nonequilibrium growth of an elastic sheet. Rolls could be explained by the two growing edges missing each other in space, extra sheets could be explained by secondary nucleation sites, unclosed tips could be explained by the energetic strains encountered by high curvature, and seams could be explained by misalignment along edge junctions. Butan et al. recently showed a correlation between capsid morphology and the number of envelope glycoprotein spikes present in Rous sarcoma viruses (Butan et al., 2008). This correlation also suggests that capsids do not assemble strictly end-to-end across the viral interior, but rather are influenced as they grow by envelope spikes positioned all around the viral membrane. This could happen if small patches of capsid shell, for instances, existed in the vicinity of spikes, and later merged through edge growth.

Since there are apparently holes and cracks large enough for nucleases to pass through in many capsids, we speculate that the capsid's purpose is not to protect the viral genome from nucleases, but rather to catalyze reverse transcription (Zhang et al., 1996; Arhel et al., 2007), transport the HIV genome along microtubules towards the nucleus, and/or interact with the nuclear pore complex. Unfortunately, we do not know whether the unclosed particles are infectious, and so cannot comment on whether these defects inhibit function. Further structural studies of capsids *in vivo* immediately after entry into a cell may reveal the correlation between defects in the shell and the infectivity of the capsid. If full capsid closure is essential to the HIV life cycle, small molecules that

disrupt the natural curvature of growing capsid sheets or perturb the ratio of hexamers to pentamers may be effective anti-retroviral agents.

Materials and Methods

Mature HIV Particle Preparation

293T cells were seeded at 2.4×10^6 cells/10 cm plate a day before transfection. Each 10 cm plate of cells was transfected (CalPhos mammalian transfection kit; Clontech) with 8.1 μg of R9 ΔRT ΔRNase. After 36 h, the supernatants were harvested, filtered (0.45 μm pore size), and pelleted through a 4-ml 20% sucrose cushion in a Beckman SW-32Ti rotor (134,000 X g, 2 h, 4 °C). Each set of pelleted virions was resuspended in 50 μl of ST buffer and kept on ice until frozen on grid.

EIAV Core Isolation

EIAV cores were prepared as described in Langelier et al., 2008. Briefly, EIAV virions were produced by co-transfection of 293T cells with an EIAV vector system. Each 10 cm plate of cells was transfected (CalPhos mammalian transfection kit; Clontech) with 7.5 μg of pEV53 (EIAV structural proteins), 7.5 μg of pSIN6.1CeGFPW (packaged GFP expression vector), and 2.2 μg of phCMV- VSV-G (VSV-G envelope). After 36 h, the supernatants were removed, pooled (four plates/pool), filtered (0.45 μm pore size), and pelleted through a 4 mL 20% sucrose cushion in a Beckman SW-32Ti rotor (134,000 × g, 2 h, 4 °C). Each set of pelleted virions was resuspended by gentle pipetting (4 h at 4°C) in 400 μL of ST buffer (10 mM Tris-HCl [pH 7.4], 50 mM NaCl). Four 11.5 mL sucrose gradients (30% and 70% [wt/vol] sucrose in ST buffer) were prepared in 14-by-89 mm tubes using a gradient mixer (Biocomp). The gradients were overlaid with a 0.3 ml cushion of 15% sucrose containing 1% Triton X-100 and then with a 0.3 mL barrier layer of 7.5% sucrose in ST buffer. Each tube of concentrated EIAV particles was carefully

layered on top of a gradient and centrifuged in a Beckman SW-41 rotor (210,000 × g, 16 h, 4°C). Twelve 1 ml fractions were collected from the bottom of each tube, and fraction densities were measured by using a digital refractometer (Leica), and EIAV CA was assayed by Western blotting. Three 1 ml fractions of the correct density (1.22 to 1.26 g/mL) contained intact EIAV core particles and were pooled, repelleted by centrifugation in a Beckman SW-41 rotor (210,000 × g, 2 h, 4 °C), and resuspended in 50 μL of ST buffer and kept on ice until frozen on grids.

Cryo EM grid preparation

Quantifoil carbon grids with a hole size of 0.6 μm and spacing between holes of 1 μm were glow discharged. A 3 μL solution of 10 nm nanogold was applied to the carbon film and dried in a 60 °C oven. A 4 μL solution of either intact mature HIV particles, purified mature EIAV/HIV cores, or *in vitro* assembled mature HIV CA-NC cones was applied to the pre-treated Quantifoil grids. Excess solution was blotted away with filter paper in a 100% relative humidity chamber. Grids were plunged into liquid ethane using a Vitrobot. Freezing conditions varied for each session, but were optimized when cryo-grids had sample particles suspended in a thin layer of vitrified ice across the holes of carbon.

Electron Cryotomography

Cryo grids were transferred to a 300 kV FEI G2 Polara transmission electron microscope equipped with a field emission gun and energy filter. Data were collected on a Gatan Ultracam 4k by 4k lens-coupled CCD in the EFTEM mode with an energy slit width of 20 eV. Tilt series were collected within a range from −65 degrees to +65 degrees with a step size of 2 degrees, a total dose of 80–100 e/Å^2, and a defocus of −6-8 μm. The software package used to collect the tilt series was UCSF Tomo and the 3D reconstruction was done with IMOD using a weighted back-projection algorithm.

Tomographic slices of capsids with seams were created by fitting an ObliqueSlice in Amira to be perpendicular to the seams, or to the long axis of the cones in the case of the control.

Segmentation

The segmentations were done manually using the Amira package by selecting the darkest density through several slices. To generate the isosurface, subvolumes of tomograms containing regions of interest were cut and an isosurface was generated with UCSF Chimera. The threshold was chosen to minimize noise while maintaining the capsid density before holes appeared throughout. A red cylinder was fit inside the core using UCSF Chimera to highlight the holes in the capsid.

Simulations

The capsids were modeled as if made of sheets of thin elastic material with Poisson ratio equal to 1/3. Such artificial material for the simulated capsids was created by means of assigning specific values for spring constants within individual subunits. The equation of motion for a large set of such springs has the same solution as an equation of continuum elasticity resolved on capsid surface, with accuracy up to the second order in lattice spacing.

HIV Gag-iGFP Core Purification and Analysis

Viral cores were isolated from HIV-1 particles generated by transfection of 293T cells with the HIV-1 Gag-iGFP viral clone (Hübner et al., 2007) as previously described (Shah and Aiken, 2011). Fractions were collected from the top of the gradient, and the proteins were precipitated with trichloroacetic acid. The precipitated proteins were dissolved in Laemmli buffer and separated on 4%–20% polyacrylamide gradient gels and blotted to nitrocellulose. The blots were probed with a mixture of affinity-purified rabbit polyclonal antibodies against GFP-derived peptides (Clontech), followed by a

monoclonal antibody to HIV-1 CA (clone 183-H12-5C) with appropriate IR dye-conjugated secondary antibodies. Bands were detected with a LI-COR Odyssey.

HIV Gag-iGFP Fluorescent Imaging and Analysis

For fluid phase virus imaging experiments, HIV-1 Gag-iGFP virus was generated by transfection of 293T cells with HIV Gag-iGFP Δ env, mCherry-Vpr, and CMV VSV-G. Cells stably expressing HA-tagged rhTRIM5α (provided by Joseph Sodroski) were seeded onto coverslips treated with fibronectin (Sigma-Aldrich) and infected in the presence of 10 μg/mL DEAE-dextran and 1 μg/mL MG132 (Sigma-Aldrich). Cells were incubated at 37°C for 4 hours before fixing in 3.7% formaldehyde (Polysciences) in PIPES buffer. Coverslips were stained with rabbit-anti-HA (Sigma-Aldrich) at a 1:300 dilution to detect rhTRIM5α, followed by AMCA donkey-anti-rabbit (Jackson ImmunoResearch) at a 1:400 dilution, then mounted onto slides (VWR) using Fluoro-Gel (Electron Microscopy Sciences). Images were acquired and deconvolved on a DeltaVision microscope equipped with softWoRx software (Applied Precision). Images were analyzed using algorithms written for Interactive Data Language (IDL) to identify virions containing mCherry-Vpr (TRITC-positive) associated with rhTRIM5α (DAPI-positive) and determine whether they were also positive for fluid phase GFP (FITC-positive). Three independent experiments were performed, and a total of seven coverslips were analyzed. The proportion of incompletely closed virions (TRITC-positive, DAPI-positive, FITC-negative) in the text represents the mean ± SEM (N = 7).

Acknowledgments

This work was support in part by NIH Grant P50 GM082545 to WIS, TJH and GJJ, R01 AI076121 to CA, R01 AI407770 to TJH, NSF Grant DMR-06-45668 to RZ, the Beckman Institute at Caltech, gifts to Caltech from the Ralph M. Parsons Foundation,

the Agouron Institute, the Gordon and Betty Moore Foundation, and gifts to Northwestern from the James B. Pendleton Charitable Trust. The following was obtained from the NIH AIDS Research and Reference Reagent Program: 183-H12-5C hybridoma from Dr. Bruce Chesebro. We thank Dr. Ben Chen for providing the HIV Gag-iGFP plasmid, Dr. Joseph Sodroski for cells expressing rhTRIM5α, Dylan Morris for help with the simulations, and Drs. Wesley Sundquist and Edward Campbell for critical reading of the manuscript.

2.3

NEXT STEPS

Immature (Wright et al., 2007) and mature (Benjamin et al., 2005) HIV particles have been imaged to high resolution with electron cryotomography. The structure of the fullerene cone has been determined using several approaches, and we have classified the structures of the irregular, unclosed cores as well. However, intermediate capsids between the immature and mature state have yet to be visualized to high resolution. By capturing the HIV capsids at intermediate steps of assembly, we could follow the structural process involved in forming a capsid and understand a process that remains elusive.

There are a few methods by which researchers have attempted to identify capsids at intermediate stages. In 1999, Davis et al. used a protease inhibitor to maintain HIV particles in an immature state. By washing out the drug, the particles were allowed to progress through maturation in a synchronized fashion. Electron micrographs were shown of intermediate particles, but the imaging technology at the time was poor and the resolution of the images is too low to gain knowledge about the intermediate structures. I initiated a project to repeat the protocol and collect electron cryotomograms of these intermediate particles, which could help further our understanding of the assembly process.

To harvest the virus, I traveled to the lab of Wesley Sundquist at the University of Utah and collaborated with Devin Christensen. Plates of 293T cells were grown in DMEM medium with 10% FBS. The cells were washed with FBS and incubated for one minute with trypsin to unadhere them from the plate. All cells were combined in a 50 mL conical tube and counted with a hemacytometer. Cells were replated at 2.5 × 106 cells

per 10 cm plate with 10 mL media. The transfection was performed with the Clontech CalPhos Mammalian Transfection kit. The plasmids used to produce virus were HLox for packaging signal and GFP, and pCMV dR8.2 for the structural genes, and both were ampicillin resistant. Virions were harvested through 0.45 μm filters and purified through a 20% sucrose cushion in PBS and 5 μM protease inhibitors Indinavir or Ritonavir (except for control). Purified virions were resuspended in PBS with or without protease inhibitor and frozen in liquid nitrogen for storage and shipping to Caltech. Virions were thawed at room temperature and centrifuged in a Beckman TLA 100.3 rotor at 48,000 RPM (~100,000 × g) at 4 °C for 35 minutes. The pellet was resuspended in 1 mL PBS and protease inhibitor (except for control) and centrifuged again. The pellet was resuspended in 1 mL DMEM with 10% FBS without drug to commence maturation, and maintaining drug in one case for a control. In half of the tubes I added 50 mM DTT after the first time point to speed the maturation reaction. I took two 10 μL aliquots at time points 0, 1, 4, 8, 20, and 24 hours. One half of the tubes from each time point was used for Western blots and the rest were plunge frozen on EM grids for imaging.

Western blots showed the virions never exposed to protease inhibitor were mature throughout the time course (Figure 2.11). The virions remained immature when kept in the presence of either Indinavir or Ritonavir protease inhibitor (Figure 2.12). A further experiment showed the drug maintained immature particles at 1 μM concentration but not at 200 nM. When drug was washed out, the particles were mature at the first time point of 1 hour (Figure 2.13). The conclusion was that the time points needed to be taken within the first hour to capture intermediates. This was a significant difference to the experiment published in 1999 when the particles took 24 hours to mature, but the use of a different protease inhibitor may be the cause. The original protease inhibitor used is now off the market, and therefore unavailable.

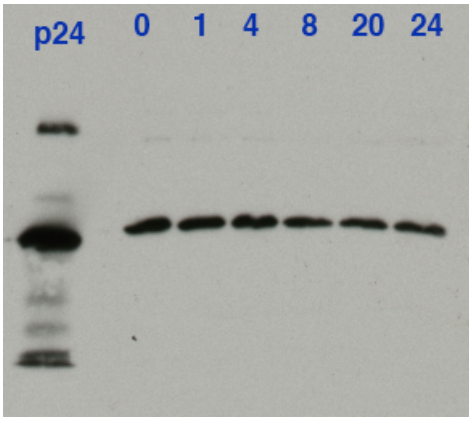

Figure 2.11. HIV particles mature without presence of protease inhibitor. The time course began after particles were harvested, purified, and concentrated. Each column represents the number of hours into the time course. The far left column was the control of p24, the main protein of mature HIV capsids. This Western blot shows that particles were mature before the time course began and remained mature.

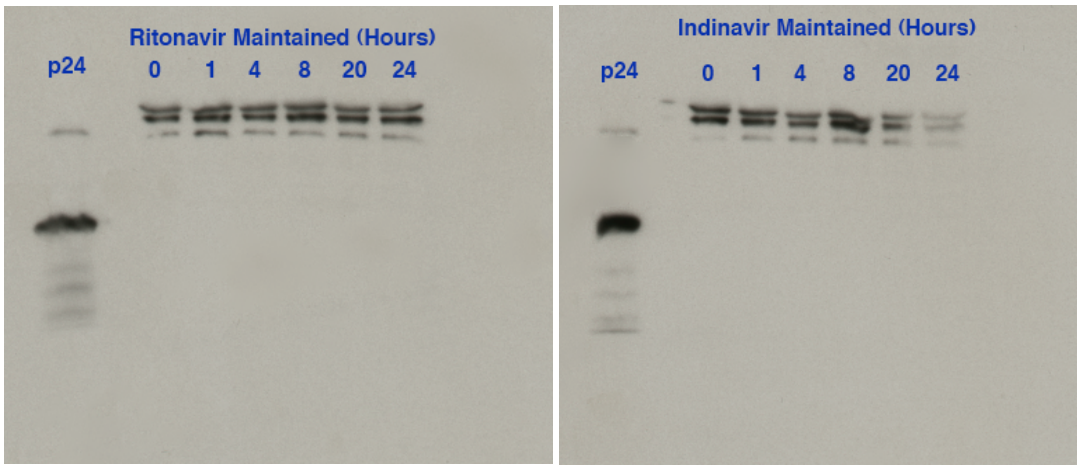

Figure 2.12. Both protease inhibitors maintain immature particles. A concentration of 5 μM of each protease inhibitor was maintained throughout the harvesting, purification, concentration, and time course of the particles. The particles remained in an immature state as seen by the lack of p24 (mature capsid protein) present.

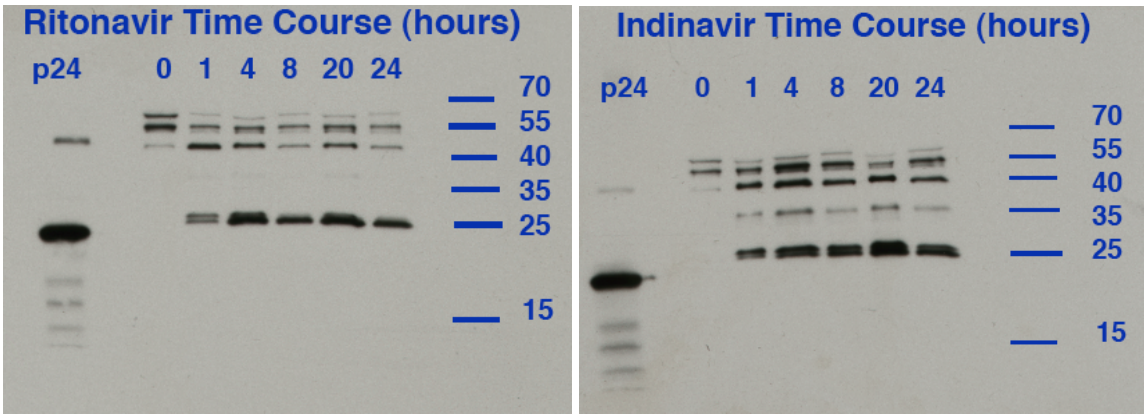

Figure 2.13. Particles mature before 1 hour after protease inhibitors are washed out. Protease inhibitors were maintained in the media with particles during harvesting, purification, and concentration. The time course began when the drugs were washed out, and p24 was not present when the time course began, but was present at 1 hour.

In the second run of the experiment, I collected aliquots of maturing virions at 17 different time points between 0 and 76 minutes. However, because the time points were so close together, there was not enough time to incubate the virions at 37 °C and were therefore kept at room temperature. Presumably it was because of this difference that all particles were immature. I repeated the experiment, keeping the tubes in a 37 °C water bath while drawing aliquots at each time point. In this case, and every iteration of the experiment after, the Western blot results were contradictory, showing a non-gradual maturation. Some time points displayed mature particles earlier than later lanes that displayed immature particles in the Western blots. These contradictory results were likely due to clumping of virions. Future attempts will normalize the virions or try other mixing strategies such as vortexing.

Additionally, the virions could be moved to 4°C and allowed to mature over several days. This slower maturation will provide a longer time frame for isolating intermediate particles. There are also temperature-sensitive protease inhibitors that could be used to commence the maturation.

REFERENCES

Arhel, N., Souquere-Besse, S., Munier, S., Souque, P., Guadagnini, S., Rutherford, S., Prévost, M., Allen, T., and Charneau, P. (2007). HIV-1 DNA Flap formation promotes uncoating of the pre-integration complex at the nuclear pore. *EMBO* J *26*, 3025-3037.

Arslan, I., Tong, J., and Midgley, P. (2006). Reducing the missing wedge: High-resolution dual axis tomography of inorganic materials. *Ultramicroscopy 106*, 994-1000.

Bartonova, V., Igonet, S., Sticht, J., Glass, B., Habermann, A., Vaney, M.-C., Sehr, P., Lewis, J., Rey, F.A., and Kraüsslich, H.-G. (2008). Residues in the HIV-1 capsid assembly inhibitor binding site are essential for maintaining the assembly-competent quaternary structure of the capsid protein. *J Biol Chem 283*, 32024-32033.

Benjamin, J., Ganser-Pornillos, B.K., Tivol, W.F., Sundquist, W.I., and Jensen, G. (2005). Three-dimensional structure of HIV-1 virus-like particles by electron cryotomography. *J Mol Biol 346*, 577-588.

Briggs, J.A., Simon, M.N., Gross, I., Kräusslich, H.G., Fuller, S.D., Vogt, V.M., and Johnson, M.C. (2004). The stoichiometry of Gag protein in HIV-1. *Nat Struct Mol Biol 11*, 672-675.

Briggs, J.A.G., Grünewald, K., Glass, B., Förster, F., Kräusslich, H.-G., and Fuller, S.D. (2006). The mechanism of HIV-1 core assembly: insights from three-dimensional reconstructions of authentic virions. *Structure 14*, 15-20.

Butan, C., Winkler, D.C., Heymann, J.B., Craven, R.C., and Steven, A.C. (2008). RSV capsid polymorphism correlates with polymerization efficiency and envelope glycoprotein content: implications that nucleation controls morphogenesis. *J Mol Biol 376*, 1168-1181.

Campbell, E.M., Perez, O., Anderson, J.L., and Hope, T.J. (2008). Visualization of a proteasome-independent intermediate during restriction of HIV-1 by rhesus TRIM5alpha. *J Cell Biol 180*, 13.

Cardone, G., Purdy, J.G., Cheng, N., Craven, R.C., and Steven, A.C. (2009). Visualization of a missing link in retrovirus capsid assembly. *Nature 457*, 694-698.

Davis, D., Yusa, K., Gillim, L.A., Newcomb, F.M., Mitsuya, H., and Yarchoan, R. (1999). Conserved cysteines of the Human Immunodeficiency Virus Type 1 protease are involved in regulation of polyprotein processing and viral maturation of immature virions. *Journal of Virology 73*, 9, 1156–1164.

Dismuke, D.J., and Aiken, C. (2006). Evidence for a functional link between uncoating of the human immunodeficiency virus type 1 core and nuclear import of the viral preintegration complex. *J Virol 80*, 3712-3720.

Egberink, H.F., Ederveen, J., Montelaro, R.C., Pedersen, N.C., Horzinek, M.C., and Koolen, M.J. (1990). Intracellular proteins of feline immunodeficiency virus and their antigenic relationship with equine infectious anaemia virus proteins. *J Gen Virol 71 (Pt 3)*, 739-743.

Forshey, B.M., von Schwedler, U., Sundquist, W.I., and Aiken, C. (2002). Formation of a human immunodeficiency virus type 1 core of optimal stability is crucial for viral replication. *J Virol 76*, 5667-5677.

Gamble, T.R., Yoo, S., Vajdos, F.F., von Schwedler, U.K., Worthylake, D.K., Wang, H., McCutcheon, J.P., Sundquist, W.I., and Hill, C.P. (1997). Structure of the carboxyl-terminal dimerization domain of the HIV-1 capsid protein. *Science 278*, 849-853.

Ganser, B.K., Cheng, A., Sundquist, W.I., and Yeager, M. (2003). Three-dimensional structure of the M-MuLV CA protein on a lipid monolayer: a general model for retroviral capsid assembly. *EMBO* J *22*, 2886-2892.

Ganser, B.K., Li, S., Klishko, V.Y., Finch, J.T., and Sundquist, W.I. (1999). Assembly and Analysis of Conical Models for the HIV-1 Core. *Science 283*, 80-83.

Ganser-Pornillos, B.K., Cheng, A., and Yeager, M. (2007). Structure of full-length HIV-1 CA: a model for the mature capsid lattice. *Cell 131*, 70-79.

Gitti, R.K., Lee, B.M., Walker, J., Summers, M.F., Yoo, S., and Sundquist, W.I. (1996). Structure of the amino-terminal core domain of the HIV-1 capsid protein. *Science 273*, 231-235.

Goudsmit, J., Houwers, D.J., Smit, L., and Nauta, I.M. (1986). LAV/HTLV-III gag gene product p24 shares antigenic determinants with equine infectious anemia virus but not with visna virus or caprine arthritis encephalitis virus. Intervirology *26*, 169-173.

Hübner, W., Chen, P., Del Portillo, A., Liu, Y., Gordon, R.E., and Chen, B.K. (2007). Sequence of human immunodeficiency virus type 1 (HIV-1) Gag localization and oligomerization monitored with live confocal imaging of a replication-competent, fluorescently tagged HIV-1. *J Virol 81*, 12596-12607.

Jin, Z., Jin, L., Peterson, D.L., and Lawson, C.L. (1999). Model for lentivirus capsid core assembly based on crystal dimers of EIAV p26. *J Mol Biol 286*, 83-93.

Kelly, B.N., Howard, B.R., Wang, H., Robinson, H., Sundquist, W.I., and Hill, C.P. (2006). Implications for viral capsid assembly from crystal structures of HIV-1 Gag(1-278) and CA(N)(133-278). *Biochem 45*, 11257-11266.

Langelier, C.R., Sandrin, V., Eckert, D.M., Christensen, D.E., Chandrasekaran, V., Alam, S.L., Aiken, C., Olsen, J.C., Kar, A.K., Sodroski, J.G.*, et al.* (2008). Biochemical characterization of a recombinant TRIM5alpha protein that restricts human immunodeficiency virus type 1 replication. *J Virol 82*, 11682-11694.

Laurents, D.V., Bruix, M., Jiménez, M.A., Santoro, J., Boix, E., Moussaoui, M., Nogués, M.V., and Rico, M. (2009). The (1)H, (13)C, (15)N resonance assignment, solution structure, and residue level stability of eosinophil cationic protein/RNase 3 determined by NMR spectroscopy. *Biopolymers 91*, 1018-1028.

Levandovsky, A., and Zandi, R. (2009). Nonequilibirum assembly, retroviruses, and conical structures. *Phys Rev Lett 102*, 198102-198101-198104.

Li, S., Hill, C.P., Sundquist, W.I., and Finch, J.T. (2000). Image reconstructions of helical assemblies of the HIV-1 CA protein. *Nature 407*, 409-413.

Mcdonald, D. (2002). Visualization of the intracellular behavior of HIV in living cells. *J Cell Biol 159*, 441-452.

Momany, C., Kovari, L.C., Prongay, A.J., Keller, W., Gitti, R.K., Lee, B.M., Gorbalenya, A.E., Tong, L., McClure, J., Ehrlich, L.S.*, et al.* (1996). Crystal structure of dimeric HIV-1 capsid protein. *Nat Struct Biol 3*, 763-770.

Owen, G. (2008). Cryo Electron Tomography -3D imaging at nm resolution. *Euro Cells and Mat 16*, 1.

Pettit, S., Sheng, N., Tritch, R., Erickson-Viitanen, S., and Swanstrom, R. (1998). The regulation of sequential processing of HIV-1 gag by the viral protease. *Advances Exp Med and Biol 436*, 15-25.

Pilhofer, M., Ladinsky, M.S., McDowall, A.W., Jensen, G.J. (2010). Bacterial TEM: New insights from cryo-microscopy. *Methods Cell Biol* 96, 21-45.

Pornillos, O., Ganser-Pornillos, B.K., and Yeager, M. (2011). Atomic-level modelling of the HIV capsid. *Nature 469*, 424-427.

Shah, V.B., and Aiken, C. (2011). In vitro uncoating of HIV-1 cores. *J Vis Exp*. 57 e3384, DOI: 10.3791/3384

Sundquist, W.I., and Hill, C.P. (2007). How to assemble a capsid. *Cell 131*, 17-19.

Swanstrom, R., and Wills, J.W. (1997). Synthesis, assembly, and processing of viral proteins. *Retroviruses*, S.H.H. J.M. Coffin, and H.E. Varmus, ed. (Cold Spring Harbor, New York, Cold Spring Harbor Laboratory Press), pp. 263-334.

Tanaka, N., Nakanishi, M., Kusakabe, Y., Goto, Y., Kitade, Y., and Nakamura, K.T. (2004). Structural basis for recognition of 2',5'-linked oligoadenylates by human ribonuclease L. *EMBO* J *23*, 3929-3938.

Tanchou, V., Gabus, C., Rogemond, V., and Darlix, J.L. (1995). Formation of stable and functional HIV-1 nucleoprotein complexes in vitro. *J Mol Biol 252*, 563-571.

Vogt, V.M. (1997). Retroviral virions genomes. *Retroviruses* (Cold Spring Harbor, New York: Cold Spring Harbor Laboratory Press), pp. 27-69.

von Schwedler, U.K., Stray, K.M., Garrus, J.E., and Sundquist, W.I. (2003). Functional surfaces of the human immunodeficiency virus type 1 capsid protein. *Journal of Virology 77*, 5439-5450.

Wright, E., Schooler, J., Ding, H., Kieffer, C., Fillmore, C., Sundquist, W.I., and Jensen, G. (2007). Electron cryotomography of immature HIV-1 virions reveals the structure of the CA and SP1 Gag shells. *EMBO* J *26*, 2218-2226.

Zhang, H., Dornadula, G., and Pomerantz, R.J. (1996). Endogenous reverse transcription of human immunodeficiency virus type 1 in physiological microenviroments: an important stage for viral infection of nondividing cells. *J Virol 70*, 2809-2824.

CHAPTER 3:

CONTRIBUTIONS TO METHODS

3.1

INTRODUCTION

Since the field of electron cryotomography is still relatively new, there are many protocols that have not been standardized. Each laboratory or individual researcher has a method for the techniques used, but this makes experiments very difficult to repeat across the field. In order to establish a more standardized set of protocols, I have described here three methods that I contributed to developing.

In the first, I tested procedures used to purify HIV particles from the medium of infected cells (Chapter 3.2). Researchers typically use a sucrose cushion for purification, but it was recently suggested that this method caused more damage to the structural integrity of the particles than a commercial preparation called Optiprep (Kol et al., 2010). Using electron cryotomography, I compared particles from the two different preparation methods, as well as with or without the envelope protein. It was found that purifying with a sucrose cushion did not affect the structural integrity of the particles, and neither did the presence or absence of the envelope. These results were submitted to other laboratories that frequently purify HIV particles, impacting the way many researchers conduct their experiments using purified particles, as well as their confidence level in the structural integrity.

The second method described is plunge freezing for electron cryomicroscopy (Chapter 3.3). Since the 1980s, plunge freezing has been used as a technique to rapidly freeze thin samples for preservation in vitreous ice. Researchers preparing cryosamples typically establish their own set of protocols that work for their sample, and then train new researchers based on their established methods. However, several steps in the process are sample-specific, and so repeating a published experiment based on one's

own methods would fail to repeat the results. Therefore, we published a chapter in *Methods in Enzymology* describing a set of conditions to consider when plunge freezing (Dobro et al., 2010). This will hopefully impact the reproducibility of electron cryomicroscopy experiments and give researchers a broad perspective so they understand the history, know what options to consider when plunge freezing, adhere to safety recommendations, and know what equipment is available.

In the third method, I describe what was learned about growing thin eukaryotic cells on electron microscopy grids for plunge freezing and electron tomography. The goal of the project was to image cells infected with HIV to observe the host/virus interaction at the early and late stages that take place near the plasma membrane. The project was not completed, but many steps along the way helped advance our ability to image cells. These lessons are described to advance future projects involving electron microscopy of eukaryotic cells.

3.2

EFFECTS OF PURIFICATION ON HIV STRUCTURE

Introduction

HIV exits infected cells as a non-infectious, immature particle. The Gag protein helps to deform the membrane during budding and gives HIV its structure as an independent particle. In the immature state, Gag forms a spherical shell just under the membrane and surrounds the virion's genome and enzymes. During maturation, the Gag protein is cleaved in several domains and refolds to form the conical capsid indicative of the infectious particle.

Gag of the immature virus forms a hexagonal lattice that is now known to contain large gaps. Using electron cryotomography, Gag in immature particles has been found to cover about 40% of the particle and consist of several patches in one study (Wright et al., 2007), or cover 70% and consist of a continuous lattice in other studies (Carlson et al., 2008; Briggs et al., 2009).

In 2010, a publication studied the completeness of the Gag shell using two different purification methods (Kol et al., 2010). It was concluded that the Gag shells were significantly less complete when purified with sucrose cushions (60%) compared to Optiprep, a non-ionic density gradient media also known as Iodixanol (82%). This affected the rigidity of the particles as well, with the sucrose-purified particles being much softer than the Optiprep-purified particles.

In light of these results, I repeated the experiment since the paper that claimed the immature particles were only 40% complete came from our lab and were purified

using sucrose cushions (Wright, 2007). This was an important study that has influence on the way HIV labs purify virions.

In addition to studying the effects of purification on Gag completeness, we were also curious about whether the presence of an envelope affects Gag completeness. This is because it was reported that the stiffness of immature particles is dramatically decreased when the envelope was deleted, specifically the cytoplasmic tail of Env (cyt) (Kol et al., 2007). We purified immature HIV particles with Env using the traditional sucrose cushion, and particles with and without Env using the new Optiprep method.

Materials and Methods

Viral Preparation and Purification

Virginie Sandrin at the University of Utah prepared immature viral particles by transfecting 293T cells with the pNL–MA/p6+Env and pNL–MA/p6–Env vectors to produce immature particles with and without envelope. Viral supernatant was collected after 18 hours and sent to Caltech. I purified the particles using the sucrose cushion method or Optiprep. The sucrose cushion consisted of 5 ml of 20% sucrose in TNE buffer (0.15 M NaCl, 1mM EDTA, 10 mM Tris, pH 7.6). Viral particles were pelleted through the cushion in an SW-28 rotor at 25,000 RPM for 1 hour. The virus pellet was collected for plunge freezing. The Optiprep method consisted of a 5 ml cushion that the viral particles pelleted on top of in an SW-28 rotor at 21,000 RPM for 90 mins. The supernatant was aspirated, leaving 2–3 ml of media above the cushion. The cushion was removed with a syringe, and the remaining supernatant containing the viral particles was resuspended in TNE buffer and concentrated by ultrafiltration with a MWCO filter column of 100,000

spun at 3,000 × g. The concentrated particles were washed in TNE buffer and filtered again two more times.

Electron Microscopy

Viral particles were plunge frozen on R1.2/1.3 Quantifoil grids with a blot time of 1–3 seconds and offset of 0 or -1 mm. Two-dimensional projection images were collected on the FEI Tecnai T12 or Polara microscope. For each particle, I collected images at different defocus values to increase the ability to determine the completeness of the Gag shell.

Results

I imaged 48 Env+ particles purified with Optiprep, 80 Env− particles purified with Optiprep, and 41 Env+ particles purified through a sucrose cushion. These particles had a clearly visible shell, whereas others were imaged that I could not measure the Gag shell for various reasons (obstructions, poor contrast, etc.) and were not counted. For each particle, I assigned a value of having a 100% full Gag shell, 75% full, 50% full, or 25% full. Counting the number of particles for each category of completeness, I calculated the average percent coverage for each purification method.

When comparing the groups, there is not a significant difference in Gag completeness whether the particles have Env or not when purified with Optiprep (67.7% versus 66.9%). However, the Gag shells were more complete when purified with sucrose (87.2% versus 66.9% and 67.7%). There was, however, variability in each sample and there were still many Optiprep particles that had complete Gag shells present. The values are summarized in Table 3.1 and representative images are included in Figures 3.1–3.3.

Table 3.1. Summary of Gag completeness for each sample

Optiprep + env	# particles	% total particles
full gag	15	31.3
3/4 gag	6	12.5
1/2 gag	25	52.1
1/4 gag	2	4.2
total	48	
avg % coverage	**67.7**	
Optiprep - env	# particles	% total particles
full gag	22	27.5
3/4 gag	13	16.3
1/2 gag	42	52.5
1/4 gag	3	3.8
total	80	
avg % coverage	**66.9**	
Sucrose + env	# particles	% total particles
full gag	25	61.0
3/4 gag	11	26.8
1/2 gag	5	12.2
1/4 gag	0	0.0
total	41	
avg % coverage	**87.2**	

Discussion

The result is surprising as it concludes the opposite of the published results (Kol et al., 2010) that sucrose cushions reduce the completeness of the Gag shell. There are many reasons viral particles could be more or less intact. The time of harvesting, the resuspension by pipetting, the temperature, and the plunge freezing blot methods are a few examples of protocol variations that could affect the Gag shell completeness. However, under the same conditions, it does not seem that the presence of Env or the Optiprep purification method preserved larger Gag shells.

One caveat of the experiment is that the imaging was two-dimensional, so a particle considered to have a complete Gag shell could have contained holes on the top or

bottom that were not detected. However, every sample was imaged in two dimensions and so the possibility for holes in the top and bottom of the particles was normalized across samples. Also, the previously published reports on Gag completeness were also done in two dimensions.

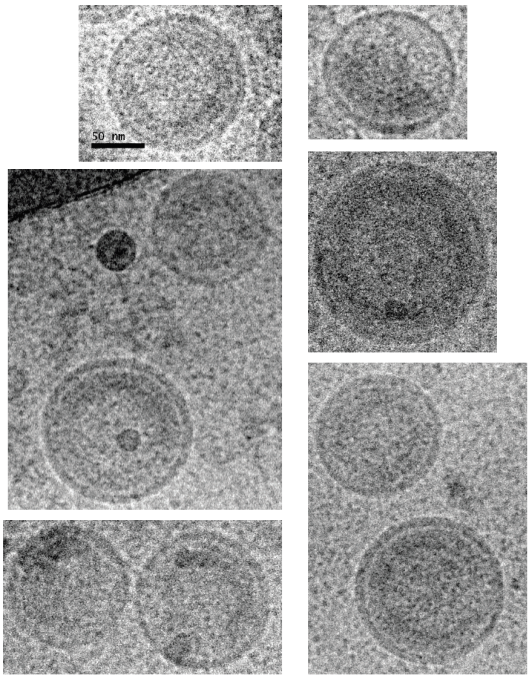

Figure 3.1: Optiprep Purification of +Env HIV particles

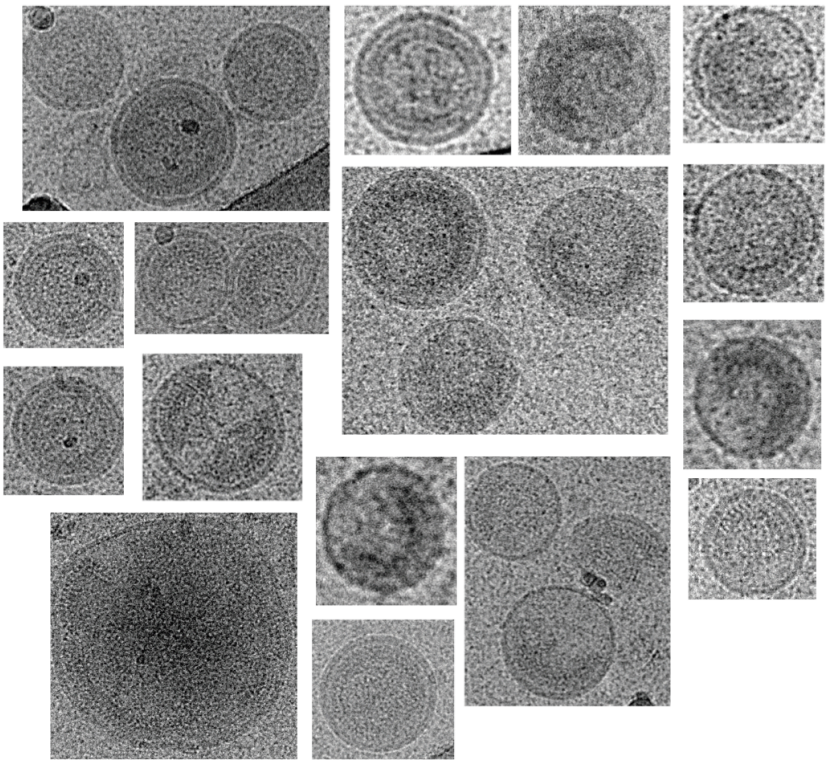

Figure 3.2: Optiprep Purification of –Env HIV particles

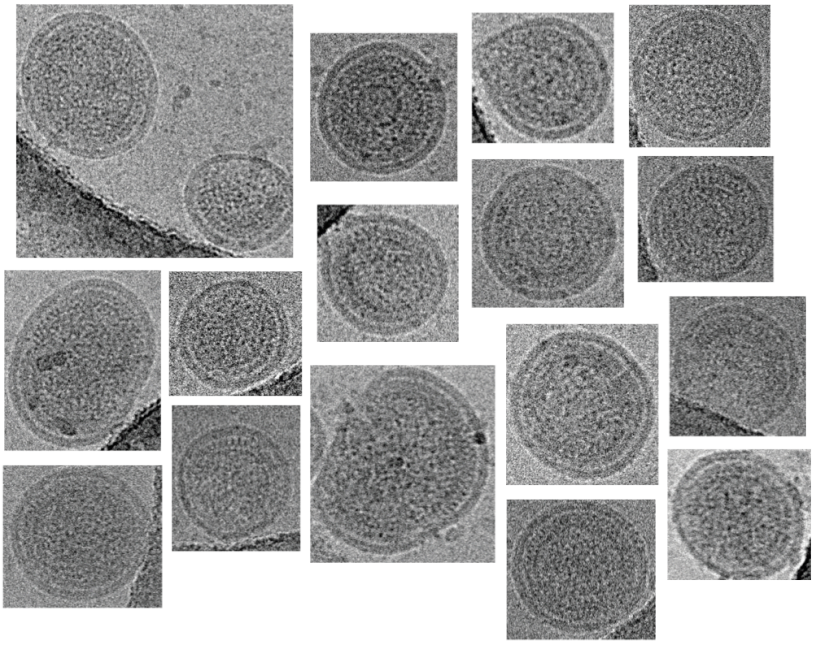

Figure 3.3: Sucrose Purification of +Env HIV particles

3·3

PLUNGE FREEZING FOR ELECTRON CRYOMICROSCOPY

Megan J. Dobro[1], Linda A. Melanson[2], Grant J. Jensen[1,3], and Alasdair W. McDowall[1*]

[1]Division of Biology and Howard Hughes Medical Institute, California Institute of Technology, 1200 E California Blvd, Pasadena, CA 91125, USA

[2]Gatan, Inc., Pleasanton, California, USA

[3]Howard Hughes Medical Institute, California Institute of Technology, Pasadena, CA, USA

*Correspondence should be addressed to AWD: mcdowall@caltech.edu, 626-395-8829

Abstract

Aqueous biological samples must be "preserved" (stabilized) before they can be placed in the high vacuum of an electron microscope. Among the various approaches that have been developed, plunge freezing maintains the sample in the most native state and is therefore the method of choice when possible. Plunge freezing for standard electron cryomicroscopy applications proceeds by spreading the sample into a thin film across an EM grid and then rapidly submerging it in a cryogen (usually liquid ethane), but success depends critically on the properties of the grid and sample, the production of a uniformly thin film, the temperature and nature of the cryogen, and the plunging conditions. This chapter reviews plunge-freezing principles, techniques, instrumentation, common problems, and safety considerations.

Introduction

Because electrons have such high scattering cross-sections, their path through the electron microscope must be kept at extremely high vacuum. Aqueous biological samples must therefore be stabilized or "preserved" before they can be imaged. The first set of methods that were developed to preserve biological samples for EM involved dehydration: protein and viruses were negatively stained; tissues and cells were first chemically fixed, then dehydrated, plastic embedded, sectioned, and then stained. Dehydration perturbs structure, however, so methods were sought to preserve samples in their naturally hydrated state through freezing. The basic problem is, of course, that when frozen gradually, water crystallizes and expands, again denaturing macromolecules and perturbing cellular structures. One approach to solving this problem is to apply high pressures and cryoprotectants ("high pressure freezing"), which inhibit the nucleation and growth of ice crystals.

It was wondered, however, whether water or biological molecules could instead be cooled so rapidly that molecular rearrangements would simply stop before ice crystals had time to form. In the early 1970s, Taylor and Glaeser plunged hydrated catalase crystals into liquid nitrogen and showed that the crystals still diffracted to 3.4 A (proving that the structure of the proteins had been preserved to at least that resolution; Taylor and Glaeser, 1973, 1974). Then in 1981, the Dubochet group showed that pure water could be frozen in a noncrystalline, liquid-like ("vitreous") state by spreading it into a thin layer across a standard carbon-coated EM grid and plunging it into liquid ethane (Dubochet and McDowall, 1981). At first, this claim was met with skepticism, but the impact the advance would have on structural biology became clear when macromolecular complexes were later added to the water and shown to be preserved in a native, "frozen-hydrated" state (Adrian et al., 1984). The development of dedicated cryo-EM instrumentation (anticontaminators; low-dose kits, and tools to insert and hold frozen grids) and complementary advances in software, computational power, and other aspects of the work have now fully capitalized on this advance, producing reconstructions of specimens in their native states that are interpretable at the atomic level.

Today, plunge freezing is being used to study macromolecules, drug delivery vehicles, 2D protein crystals, cell fractionations, vesicle suspensions, filaments, virus particles, thin bacteria, polymers, matrices, colloids, nanoparticulate catalysts, and even emulsion paints (Cerritelli et al., 2009; Finnigan et al., 2006). A variety of plunge freezers and protocols have been optimized for different applications (Grassucci et al., 2007; Iancu et al., 2006). The process of preparing samples for electron cryomicroscopy can be arduous, however, and often requires extensive troubleshooting to determine the best freezing conditions for each sample. This chapter describes the plunge-freezing protocol in detail and will enable the novice to recognize the potential rewards and

challenges that await them.

Grids and Supports

The first step in preparing samples for electron cryomicroscopy is to choose the right grid and support film. The grid itself can be made from a variety of metals. Copper is the most common, but if cells are to be grown on or in the presence of the grid, gold is a better choice because it is less toxic. Molybdenum has the advantage that it has a similar coefficient of thermal contraction as carbon, so that when frozen, the grid and the carbon support shrink more similarly, preventing "crinkling" (Booy and Pawley, 1993). Larger mesh sizes (smaller squares between grid bars) provide more support, but the grid bars block more area on the grid, especially at high tilt angles. Specialized "finder" grids are decorated with symbols to help mark particular locations on the grid, which can be critical, for instance, in correlative light and electron microscopy.

Grids for cryo-EM applications are almost invariably coated with a thin carbon film, although just recently, a new silicon ceramic combination called CryomeshTM has been introduced, which shows promise in providing greater strength and stability (Quispe et al., 2007; Yoshioka et al., 2010). The carbon film can be either "continuous" (no holes) or "holey." Continuous-carbon support films can be better for 2D crystals, for instance, where maintaining a perfectly flat crystal is more important than reducing background noise. Holey carbon films allow background noise to be reduced, as samples can be imaged suspended in vitreous ice alone across the holes. While "lacey" grids (prepared either in the lab or purchased) have an irregular array of varying hole sizes (Figure 3.4A), commercially available Quantifoil and C-flat films have a regular pattern of holes (Figure 3.4B) to facilitate automatic image acquisition. Typical hole sizes are around 1 mm. Larger holes maximize the sample imaging area, but it is helpful to have at least some carbon film (and maybe the full periphery surrounding a hole) in each image to reveal

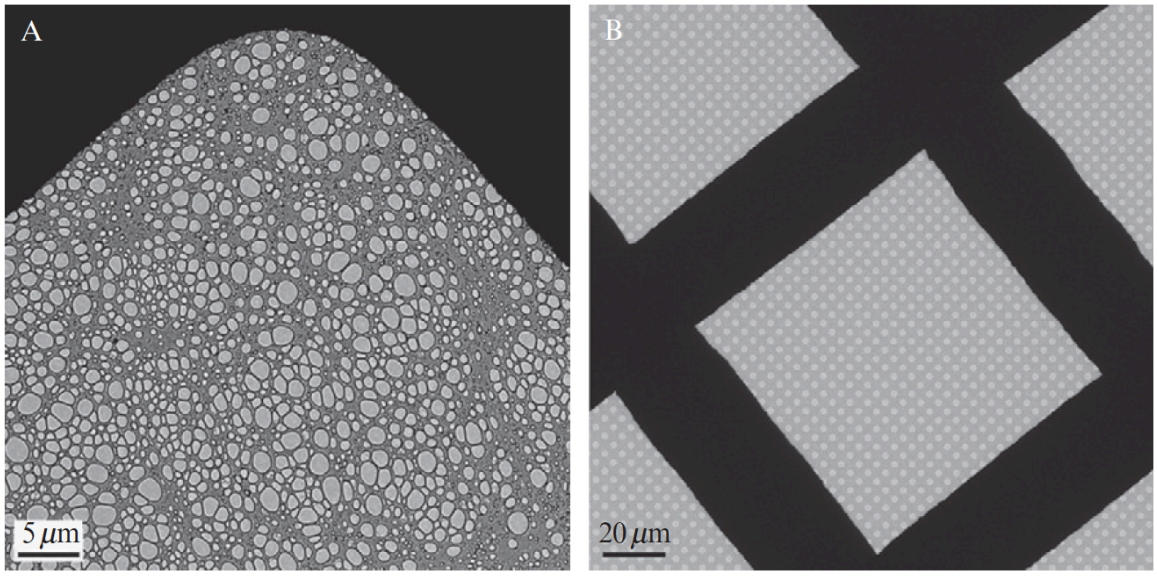

Figure 3.4. EM grid types. (A) Lacey carbon support film with an array of various hole sizes (grid bar 5 μm) and (B) Quantifoil grid showing regular pattern of holes in carbon (grid bar 20 μm).

the defocus more precisely and to reduce charging.

Unfortunately, in our experience, the surface properties and integrity of the support film vary from batch to batch. We therefore recommend that a few grids from each batch be tested before use. The integrity of the carbon film can be checked easily in a light microscope, both before and after plasma cleaning. The surface properties can be checked by plunge-freezing pure water on a grid with standard plasma-cleaning and plunge-freezing protocols to make sure that uniformly thin vitreous ice is formed. Commercial suppliers can customize their support films to particular needs to reduce substrate bubbling, for instance, or improve film stability through the use of extra thick layers.

Cleaning the Grids

Freshly prepared carbon films are hydrophilic, but they become progressively more

hydrophobic over time. It is therefore usually necessary to restore their hydrophilicity so that the liquid sample will spread evenly over their surface. Before the advent of electron cryomicroscopy, plasma cleaning, also called "glow discharging," was used to modify the adhesive properties of a variety of substrates for room temperature microscopy (Dubochet et al., 1971). The plasma is created from the ionization of a gas, such as air, argon, oxygen, and hydrogen, or combinations thereof, such as argon/oxygen or hydrogen/oxygen, under low vacuum. Radicals within the plasma react with the surface of the substrate. As a result, the surface of the grid typically becomes hydrophilic. When liquid samples are then placed on the grid, they spread evenly across the surface and can be blotted to form films as thin as just tens of nanometers thick (Gan et al., 2008). On a properly cleaned grid, in the chamber of a humidity-controlled plunge freezer, this thin sample film is remarkably stable and can remain suspended across holes in the grid for many seconds. If the plasma cleaning does not make the whole surface of the film uniform, the liquid will not spread over the grid or blot evenly off the grid, causing denser ice in some areas. One result can be, for instance, a bulge of ice in the center of each grid square (Figure 3.5C).

Plasma-cleaning parameters, such as the chamber pressure, radio frequency (RF) power, the gas mixture used to form the plasma, and the overall system geometry, should all be explored and optimized. The system settings can vary for each machine and application, but in our lab at Caltech, we use a platform height of 35 mm, a glow time of 60 s and an electrical current of 15 mA. If the fields are too strong or the glow time is too long, bombardment by the highly energetic ions can break the carbon film. The carbon film can also break if the vacuum is vented too quickly. Small organic molecules like amylamine and polylysine can be introduced as vapors during the ion discharge and subsequently affect how purified macromolecules partition in the ice over the carbon film and the holes. Once cleaned, grids can be stored in their original storage grid box

and sealed in an air-tight bag or chamber for later use. There are several diagrams available that show the proper setup for a plasma-cleaning system (Aebi and Pollard, 1987; Kumar et al., 2007).

Building homemade plasma cleaners can be dangerous because of the high currents and voltages used and the specialized gases required to create the plasma. Commercial instruments are widely available. Some are designed solely for plasma cleaning and others also offer carbon coating. The Cressington 208 plasma-cleaning module attached to the Cressington carbon coater has a fixed 40 mm grid platform height and programmable time and power values. The Emitech K100X free standing unit uses a programmable protocol sequence, an adjustable height platform, and options for introducing alternate gases, making this a versatile unit. The smaller Harrick PDC-32 unit has fewer control settings, a fixed glow tube diameter, and may be easily transported to more remote research locations. Further development by Gatan, Inc. has produced the autotuning SolarusTM 950 Advanced Plasma Cleaning System, with a chamber to accommodate grid cleaning as well as two ports for cleaning microscope specimen holders. The SolarusTM 950 is configured to use a hydrogen/oxygen gas mixture that cleans with minimal sputter damage, making it especially suitable for cleaning fragile carbon support substrates. Because of the efficiency of the hydrogen/oxygen plasma, the cleaning time for carbon substrates is very short, typically 15–30 s using a hydrogen/oxygen gas mixture and a RF setting of 50 W. This has produced carbon films that are uniformly hydrophilic and can remain so for several weeks (Melanson, 2009b).

Though plasma cleaning is the preferred method to clean grids, when plasma cleaners are not available, the grids can also be dipped into ethanol, acetone, or chloroform or be recoated with a fresh carbon layer (Quispe et al., 2007). Grids can also be coated with polylysine or other organic molecules to promote the adherence of cells,

for instance. We and others have found that more extreme grid treatments (such as overnight "preirradiation" in an EM) can cause certain macromolecular complexes to partition into the holes in the carbon.

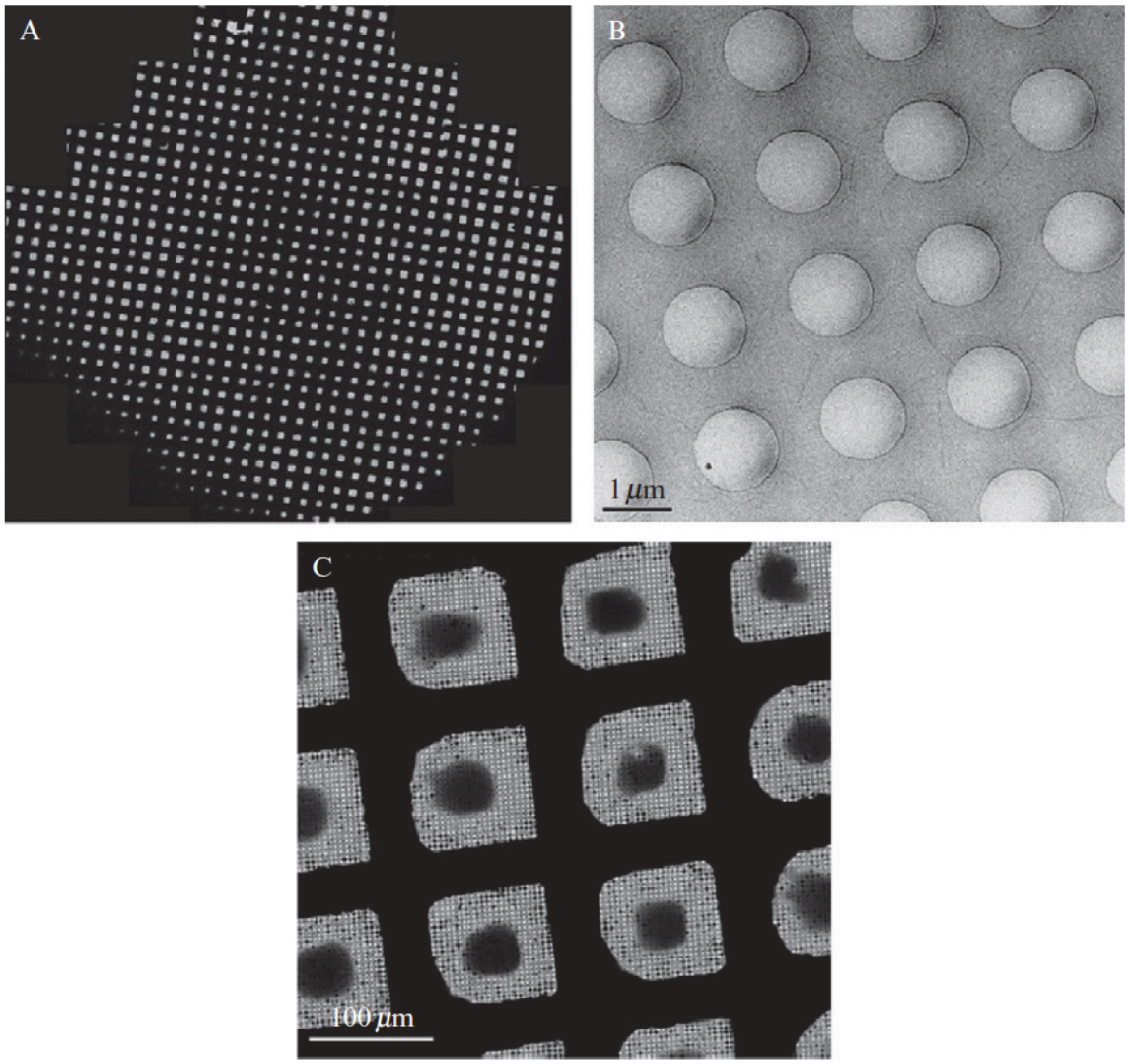

Figure 3.5. The effect of plasma cleaning on the ice. (A) Montaged serial EM atlas of a grid showing uniform ice thickness, image courtesy of Guenter Resch. (B) A SolarusTM plasma-cleaned Quantifoil film with thin, uniform ice in the holes, image courtesy of Chen Xu, Rosentiel Basic Medical Sciences Research Center, Waltham, MA (grid bar 1 mm). (C) When plasma cleaning fails, one result can be a dense cores of ice in the center of each grid square (grid bar 100nm).

Preparing the Cryogen

For water to vitrify, the temperature has to drop faster than ~10^5 K/s (Dubochet and McDowall, 1981). The reason why samples have to be thin is that the heat conductivity of the water in the sample is the limiting factor. The cryogen that the sample is plunged into has to have a high thermal conductivity in order to transfer heat out of the specimen quickly, a freezing point below the temperature needed to vitrify the sample, and both a high boiling point and a large heat capacity to prevent a layer of vapor forming between the sample and the cryogen (Bellare et al., 1999). While the temperature of liquid nitrogen at ambient pressures is very low (77 K), it is readily available, and it is relatively inexpensive, unfortunately its thermal conductivity is only about 400 K/s and so frequently produces crystalline ice. The most commonly used cryogens are therefore ethane and propane, primarily because their thermal conductivity is 300–400 times higher (in excess of 13–15 kK/s). The freezing point of ethane is 90 K, its boiling point is 184 K, and it has a high heat capacity (68.5 J/mol K at 94 K). Liquid nitrogen is used instead as the primary coolant to first liquefy the ethane or propane and then keep it cold during the procedure.

An inconvenience arises, however, because the freezing points of both ethane and propane are higher than the temperature of the nitrogen, so they slowly solidify during the experiment. Some plunge freezers have therefore been constructed with built-in heating elements or special designs that limit the heat transfer between the nitrogen and ethane/propane cups to maintain the cryogen just above its melting point. Tivol et al. (2008) found that a mixture of 37% ethane and 63% propane remains liquid even when in direct contact with liquid nitrogen. This mixture produces consistently thin vitrified layers and facilitates long plunge-freezing sessions without heaters or special cup configurations.

After the grid is plunged into the cryogen and then transferred into liquid nitrogen for storage, excess ethane (or propane) on the grid will freeze, forming a solid crust. Usually, this crust falls off the grid in subsequent handling, but if not, it will sublime rapidly when the grid is inserted into the high vacuum of the microscope. Impurities will remain, however, so it is important to use very pure cryogen. Lower grade "camping gas propane" is too full of contaminants to produce clean samples.

Condensing the Cryogen

Cryogens come as compressed gases and therefore need to be liquefied. This is done by releasing the gas slowly into a cup cooled by liquid nitrogen. The flow of the gas can be controlled with a 2-stage regulator fitted with a needle valve on the second stage and narrow-bore Tygon tubing on the nozzle. A pipette tip is usually inserted into the end of the Tygon tubing to further restrict and better direct the gas flow. The following is a typical protocol for condensing the cryogen:

1. Work in a fume hood and wear a lab coat and goggles.

2. Pour liquid nitrogen into the space around the cryogen cup. When the cup has reached at least −175°C, the liquid nitrogen will stop bubbling violently (the "Leidenfrost point"). Depending on the plunge freezer design, this can take 5–15 min, and the procedure is usually outlined in the instruction manual specific to the instrument being used.

3. Before starting the condensation process, check to make sure that the cryogen cup is free of any residual liquid nitrogen.

4. With the needle and main tank valves on the 2-stage regulator closed at this point, adjust the gas outlet pressure on the second stage to approximately 0.14–0.28 bar. Use

low pressure to avoid unnecessary venting of the gas into the fume hood or splashing of condensed cryogen.

5. Place the tubing attached to the gas tank regulator into the bottom of the precooled cryogen cup (as in Figure 3.6A).

6. Open the main tank and needle valves to allow delivery of the gas at the preset pressure.

7. You will start to notice the liquid filling the cup. When the liquid reaches the top, decrease the flow of gas and slowly pull the tip of the tubing out. Quickly turn the gas off. If you turn the gas off while the tip is still submerged, the liquid will aspirate back into the tubing.

8. Remember to close the main tank valve on the cylinder and bleed the line of any residual gas. Always leave the gas cylinder in a safe configuration as defined by the safety procedures for your laboratory.

Alternatively, the cryogen can be condensed in a separate container cooled by liquid nitrogen and then poured into the precooled cryogen cup (Figure 3.6B).

Safety Considerations

Before handling cryogens, read about them thoroughly in the latest Materials Safety Data Sheets. Ethane and propane are highly flammable and are even more so when condensed, so do not condense these gases in the presence of an open flame. Only condense the smallest volume necessary to fill the cryogen cup (usually less than 10 ml). Rather than having one large tank of cryogen gas, try to limit the size and keep reserve tanks in flameproof cabinets. Two refillable cylinders containing 67 lb of gas last 2–3 months in a busy laboratory. Ethane or propane gas cylinders, and their associated 2-

stage regulators, should be ordered and installed in consultation with the on-site laboratory safety officer.

The liquid nitrogen that is used to maintain the low temperature of the condensed cryogen will evaporate over time and must be continually refilled during a freezing session. Replenishing the liquid nitrogen also serves to maintain a layer of cold, dry nitrogen gas surrounding the condensed cryogen. This helps to minimize condensation of atmospheric moisture into ice that will contaminate the cryogen and the sample and provide a protective interface for transferring the frozen specimen grid. However, try not to splash liquid nitrogen into the cryogen. The surface of the cryogen can freeze solid, entrapping an underlying volume of warmer, liquid cryogen that can explode through the frozen layer. The CryoplungeTM 3 has a shield over the workstation to prevent splashing as well as an external funnel for refilling the liquid nitrogen (Figure 3.6C). Physical exposure to these low temperature cryogens can produce severe frostbite. Always wear adequate eye and face protection when working with these cryogens. Also, exercise caution when handling any materials that come in contact with the condensed cryogen, since these surfaces can also freeze skin and underlying tissues.

While small volumes of liquid nitrogen can safely be poured over a large ventilated surface, such as a floor, to dispose of it, it is recommended that propane and ethane be allowed to evaporate in a dedicated fume hood for several reasons. First, they are highly flammable. As the cryogens evaporate, they will expand rapidly by factors in excess of 700 times. Since the cryogens are odorless and colorless, there is also a risk of asphyxiation as atmospheric oxygen is displaced. Even at low concentrations, ethane gas can cause narcotic effects with symptoms of dizziness, headache, nausea, and loss of coordination. The plunge-freezing area should be well ventilated, and labs handling large volumes of cryogens can be equipped with oxygen displacement sensors to warn people

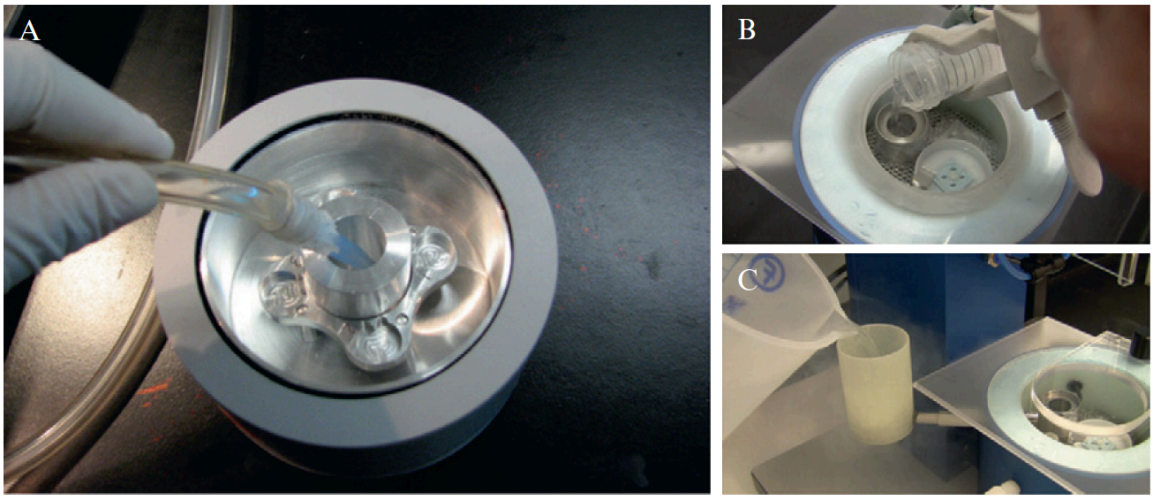

Figure 3.6. (A) Condensing the cryogen by flowing cryogen gas into a precooled cup surrounded by liquid nitrogen. (B) Pouring liquid ethane into the cold cryogen cup after condensing ethane gas in a separate container. (C) Refilling the liquid nitrogen through an external port maintains a clean, cold nitrogen gas environment. (B)–(C) Images courtesy of Gatan, Inc., Pleasanton. CA.

when oxygen gets low. In addition to educating the staff on the risks from cryogens, always provide plenty of protective cryo gloves and eye shields and post signs alerting visitors and emergency responders to the location of cryogens.

Plunging the Grid

Basic Procedure

The process of plunge freezing generally involves three main steps: a small liquid droplet containing the specimen is applied to the carbon surface of an EM grid; the liquid droplet is blotted with filter paper until only a very thin film of fluid remains; and then the grid is plunged into the cryogen. The grid is then stored in liquid nitrogen in a custom-made grid box until it is finally loaded into the electron cryomicroscope for imaging. Blotting can be done from either one or two sides. Unilateral blotting can be particularly helpful in reducing the direct contact of fibers in the blotting paper with

cells, for instance, growing on the other side (Lepper et al., 2010). The best ice thickness depends on several factors, including the size and shape of the specimen and the accelerating voltage of the electron cryomicroscope that will be used. Thicker ice may provide more stability, but if the fluid sample to be vitrified is too thick, the ice may not vitrify. If too much fluid is blotted away, the cells can become dehydrated. The thinness of the ice will also effect how particles distribute across the holes: large particles may be displaced to deeper regions of the film, such as the edge of a hole. Particles may also be oriented preferentially in very thin layers in part because of surface charges at the air/liquid interface (Glaeser et al., 2007). The temperature, humidity, blotting pressure, and blotting duration should be optimized for each specimen. It has recently been shown that blotting can damage and even kill large cells (Lepper et al., 2010). Such samples should therefore be blotted gently for longer times.

As an example protocol for plunge-freezing protein or bacteria,

1. Suspend the sample in an aqueous medium (e.g., water or low ionic buffer solution to reduce background noise during imaging) at a concentration of 1–3 mg/ml for protein complexes or an OD600 of 0.5 for bacteria.

2. Plasma clean EM grids, following the instructions provided in the user manual for your particular machine.

3. Secure an EM grid with the tweezers provided with your plunge freezer and attach the tweezers to the machine.

4. If the plunge freezer has a humidity-controlled chamber, set the humidity to 100%.

5. Apply 3–5 ml of the sample to the carbon side of the grid (see the manufacturer's instructions on the grid box).

6. Blot the EM grid with #1 grade filter paper for 1–3 s to produce an aqueous film less than 1 mm in thickness.

7. Plunge into liquid cryogen to produce a thin glass-like solid.

8. Transfer the grid into a labeled four-grid-slot box in liquid nitrogen, being careful not to expose the grid to atmospheric moisture.

9. Grid boxes are stored within a 50 ml conical tube placed in a large nitrogen cryostorage dewar.

Part of the skill of plunge freezing is knowing when the cryogen is at the right temperature. When gaseous cryogens are first liquefied, they are still warmer than the surrounding liquid nitrogen, and it takes time for them to cool further. The best indication for when the liquid ethane reaches the right temperature for plunge freezing is when the bottom of the cup freezes, but enough liquid remains at the surface for plunging the grid. This state does not last very long before the rest of the volume freezes, however, so unless a mixture of ethane and propane is used or the freezing device somehow keeps the cryogen temperature just above its freezing point (see earlier), the cryogen will have to be melted periodically. This can be done by inserting a warm metal rod or adding more (room temperature) cryogen gas, but neither strategy is ideal, since rods can introduce contamination and adding more gas can cause the cryogen to overflow the cup. One must also wait again until the cryogen has recooled to its freezing point before the next grid is frozen.

After a grid has been plunged, it should be handled very carefully to avoid damage. The grid should never be bent, because it will then fail to seat securely in the holder, causing drift and instability, so try to avoid touching the grid to any walls of the freezing cup during manipulation. When transferring the frozen grid from the cryogen cup to the

storage holder, the grid may need to be lifted out of the cryogen very quickly in a space filled with cold dry nitrogen gas to prevent exposing it to moisture in the air. Floating cylindrical barriers and purpose-built covers are also to be used to trap more dry nitrogen gas and protect the specimen. For more details on the plunge-freezing procedure, see Iancu et al., 2006. Training courses are frequently available from vendors and the NIH-funded National Research Resource Centers.

Controlling Humidity

Atmospheric moisture in the cryolab is undesirable. If precautions are not taken, moisture will form ice crystals on liquid nitrogen storage containers and subsequently on the grid sample. In humid regions of the world, cryolabs employ complex ventilation systems and dehumidifiers for reducing relative humidity to less than 25%. Additionally, instruments may be entirely enclosed within a humidity-controlled chamber. (A cautionary tip: low humidity may increase static electricity. Certain floor coverings and clothes can reduce these discharges.) The regulations at some institutions require that plunge freezers be operated in a fume hood. The strong air currents within fume hoods can introduce ice contamination and air-drying artifacts. A shield around the plunging area is recommended. Automated plunge freezers now provide covers that facilitate a dry nitrogen gas flow over the cryogen container to reduce contamination. In addition, all liquid nitrogen dewars must be kept dry between freezing sessions and fitted with a loose lid to reduce water vapor condensation. Always invert portable tanks and dewars to dry, since moisture will collect on their cold surfaces. A large drying incubator at 30 °C is useful to ensure that all components remain moisture free. Workstations with heat blocks set at 50 °C can be used to dry small tools, and a source of low pressure “lab air” can be used to dry fixtures.

While atmospheric moisture must be controlled to avoid contamination, a higher

relative humidity in the immediate area of the sample grid is preferred for preventing desiccation of the sample prior to freezing. Many commercial plunge-freezing instruments offer an environmental chamber for controlling temperature and humidity. This controlled environment is especially important when blotting, as evaporation and surface air/liquid interfaces play important roles in electrostatic forces and on how macromolecules organize at the surface. In general, the humidity in the chamber before plunging should be greater than 80%, as demonstrated in the preservation of liposomes. Humidity values in the 40% range will create osmotic imbalances as water evaporates from the film, causing liposome inversions (Frederik and Hubert, 2005). Other effects are seen in the preferential organization of viral capsid complexes as they align because of surface interactions (Dubochet et al., 1985).

Instrumentation

The designs of plunge freezers used in pioneering experiments contributed to the design of modern-day instruments (Fernandez-Moran, 1960; Handley et al., 1981; McDowall et al., 1984). Early laboratory prototypes for plunge freezers were often a basic construction of makeshift stands and Styrofoam boxes (Dubochet et al., 1983; McDowall et al., 1983; McDowall, 1984). One of the first plunge freezers was a simple pivoting fine-forcep holding a carbon-coated grid. The grid fell in a gravity arc past a vaporized mist sprayed through an aperture slit. The continuous-carbon substrate collected microfine droplets, which were vitrified in a pot of viscous ethane. The first image of vitreous water was prepared in this way (Dubochet and McDowall, 1981). Eventually, the carbon substrate was removed and the "bare grid" method was the precursor of the unsupported liquid film (Adrian et al., 1984). The Dubochet group's 1980s plunge freezer design was an elastic-driven rod supporting gold electronic circuitry pins for freezing suspensions and filaments. A water-driven magnetic stir bar kept the ethane fluid and successfully

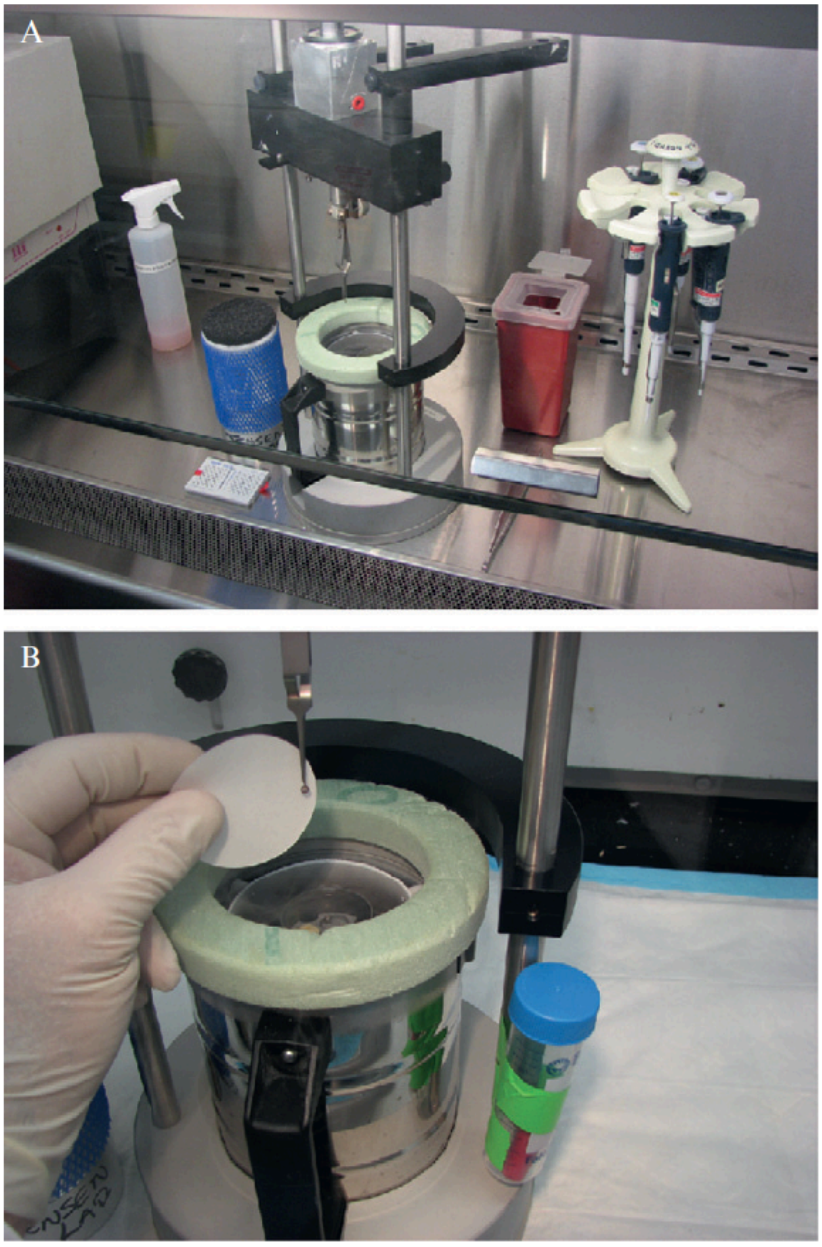

Figure 3.7. (A) Manual plunger (custom-made in the Department of Biochemistry, Max Planck Institute, Martinsried, Germany) in a biosafety cabinet. (B) Manually blotting the liquid from the back of the grid before plunging.

vitrified samples for early cryosectioning experiments (Dubochet et al., 1988). The plunge freezers today are much more sophisticated but owe their design to these early prototypes and years of experience in many laboratories.

A key requirement for obtaining good frozen-hydrated specimens is the ability to produce the uniformly thin vitrified ice layer. In the early days of cryospecimen preparation, many of the "homemade" plunge-freezing instruments required manual blotting of the specimen grid. Although, very high-quality results can be obtained in this manner, manual blotting of the liquid from the surface of a fragile EM grid is often variable, and success depends on the skill of the individual. Manual plungers rely on gravity to plunge the EM grid into a cryogen and have therefore been called "gravity plungers" (Figure 3.7A). Because they are not automated they offer more user control over the blotting. For experiments involving cells growing on the EM grid, harsh blotting pressures from both sides in an automated plunger run the risk of "peeling" the adherent cells off the grid. In the case of gravity plungers, the user can blot from the back of the grid if the intent is not to disturb the cells. The liquid flows into the filter paper through the holes in the carbon. A typical practice is to blot with filter paper from one side until the liquid stops wicking into the filter paper (Figure 3.7B), but a variation of blotting times should be tested for each sample. The gravity plungers are fairly mobile and are often used when traveling to laboratories where specimens are to be frozen on-site. However, the lack of an environment-controlled chamber means that the grids are exposed to atmospheric humidity and temperature, and the users are more exposed to the danger of having sharp tweezers and biological samples near their hands. Modern manual plungers have built-in lights to help visualize the blotting process and a foot pedal for dropping the tweezers.

Currently, there are a variety of automated plunge-freezing instruments designed to make the plunge-freezing process efficient and reproducible (Figure 3.8). Automated plunge freezers provide precise control of several parameters such as humidity, blot pressure, and blot duration in order to eliminate variability in the thickness of the vitrified ice layer. They also provide the means to select, store, and recall a set of

parameters. Finally, automated plunge freezers incorporate a variety of safety features for protecting the user.

The first fully automated, computer-controlled plunge freezer was developed in the late 1990s by Dr. Peter Frederik and Paul Bomans (Frederik and Hubert, 2005). This machine, the VitrobotTM Mark I, was the first in a series of "vitrification robots" now commercially offered through the FEI Company. The Vitrobot Mark IV is the latest version, and can dip the grid into a liquid sample or allow a sample to be pipetted onto the grid from an opening in the side. The Leica EM GP, developed in conjunction with Dr. Gunter Resch, provides one-sided blotting of cell monolayers grown on the specimen grid. An attached stereomicroscope allows the user to view the specimen grid to monitor the process. CryoplungeTM 3 from Gatan, Inc. is a versatile, semiautomated plunge-freezing instrument that provides timed blotting functions, a removable humidity chamber, and the temperature of the liquid ethane can be held just above the melting point of the cryogen. A shield over the cryogenic workstation provides a protective environment for transferring the frozen-hydrated grid to its storage container to prevent the formation of contaminating ice (Melanson, 2009a). The Rapid Immersion Freezer from Electron Microscopy Sciences requires that the specimen be manually blotted, but it is a portable and economical plunge freezer that provides an environmental chamber, temperature control of the cryogen, and freeze-substitution capabilities.

Consistency of results, control parameters, and overall cost are some of the criteria that can be used to determine which type of plunge freezer best suits the needs of the individual investigator. Some laboratories use several different types of plungers based on the features required to prepare their diverse specimens.

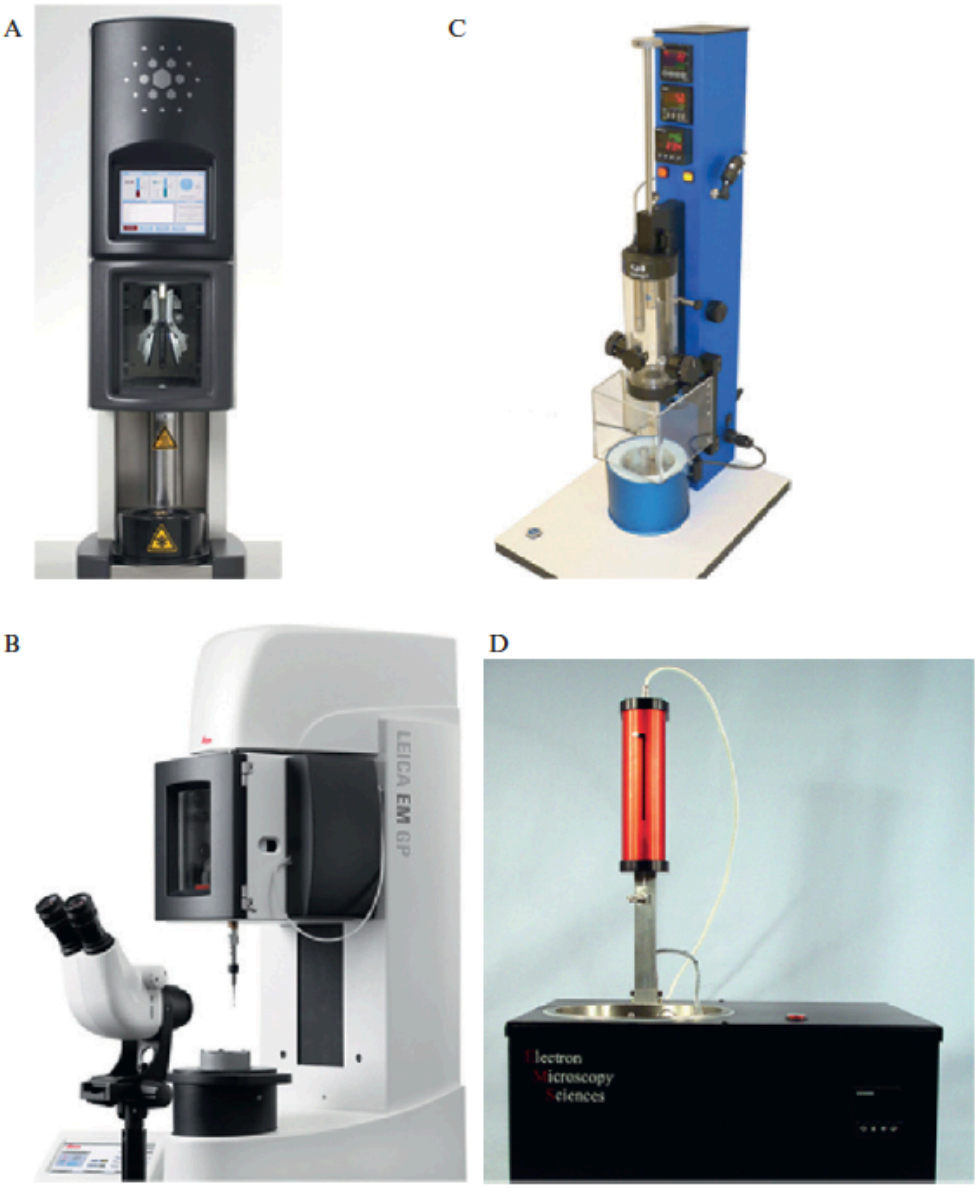

Figure 3.8. Variety of automated plunge freezers. (A) Vitrobot Mark IV, image courtesy of FEI, Inc., Hillsboro, OR. USA. (B) Leica EM GP, image courtesy of Leica Microsystems, Inc., Vienna, Austria. (C) Cryoplunge3, image courtesy of Gatan, Inc., Pleasanton, CA. (D) EMS-002 Rapid Immersion Freezer, image courtesy of Electron Microscopy Sciences, Hatfield, PA, USA.

Safety Considerations

Many people with different samples typically share a plunge freezer. A good practice is to decontaminate surfaces and mechanical parts of the machine with 70%

ethanol before and after every use. In order to keep track of all the samples that come in contact with the machine, an accurate sample history should be kept on a database and staff should be informed of the daily freezing schedule. Only microliter volumes should be cultured and used in freezing procedures, and aseptic technique should be followed in safety hoods. For biohazardous samples in automated plunge freezers, a heat cycle overnight will help to decontaminate the chamber. In manual plungers, the whole machine can be placed in a biosafety cabinet in an isolated room. When using manual plungers, be aware of the location of the foot pedal to avoid premature release of the tweezers and try to keep fingers from ever going beneath the sharp tweezers. The automated plunge freezers are usually controlled by compressed air and have enclosed chambers so the user is less likely to be injured by the tweezers. Training for new staff and yearly refresher lab safety courses should be offered.

Common Problems and Their Diagnoses

Ideally, the ice across a grid will be uniformly thin and vitreous (Figure 3.5A). If the ice and embedded sample is too thick, or there is too much contamination, no electrons will penetrate through the grid. If the ice is at least thin enough for electron penetration, electron diffraction can be used to evaluate the quality of the ice. Vitreous ice is the absence of a detectable crystalline structure and most closely resembles the liquid state of water. It is the preferred form of "ice" for electron imaging and is thought to be the least damaging to structures. However, there are many points in the freezing, transfer, and loading procedures that can cause damaging hexagonal or cubic ice crystals to form: slow cooling of the sample because the cryogen was too warm or had a low thermal conductivity; contaminating ice floating in the cryogen or storage liquid nitrogen; or the frozen sample warming to a temperature higher than –135°C at any time during storage or transfer (Cavalier et al., 2009; Dubochet et al., 1988). Contaminating

ice can adhere to the sample during the transfer of the grid from the cryogen to the storage container or during loading into the microscope. Care should be taken at these points to protect the EM grid by always keeping it in liquid nitrogen, limiting exposure to atmospheric moisture, and always cooling tools in liquid nitrogen before using them to manipulate the grid.

Hexagonal ice is the most common ice on earth and is formed when water molecules attach to each other at each point of their tetrahedral structure and extend indefinitely (Dubochet et al., 1988). This proliferation of bonded molecules can severely damage the cellular ultrastructure. Hexagonal ice can form during slow freezing (streaks of crystalline ice, as seen in Figure 3.9A), or could have condensed after freezing in the form of discrete spherical spots. Cubic ice is very similar to hexagonal ice, except that the bond angles of neighboring water molecules are rotated 180°, making it only stable below −70°C (Dubochet et al., 1988). The dimensions of cubic ice crystals range from 30 nm to 1 mm, and they usually look like fine grain spots (Figure 3.9B). While cubic ice does not tend to cause extensive structural damage to the specimen, it can cause background noise that will disrupt the image. For reference, the three forms of ice and their diffraction patterns can be found in the landmark article by Dubochet et al. (1988).

There are many decisions to be made and conditions to be controlled during the plunge-freezing process in hopes of creating a well-preserved sample in a thin, vitreous ice. However, when the process works, high-resolution structural detail of a sample can be obtained and the reward can be great. Figure 3.10 demonstrates the level of detail that can be achieved in different samples.

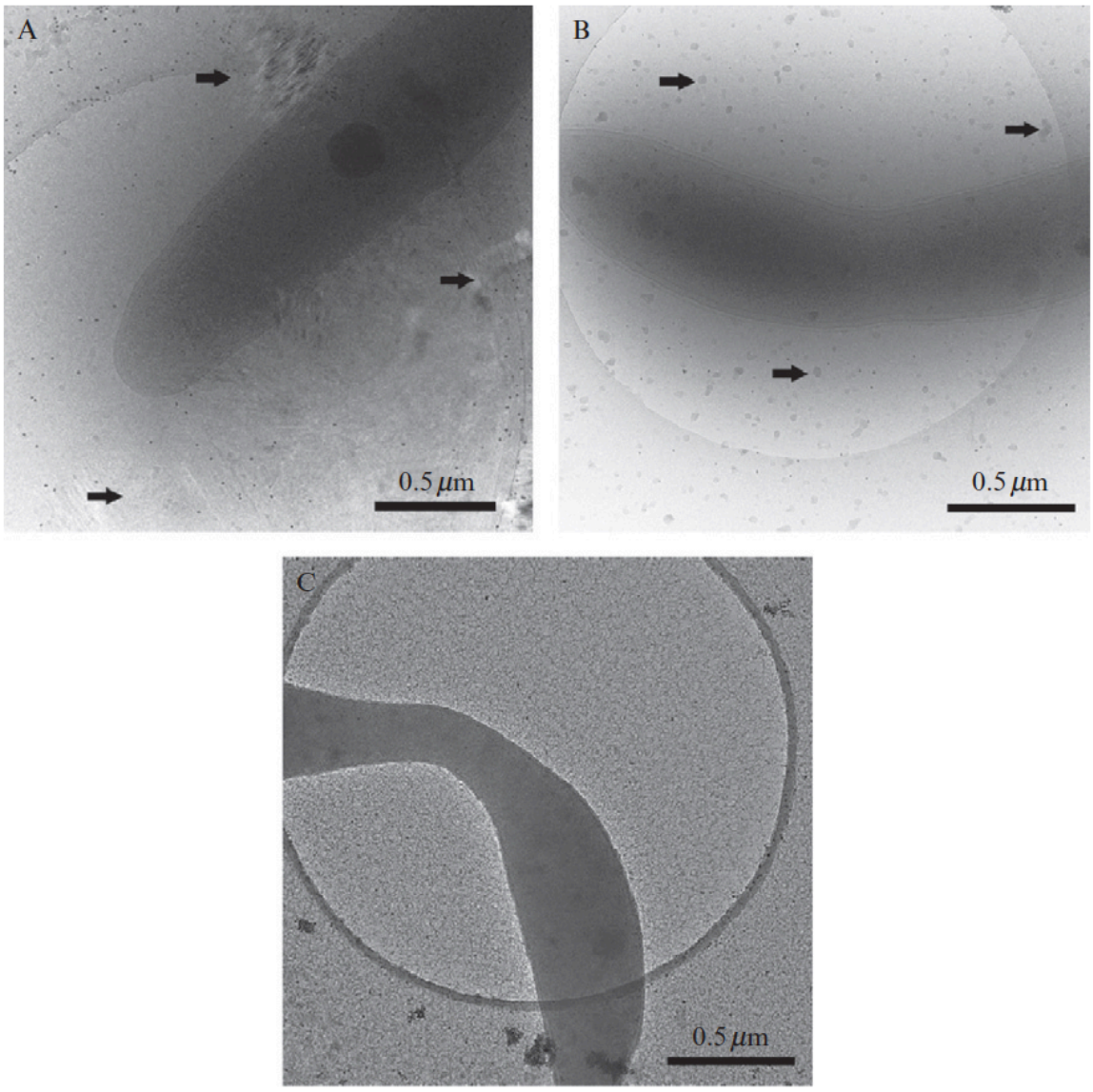

Figure 3.9. Examples of poor ice. (A) Hexagonal ice surrounding the bacterium, indicated by the arrows. (B) Cubic ice contamination, indicated by arrows. (C) The result of extreme rewarming: loss of water and structural detail. Grid bars = 0.5 μm.

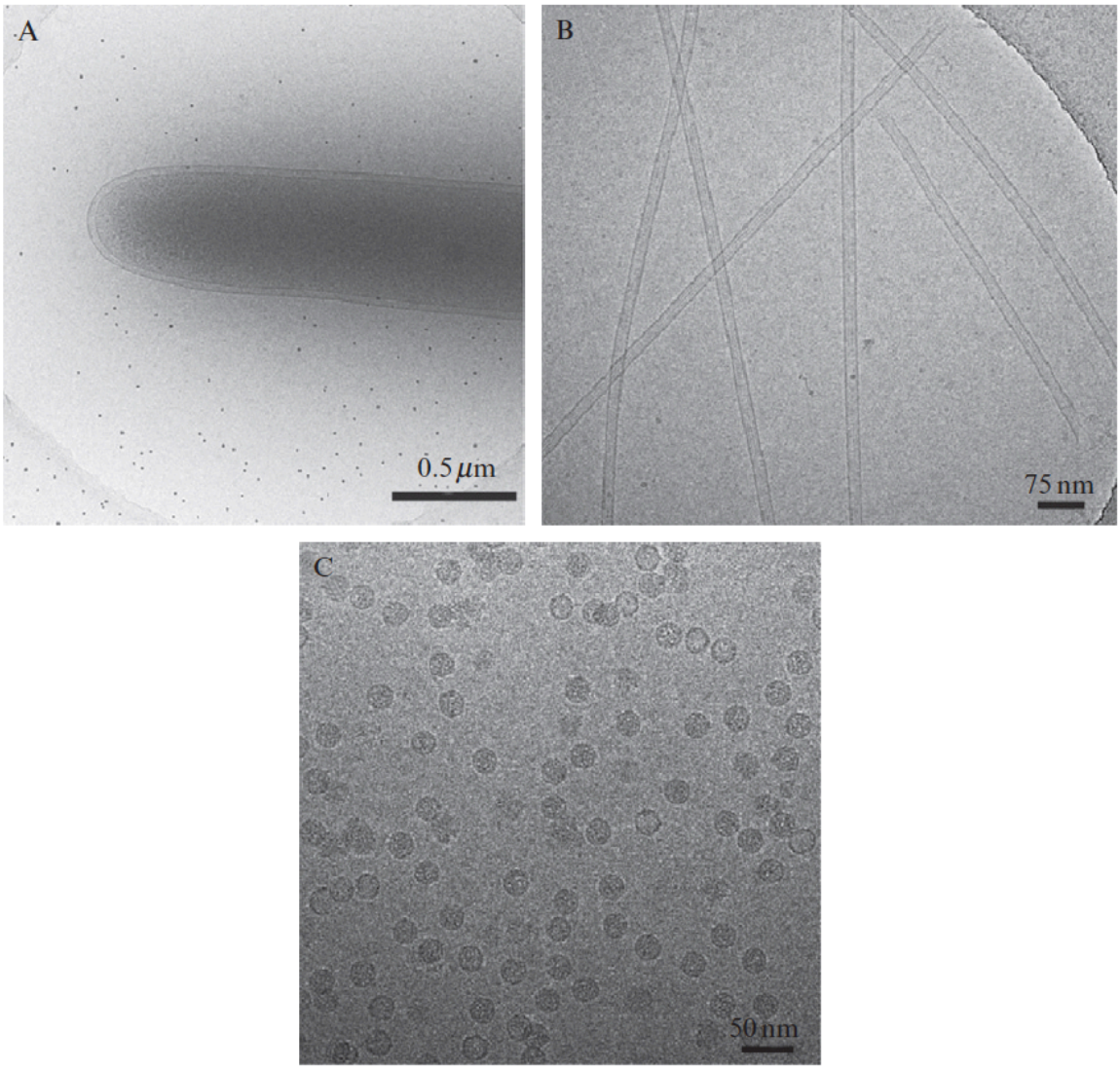

Figure 3.10. Examples of good ice. (A) A bacterium surrounded by gold fiducials, which are used to align tomographic tilt series (grid bar 0.5 μm). (B) Microtubules, image courtesy of Guenter Resch (grid bar = 75 nm). (C) Rhinovirus particles labeled with Fab fragments, image courtesy of Angela Pickl-Herk (grid bar = 50 nm).

Acknowledgements

We wish to thank our colleagues, Steve Coyle and John Hunt of Gatan, Inc., Mark Ladinsky, Elitza Tocheva, Ariane Briegel, and Martin Pilhofer at Caltech, who proofread

the manuscript. FEI, Inc.; Gatan, Inc.; Leica Microsystems, Inc.; and Electron Microscopy Sciences supplied images and data. Guenter Resch, IMP/IMBA Electron Microscopy Facility, Stefan Westermann and Angela Pickl-Herk, at the Max F. Perutz Laboratories in Vienna, Austria, provided specimens, images, and protocols from their experience using the Leica EM GP. Chen Xu, Rosentiel Basic Medical Sciences Research Center, Waltham, MA provided the image for Figure 3.5B. This work was supported in part by NIH grant P01 GM066521 to G.J.J., the Beckman Institute at Caltech, and gifts to Caltech from the Gordon and Betty Moore Foundation and Agouron Institute. Finally, a special thank you to Ted and Chris Pella, Pella, Inc., for their bequest to the Jensen laboratory tomography database project.

3·4

THIN EDGES OF EUKARYOTIC CELLS

Electron cryotomography has become an invaluable tool for imaging thin samples such as bacteria and viruses at high resolution. However, thicker samples such as eukaryotic cells have been more difficult since electrons at 300 kV are scattered inelastically or more than once in samples thicker than about 500 nm. In order to image eukaryotic cells using transmission electron microscopy previously, the sample must be fixed, embedded in plastic, sectioned, and stained, which causes damage to the specimen. Cells can now be cryosectioned or milled with a focused ion beam, but these techniques are technically challenging and still can cause compression and loss of material. Therefore, I started a project to grow adherent eukaryotic cells on EM grids with the goal of imaging the thin outer edges. Cells would be frozen in their native state and would not require fixative or stain. The aim was to image cells infected with HIV to elucidate the uncoating process or TRIM5α restriction factor binding. It is also unknown what role the capsid plays in the HIV life cycle, so by imaging capsids inside cells, we could deduce its function by its structure and how long it stays intact. For example, if the capsid uncoated immediately, it is not likely to function in protection of the genome or transportion to the nucleus. However, if capsids remain intact to the nuclear pore, transportation of the genome to the nucleus could be a primary function. In addition to growing cells thinly on EM grids, the targets would need to be identified using correlative fluorescent light microscopy and electron cryotomography. However, there are very few areas of the EM grid that have regions of cells suitably thin for electrons to penetrate, and additionally fewer targets that have correlated fluorescent spots found in the cryo light microscope.

To infect cells with fluorescently-labeled HIV, and grow cell lines stably expressing rhesus TRIM5α, I collaborated with Thomas Hope at Northwestern University. However, the technique development of plunge freezing thin eukaryotic cells on EM grids was the challenging aspect, and anyone attempting the task would be helped to know what was tried and what worked.

Adherent eukaryotic cell lines prefer to grow on gold, nickel, or molybdenum grids, as copper is toxic. Finder grids with unique symbols imprinted in the metal should be used if the goal is to correlate images from the light and electron microscopes. Grids should be glow discharged for hydrophilicity and radiated under a UV lamp or dipped in ethanol and dried to be sterile. Grids will typically float in media but will easily sink to the bottom of a petri dish or flask if both sides of the grid are dipped in the medium first. Place grids carbon-side-up on the bottom of the plate and add cells to the medium. As the cells settle and adhere to the bottom, they will stick to the carbon-coated grid and spread to form thin outer edges. As long as the cells are kept at 37 °C (for most mammalian cell lines), the cells will lay flat. This is very important to remember if the plunge freezing area is far from the incubator. Cells should be kept on a hot plate or in a small incubator until they are added to the grid for plunge freezing, and care should be taken to plunge the grids rapidly after adding cells. This is because temperatures lower than 37 °C will cause the cells to retract and become too thick. Cell lines with long, thin projections provide many flat areas for EM. The use of poly-lysine can help cells stick to the grid with more affinity, but thick, dried clumps of poly-lysine will result in background noise in the electron microscope. Growing cells at too high a confluence will add weight to the grid, which could damage the carbon and will result in thicker ice during plunge freezing. There should only be one or two cells in each grid square for the thinnest ice. The cell culture medium used should not contain too high of a salt

concentration, as this will cause background noise in the electron microscope. The viscous medium used for cell culture may cause the ice to be too thick or cause a slower freezing process, resulting in crystalline ice. In this case, the grids and cells can be gently washed in PBS, but remember to keep the cells at 37 °C and not shock them with cold PBS. The optimal settings of the plunge freezer are specific to each machine, however a common problem occurred when cells were ripped off the grids by the harsh blotting. Therefore, blotting manually from the back of the grid is often the best approach, but the blotting time must be tested for each set of conditions.

REFERENCES

Adrian, M., Dubochet, J., Lepault, J., and McDowall, A. W. (1984). Cryo-electron microscopy of viruses. *Nature* 308, 32–36.

Aebi, U., and Pollard, T. D. (1987). A glow discharge unit to render electron microscope grids and other surfaces hydrophilic. *J. Electron Microsc Tech* 7, 29–33.

Bellare, J. R., Haridas, M. M., and Li, X. J. (1999). Characterization of microemulsions using fast freeze-fracture and cryo-electron microscopy. *Handbook of Microemulsion Science and Technology* pp. 411–436. New York, Marcel Dekker, Inc.

Booy, F. P., and Pawley, J. B. (1993). Cryo-crinkling: What happens to carbon films on copper grids at low temperature. *Ultramicroscopy* 48, 273–280.

Briggs, J.A., Riches, J.D., Glass, B., Bartonova, V., Zanetti, G., Krausslich, H.G. (2009) Structure and assembly of immature HIV. *Proc Natl Acad Sci USA* 106, 11090–11095.

Carlson, L.A., Briggs, J.A., Glass, B., Riches, J.D., Simon, M.N., Johnson, M.C., Muller, B., Grunewald, K., Krausslich, H.G. (2008) Three-dimensional analysis of budding sites and released virus suggests a revised model for HIV-1 morphogenesis. *Cell Host Microbe* 4, 592–599.

Cavalier, A., Spehner, D., and Humbel, B. M. (2009). *Handbook of Cryo-Preparation Methods for Electron Microscopy*. CRC Press, Boca Raton, FL.

Cerritelli, S., O'Neil, C. P., Velluto, D., Fontana, A., Adrian, M., Dubochet, J., and Hubbell, J. A. (2009). Aggregation behavior of poly(ethylene glycol-bl-propylene sulfide) di- and triblock copolymers in aqueous solution. *Langmuir* 25, 11328–11335.

Dobro, M.J., Melanson, L.A., Jensen, G., and McDowall, A.W. (2010). Plunge freezing for electron cryomicroscopy. *Meth Enzymol 481*, 63-82.

Dubochet, J., Ducommun, M., Zollinger, M., and Kellenberger, E. (1971). A new preparation method for dark-field electron microscopy of biomacromolecules. *J Ultrastruct Res* 35, 147–167.

Dubochet, J., and McDowall, A. (1981). Vitrification of pure water for electron microscopy. *J Microsc* 124, RP3–RP4.

Dubochet, J., McDowall, A. W., Menge, B., Schmid, E. N., and Lickfeld, K. G. (1983). Electron microscopy of frozen-hydrated bacteria. *J Bacteriol* 155, 381–390.

Dubochet, J., Adrian, M., Lepault, J. C., and McDowall, A. W. (1985). Emerging techniques: Cryo-electron microscopy of vitrified biological specimens. *Trends Biochem Tech* 10, 143–146.

Dubochet, J., Adrian, M., Chang, J. J., Homo, J. C., Lepault, J., McDowall, A. W., and Schultz, P. (1988). Cryo-electron microscopy of vitrified specimens. *Q Rev Biophys* 21, 129–228.

Fernandez-Moran, H. (1960). Low-temperature preparation techniques for electron microscopy of biological specimens based on rapid freezing with liquid helium II. *Ann NY Acad Sci* 85, 689–713.

Finnigan, B., Halley, P., Jack, K., McDowall, A., Truss, R., Casey, P., Knott, R., and Martin, D. (2006). Effect of the average soft-segment length on the morphology and properties of segmented polyurethane nanocomposites. *J Appl Polym Sci* 102, 128–139.

Frederik, P. M., and Hubert, D. H. (2005). Cryoelectron microscopy of liposomes. *Methods Enzymol* 391, 431–448.

Gan, L., Chen, S., and Jensen, G. (2008). Molecular organization of Gram-negative peptidoglycan. *Proc Natl Acad Sci USA* 105, 18953–18957.

Glaeser, R., Downing, K., DeRosier, D., Chiu, W., and Frank, J. (2007). *Electron Crystallography of Biological Macromolecules*. Oxford University Press, New York, pp. 1–476.

Grassucci, R., Taylor, D. J., and Frank, J. (2007). Preparation of macromolecular complexes for cryo-electron microscopy. *Nat Protoc* 2, 3239–3246.

Handley, D. A., Alexander, J. T., and Chien, S. (1981). The design and use of a simple device for rapid quench-freezing of biological samples. *J Microsc* 121, 273–282.

Iancu, C. V., Tivol, W. F., Schooler, J., Dias, D. P., Henderson, G. P., Murphy, G. E., Wright, E., Li, Z., Yu, Z., Briegel, A., Gan, L., He, Y., et al. (2006). Electron cryotomography sample preparation using the Vitrobot. *Nat Protoc* 1, 2813–2819.

Kol, N., Shi, Y., Tsvitov, M., Barlam, D., Shneck, R.Z., Kay, M.S., Ruosso, I. (2007) A stiffness switch in Human Immunodeficiency Virus. *Biophysical Journal* 92: 1777-1783.

Kol, N., Tsvitov, M., Hevroni, L., Wolf, S.G., Pang, H-B., Kay, M.S., Rousso, I. (2010) The effect of purification method on the completeness of the immature HIV-1 Gag shell. *J Virol Methods* 169: 244-247.

Kumar, R., Singh, R. K., Kumar, M., and Barthwal, S. K. (2007). Effect of DC glow discharge treatment on the surface energy and surface resistivity of thin film of polypropylene. *J Appl Polym Sci* 104, 767–772.

Lepper, S., Merkel, M., Sartori, A., Cyrklaff, M., and Frischknecht, F. (2010). Rapid quantification of the effects of blotting for correlation of light and cryo-light microscopy images. *J Microsc* 238, 21–26.

McDowall, A. (1984). Ultracryotomy: An investigation of the cryotechnical problems involved in the preparation of frozen-hydrated cells and tissues for high resolution electron microscopy. PhD Thesis, Universite Pierre et Marie Curie, Paris, France.

McDowall, A. W., Chang, J. J., Freeman, R., Lepault, J., Walter, C. A., and Dubochet, J. (1983). Electron microscopy of frozen hydrated sections of vitreous ice and vitrified biological samples. *J Microsc* 131, 1–9.

McDowall, A. W., Hofmann, W., Lepault, J., Adrian, M., and Dubochet, J. (1984). Cryo-electron microscopy of vitrified insect flight muscle. *J Mol Biol* 178, 105–111.

Melanson, L. (2009a). A versatile and affordable plunge freezing instrument for preparing frozen hydrated specimens for cryo transmission electron microscopy (CryoEM). *Microsc Today* 14–17.

Melanson, L. (2009b). The importance of the specimen support film for cryo TEM. http://www.gatan.com/knowhow/knowhow_15/cryo.htm.

Quispe, J., Damiano, J., Mick, S. E., Nackashi, D. P., Fellmann, D., Ajero, T. G., Carragher, B., and Potter, C. S. (2007). An improved holey carbon film for cryo-electron microscopy. *Microsc Microanal* 13, 365–371.

Taylor, K. A., and Glaeser, R. M. (1973). Hydrophilic support films of controlled thickness and composition. *Rev Sci Instrum* 44, 1546–1547.

Taylor, K. A., and Glaeser, R. M. (1974). Electron diffraction of frozen, hydrated protein crystals. *Science* 186, 1036–1037.

Tivol, W. F., Briegel, A., and Jensen, G. (2008). An improved cryogen for plunge freezing. *Microsc Microanal* 14, 375–379.

Wright, E.R., Schooler, J.B., Ding, H J, Kieffer, C., Fillmore, C., Sundquist, W.I., Jensen, G.J. (2007) Electron cryotomography of immature HIV-1 virions reveals the stucture of the CA and SP1 Gag shells. *EMBO* 26: 2218-2226.

Yoshioka, Y., Carragher, B., and Potter, C. S. (2010). CryomeshTM: A new substrate for cryo-electron microscopy. *Microsc Microanal* 16, 43–53.

CONCLUSIONS

Since HIV vaccines have failed to succeed so far, virologists are becoming increasingly aware that more remains to be understood about the virus before an effective treatment can be developed. To gain further understanding of the late stages of the HIV cycle, including viral exit and maturation, I studied the structural biology of the protein complexes integral to these processes. I also further developed the methods involved in HIV purification, plunge freezing, and electron microscopy of thin eukaryotic cells.

In pursuit of mechanistic insight into viral release, I studied the high-resolution structural details of the ESCRT complex. ESCRT is not only essential to HIV infections; it is also involved in sorting ubiquitin-tagged cargo into multivesicular bodies as well as membrane scission during cytokinesis in eukaryotes and archaea. By imaging the ESCRT complex of proteins *in vitro* and in dividing archaea, I revealed more about ESCRT's structure and function. This work led me to a model for membrane scission by ESCRT, which is vital in cellular processes across biological kingdoms.

In order to gain knowledge about how HIV capsids assemble, I studied the irregular capsids that did not close into the typical conical shape. By combining electron cryotomography (ECT) and fluorescence microscopy, we showed that ~25% of viral capsids infecting living cells have large holes, seams, or extra sheets. These observations are consistent with a model of assembly that involves the union in space of two growing edges, as shown by coarse-grain modeling. Since capsids frequently contain large holes, the role of capsid may not be to protect the viral genome, as previously proposed (Tanchou et al., 1995). Together, it is an interdisciplinary story that addresses the fundamental question of what the purpose of the capsid could be.

It will be an important advance to the field of HIV structural biology to image infectious particles inside cells using ECT. There is a great deal left to learn about how

the virus interacts with the host cell. It was important groundwork to establish standardized protocols for purification of viral particles, plunge freezing, and growing thin eukaryotic cells on EM grids. The next steps involve correlating fluorescence images of GFP-tagged virions inside cells with electron cryotomograms. Because HIV particles inside cells may not be identifiable, it will be important to correlate with fluorescent images to within less than a micrometer range. I began this project at Northwestern University by mapping areas of infected cells with fluorescence microscopy at room temperature, plunge freezing the grids, transporting them back to Caltech, and collecting tomograms of the same targets. However, the protocols were not well established at the time and the ice was too thick on the grids to find the cells in the electron microscope. The Jensen Lab now has a cryo fluorescence microscope, so a better approach may be to plunge freeze the grids first, then map the particles in the cryo fluorescence microscope, and then collect tomograms of the same targets. This would eliminate movement of the particles as a factor when correlating the images from both microscopy methods.

REFERENCES

Tanchou, V., Gabus, C., Rogemond, V., and Darlix, J.L. (1995). Formation of stable and functional HIV-1 nucleoprotein complexes in vitro. *J Mol Biol 252*, 563-571.

APPENDIX A

PNAS PNAS PNAS PNAS

Universal architecture of bacterial chemoreceptor arrays

Ariane Briegel[a,b], Davi R. Ortega[c,d], Elitza I. Tocheva[a], Kristin Wuichet[d], Zhuo Li[a,b], Songye Chen[a], Axel Müller[e], Cristina V. Iancu[a,1], Gavin E. Murphy[a,2], Megan J. Dobro[a], Igor B. Zhulin[d,f], and Grant J. Jensen[a,b,3]

Divisions of [a]Biology and [e]Chemistry and [b]Howard Hughes Medical Institute, California Institute of Technology, Pasadena, CA 91125; Departments of [c]Physics and [d]Microbiology, University of Tennessee, Knoxville, TN 37996; and [f]BioEnergy Center and Computer Science and Mathematics Division, Oak Ridge National Laboratory, Oak Ridge, TN 37831

Edited by Laura L. Kiessling, University of Wisconsin, Madison, WI, and approved July 20, 2009 (received for review May 11, 2009)

Chemoreceptors are key components of the high-performance signal transduction system that controls bacterial chemotaxis. Chemoreceptors are typically localized in a cluster at the cell pole, where interactions among the receptors in the cluster are thought to contribute to the high sensitivity, wide dynamic range, and precise adaptation of the signaling system. Previous structural and genomic studies have produced conflicting models, however, for the arrangement of the chemoreceptors in the clusters. Using whole-cell electron cryo-tomography, here we show that chemoreceptors of different classes and in many different species representing several major bacterial phyla are all arranged into a highly conserved, 12-nm hexagonal array consistent with the proposed "trimer of dimers" organization. The various observed lengths of the receptors confirm current models for the methylation, flexible bundle, signaling, and linker sub-domains in vivo. Our results suggest that the basic mechanism and function of receptor clustering is universal among bacterial species and was thus conserved during evolution.

bacterial ultrastructure | chemotaxis | electron cryo-tomography

Most motile prokaryotes rely on a chemosensory system to control their movement toward favorable environmental conditions (1). This process of chemotaxis depends on transmembrane chemoreceptors called methyl-accepting chemotaxis proteins (MCPs). MCPs can be classified by topology type (2) and signaling domain class (3). Topology type I MCPs have large periplasmic ligand-binding domains (2) and an elongated cytoplasmic region consisting of a HAMP domain (i.e., histidine kinases, adenylyl cyclases, methyl-binding proteins, and phosphatases) followed by a signaling domain, which in turn is composed of "methylation," "flexible bundle," and "signaling" sub-domains (3, 4) [supporting information (SI) Fig. S1*A*]. MCPs cluster together with other chemotaxis proteins including CheA and CheW in large arrays at the cell pole (5–9).

Because MCPs act cooperatively, their arrangement and interactions within the arrays are critical to their function. Based on the crystal structure of the Tsr receptor from *Escherichia coli* (10), as well as cross-linking and other studies (11, 12), it seems clear now that the basic functional unit in that organism is a "trimer of receptor dimers." It was further proposed that, in *E. coli*, trimers of receptor dimers form a hexagonal array with a lattice spacing of 20 nm (13). A subsequent electron cryo-tomography (ECT) study showed that overexpressed Tsr chemoreceptors in *E. coli* pack into a hexagonal lattice with a center-to-center spacing of 7.5 nm (14–17). In these overexpression strains, the receptors surprisingly form a "zipper-like" double layer, in which large invaginations of the inner membrane allow the cytoplasmic tips of one layer to interact with the cytoplasmic tips of a second, facing layer. This arrangement was at one point proposed to represent the activated form of the receptors (18), but its physiologic relevance was later refuted (19). Adding further complication, MCPs from *Thermotoga maritima* crystalized as rows of dimers (20). This structure, combined with pulsed ESR and crystallographic studies of a CheA-CheW dimer, led to a third "hedgerows of dimers" model for the architecture of chemoreceptor arrays (20). Finally, through direct imaging of intact *Caulobacter crescentus* cells, we (21) and others (22) showed that the chemoreceptors in that organism are arranged in a hexagonal lattice whose 12-nm spacing suggested that trimers of receptor dimers occupied each threefold symmetric vertex. Whereas the MCPs of *E. coli* and 16 of the 18 MCPs of *C. crescentus* belong to the same signaling domain class (36H), those from *T. maritima* belong to a different class (44H) (3). Moreover, certain residues that were seen to make important contacts in the *E. coli* Tsr trimer-of-dimers structure are not conserved in all MCPs. Phenylalanine 373, for example, is involved in hydrophobic trimerization interactions in the Tsr crystal structure, but is replaced by glutamate in all the *T. maritima* chemoreceptors (3, 10, 20). Thus, based on structural and bioinformatics data, it was unclear whether receptors from different MCP classes and organisms clustered similarly, or if not, how many architectures there might be. By imaging WT cells in near-native states, here we show that the chemoreceptors of diverse species from 6 different signaling domain classes are all arranged into a highly conserved, 12-nm hexagonal array consistent with a single "trimer of receptor dimers" functional unit at each vertex.

Results and Discussion

Position of Chemoreceptor Arrays Within Cells. To visualize the arrangement of chemoreceptors in diverse bacteria, we selected 13 distantly related organisms, which together possess receptors from all 7 major signaling domain classes (3) (Table 1) and recorded nearly 700 ECTs of intact, frozen-hydrated cells. Previous immunolabeling (19) and correlated light and EM studies (21) had already established that, in *E. coli* and *C. crescentus*, chemoreceptor arrays can be recognized as clusters of thin, pillar-like densities extending from the inner membrane to a prominent "base plate" formed by CheA and CheW 20 to 30 nm below. Similar structures were seen in all 13 organisms imaged here (Figs. 1 and 2), but their locations within the cell varied. As in *E. coli*, the chemoreceptor arrays in *Magnetospirillum magneticum, Rhodobacter sphaeroides, Treponema primitia, T. maritima*, and *Listeria monocytogenes* were polar. In contrast, the arrays in *Helicobacter hepaticus* and *Campylobacter*

Author contributions: A.B. and G.J.J. designed research; A.B., D.R.O., E.I.T., K.W., Z.L., S.C., A.M., C.V.I., G.E.M., and M.J.D. performed research; A.B., D.R.O., E.I.T., K.W., and I.B.Z. analyzed data; and A.B., D.R.O., E.I.T., I.B.Z., and G.J.J. wrote the paper.

The authors declare no conflict of interest.

This article is a PNAS Direct Submission.

[1]Present address: Department of Biochemistry and Molecular Biology, Rosalind Franklin University, The Chicago Medical School, North Chicago, IL 60064.

[2]Present address: Laboratory of Cell Biology, Center for Cancer Research, National Cancer Institute, National Institutes of Health, Bethesda, MD 20892.

[3]To whom correspondence should be addressed. E-mail: jensen@caltech.edu.

This article contains supporting information online at www.pnas.org/cgi/content/full/0905181106/DCSupplemental.

MICROBIOLOGY

Table 1. Summary of measurements of 13 different bacterial species obtained by ECT

Bacterium	Phylum	Average cell diameter × length (μm)	MCP class (no. of receptors)[a]	Location	Distance from IM to base plate (nm)	Lattice (nm)	Surface area (nm²), estimated no. of receptors[b]
Thermotoga maritima	Thermotogae	0.5–1 × >1.5	44H (**6**) Unc (**1**)	Polar	25	12	≈97 k, ≈9,400
Listeria monocytogenes	Firmicutes	0.5 × >1.5	44H (**1**), 24H (**1**)	Polar	26	None observed	≈30 k, ≈2,900
Acetonema longum	Firmicutes	0.3 × variable length (>10)	44H (**20**,**2**), Unc (**10**)	Subpolar	26	12	≈51 k, ≈5,000
Borrelia burgdorferi	Spirochaetes	0.2 × variable length (>10)	34H (**2**), 48H (**1**), Unc (**3**)	Subpolar	27	None observed	NA
Treponema primitia	Spirochaetes	0.4 × 3–8	48H (**10**,**1**), 40H (**1**) Unc (**1**,**2**)	Polar	28	12	≈15 k, ≈1,500
Caulobacter crescentus	Alpha-proteobacteria	0.4–0.7 × 0.9–2.2	36H (**9**,**7**), 38H (**1**), Unc (**1**)	Polar, convex side (**21**)	31	12	≈17 k, ≈1,700
Magnetospirillum magneticum	Alpha-proteobacteria	0.5 × 2–10	38H (**39**,**23**), 40H (**2**), 44H (**1**), Unc (**7**)	Polar	28	12	≈12 k, ≈1,200
Rhodobacter sphaeroides	Alpha-proteobacteria	0.7–0.8 × 1.3–1.4	34H (**7**,**1**), 36H (**2**), Unc (**2**)	Polar	21	12	≈22 k, ≈2,200
Escherichia coli	Gamma-proteobacteria	0.5–1.3 × 2–5	36H (**4**,**1**)	Mainly polar (**19**)	22	12	≈53 k, ≈5,200
Vibrio cholera	Gamma-proteobacteria	0.8–0.9 × > 1.5	40H (**32**,**10**), 44H (**1**), 36H (**2**), 24H (**2**), Unc (**2**)	Polar, convex side	25	12	≈121 k, ≈11,800
Halothiobacillus neapolitanus	Gamma-proteobacteria	0.4–0.5 × 1.6–1.7	40H (**4**)	Polar	24	12	≈31 k, ≈3,000
Helicobacter hepaticus	Epsilon-proteobacteria	0.3 × 1.5–4	28H (**4**,**1**) 40H (**3**) Unc (**1**)	Polar "cap"	24	12	≈112 k, ≈10,900
Campylobacter jejuni	Epsilon-proteobacteria	0.4 × 0.5–5	28H (**4**), 40H (**1**,**1**), 24H (**3**), Unc (**1**)	Polar "cap"	24	12	≈144 k, ≈14,400

[a], The receptors present in each genome are listed by organism. The number of receptors in each signaling domain class is listed in column 4 (*Unc*, uncharacterized). After each class, the number of MCPs that do (bold) and do not (regular print) belong to topology class I appear in parenthesis.
[b], Number of receptors per array (last column) estimated from the observed (average) surface areas assuming hexagonally packed receptor trimers of dimers (21).

jejuni formed a polar "collar" completely surrounding the tip of the cell, but with a gap at the apex occupied by the flagellar motor. As in *C. crescentus* (21), the arrays in *Vibrio cholerae* were polar but consistently localized to the convex side of the crescent-shaped cells. Receptor arrays in *Acetonema longum* and *Borrelia burgdorferi* were typically subpolar but inconsistently positioned. The array in *A. longum* was found, for instance, to range from immediately adjacent to the pole to nearly 1 μm away. Although

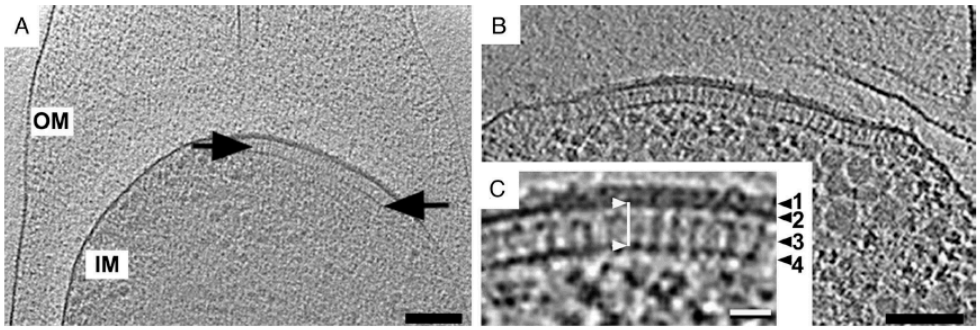

Fig. 1. Characteristic appearance of chemoreceptor arrays in vivo. (*A*) A 55-nm-thick tomographic slice through a *T. maritima* cell pole (signaling domain class 44H). Typical features like the inner membrane (*IM*) and outer membrane (*OM*) and the enclosed extended periplasm are clearly visible. The arrows indicate the location of the chemoreceptor array within the inner membrane and densely packed cytoplasm. (Scale bar: 100 nm.) (*B*) A 3-nm-thick tomographic slice through the pole of a *T. maritima* cell treated with polymyxin B. The reduced cytoplasmic crowding clarifies chemoreceptor features compared with those in untreated cells. (Scale bar: 100 nm.) (*C*) Enlarged view of the array shown in *B*: *1*, periplasmic receptor domains; *2*, inner membrane; *3*, cytoplasmic receptor domains; *4*, CheA-CheW base plate. The line between the white arrows illustrates how the array heights were measured (from the center of the inner membrane to the center of the CheA-CheW base layer). (Scale bar: 25 nm.)

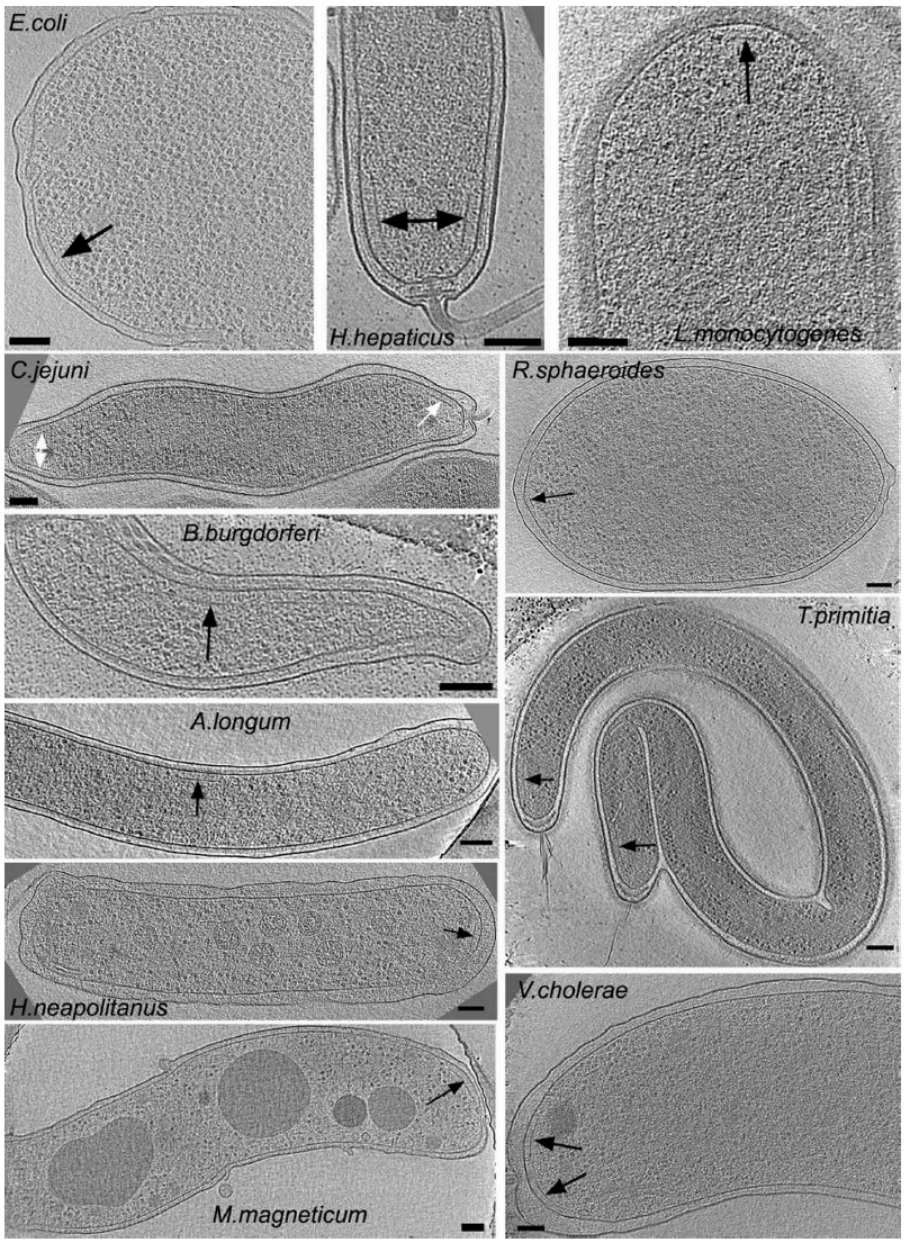

Fig. 2. Chemoreceptor arrays in diverse bacteria. Tomographic slices through cells of 11 different species illuminating the varied location but consistent appearance of the arrays. (*T. maritima* and *C. crescentus* are not shown, because they are available in Fig. 1 and ref. 21, respectively.) (Scale bars: 100 nm.)

cytoplasmic MCP arrays have been reported in *R. sphaeroides* (23–25), none were observed here.

Receptor Lengths. Despite the similarity of the arrays, the distance between the base plate and the inner membrane varied among species (Table 1). Measured values ranged from 21 nm in *R. sphaeroides* to 31 nm in *C. crescentus*, but were constant within each species. Because distinct periplasmic densities were observed above the arrays in nearly all of the cells, and only topology type I MCPs have large periplasmic domains, we infer that at least the majority of the MCPs composing these arrays were of topology type I. In 7 of the organisms imaged (*E. coli*, *V. cholerae*, *Halothiobacillus neapolitanus*, *A. longum*, *L. monocytogenes*, *R. sphaeroides*, and *T. maritima*), all of the topology type I MCPs in their respective genomes belong to a single (but different for each organism) signaling domain class (Table 1). When the observed distance between the inner membrane and base plate was plotted against the number of relevant residues (counted from the middle of TM2 to the conserved glycine at the tip of the hairpin) in the corresponding receptor sequences, there was a strong correlation with a slope of 0.142 nm per residue (Fig. 3*A*). Because all the MCPs shown in Fig. 3*A* contain a single HAMP domain, and its size is constant (26, 27), its presence should not affect the slope. The remarkable match of the observed slope with the rise per residue seen in the coiled coil crystal structure of a *T. maritima* receptor's signaling domain (0.145 nm/residue) (20) therefore strongly supports the sequence-based prediction (3) that the methylation, flexible bundle, and signaling sub-domains of all receptors are coiled coils in vivo.

The genomes of the other 6 organisms imaged (*C. jejuni*, *H. hepaticus*, *B. burgdorferi*, *T. primitia*, *M. magneticum*, and *C. crescentus*) each contain topology type I MCPs belonging to 2 different signaling domain classes, and some of their MCPs possess linkers and/or an additional HAMP domain (Fig. S1 *B* and *C*). It was therefore unclear which MCPs were forming the arrays in the imaged cells. When the observed receptor lengths were simply plotted against the total number of relevant residues in the various topology type I receptors present; however, in all but one of these organisms, only one of the 2 signaling domain classes matched the trend line (Fig. 3*B*). In the cases of *B. burgdorferi* and *T. primitia*, for instance, the class 48H MCPs matched the trend line, but the class 34H (*B. burgdorferi*) and unclassified (*T. primitia*) receptors did not. In the cases of *C. jejuni* and *H. hepaticus*, receptors of the 40H class matched the trend line, but those of class 28H, which contain long (≈95 residue) extra undefined regions between their HAMP and signaling domains (Fig. S1*C*), did not. In the case of *M. magneticum*, its class 38H receptors, which contain extra linkers (of ≈30 residues), fit the trend line, but its class 40H receptors did not. Finally, in the exceptional case of *C. crescentus*, both its class 36H and 38H receptors contain extra linkers, but neither matched the trend line well. However, close inspection of the sequences revealed that the class 36H receptors also contain a second HAMP domain. Because a HAMP domain is expected to be approximately 4 nm shorter than a (presumably) α-helical linker of the same number of residues (26), if this deficit is taken into account, the observed length of the class 36H receptors also matches the trend line well. Our interpretations are therefore that (*i*) in the single growth condition used for each particular species, the arrays were composed of receptors from a single predominant signaling class that could be identified by the observed distance between the inner membrane and base plate; (*ii*) the methylation, flexible bundle, and signaling sub-domains present in all 13 organisms are in fact coiled coils; and (*iii*) the linkers in the receptors imaged are α-helical in vivo. Assuming this is correct, our data contained images of 5 major signaling domain classes (44H, 40H, 38H, 36H, and 34H) and one minor signaling domain class (48H).

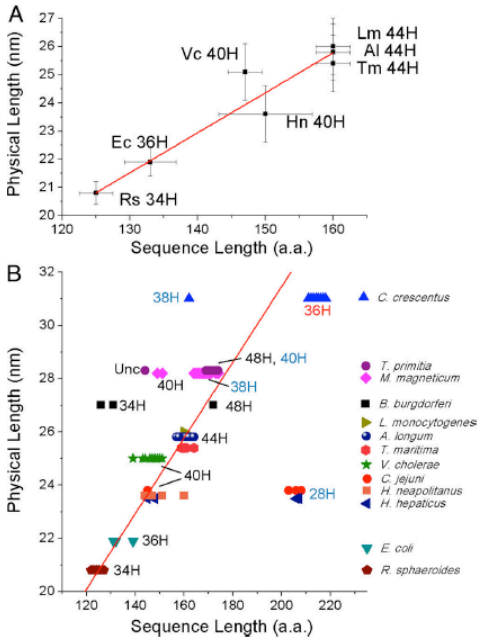

Fig. 3. Correlation between observed physical length and predicted sequence length. (*A*) Organisms possessing a single class of topology type I receptors. Physical length and sequence length were measured as described in *Materials and Methods*. The sequence length is an average of all topology type I MCPs in the given genome. Vertical bars indicate SD of measurements from different cryo-tomograms and positions within the array, horizontal bars indicate the larger of the SD of the various MCP sequence lengths present in the genome or the estimated uncertainty in the position of the transmembrane region (≈5 residues, see *Materials and Methods*). The line is a least-squares fit whose slope confirms that the cytoplasmic domains of the receptors form extended coiled coils. *Al*, *A. longum*; *Ec*, *E. coli*; *Hn*, *H. neapolitanus*; *Lm*, *L. monocytogenes*; *Rs*, *R. sphaeroides*; *Tm*, *T. maritima*; and *Vc*, *V. cholera*. (*B*) All topology type I MCPs in all 13 organisms imaged. Each MCP sequence in each organism is represented by a symbol, color- and shape-coded by organism (*Right*). All the MCPs of a particular organism appear at the same height on the graph (the measured distance between the inner membrane and base plate layer), even though it is not known which were actually imaged. MCPs of particular signaling domain classes cluster closely (3), and are labeled with the color of the label itself (e.g., *34H*, *36H*) indicating whether the receptors of that class are typical (black), contain extra linkers (blue), or contain both extra linkers and a second HAMP domain (red; see Fig. S1*C*). The sequence lengths of typical receptors (i.e., those without extra linkers and HAMP domains) are seen to progress steadily with class number across the graph from left to right. Receptors with additional linkers or a second HAMP domain (blue and red labels) appear further to the right than expected because of their extra residues. The Unc label represents an MCP that does not correspond to a known length class, but was given a sequence length measurement as described in *Materials and Methods*. The graph shows that within the organisms that possess 2 classes of receptors (*C. jejuni*, *H. hepaticus*, *B. burgdorferi*, *T. primitia*, *M. magneticum*, and *C. crescentus*), only one class matches the trend line found in *A*, suggesting that it was the receptor class forming the arrays.

Lattice Arrangement. Eleven of the species imaged here presented clear "top" views (i.e., slices parallel to the cytoplasmic membrane) of the arrays (those of *L. monocytogenes* and *B. burgdorferi* were inaccessible; see Fig. 4). Surprisingly, they all revealed

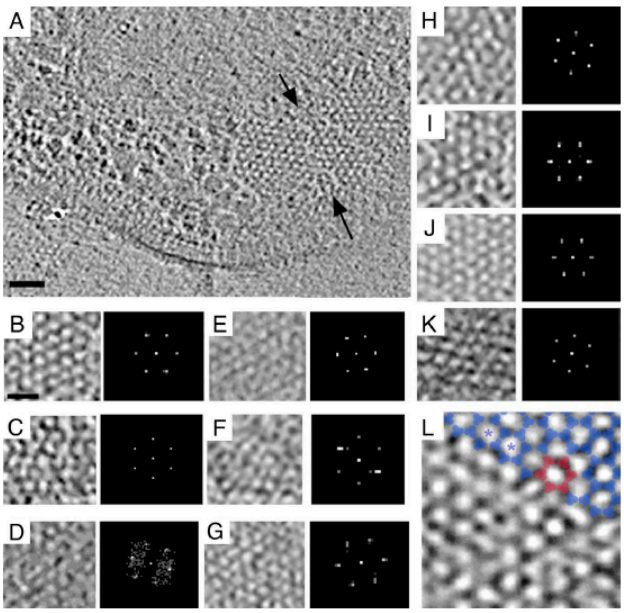

Fig. 4. Universally conserved 12-nm hexagonal arrangement of receptor. (*A*) "Top" view of a chemoreceptor array (black arrows) in *T. maritima* (signaling domain class 44H). (Scale bar: 50 nm.) (*B–K*) Top views (*Left*) and power spectra (*Right*) of receptor arrays all reveal the same ≈12-nm hexagonal lattice. *B*, *T. maritima*; *C*, *A. longum*; *D*, *C. jejuni*; *E*, *H. hepaticus*; *F*, *M. magneticum*; *G*, *H. neapolitanus*; *H*, *R. sphaeroides*; *I*, *E. coli*; *J*, *V. cholerae*; *K*, *T. primitia*. (Scale bars: 25 nm; power spectra enlarged.) (*L*) Trimer of dimers (blue) fit into the vertices of the hexagonal lattice in a chemoreceptor array (*V. cholerae*). Six trimers of dimers (red) enclose one hexagon. The spacing from the center of one hexagon to the center of an adjacent one is consistently 12 nm (blue asterisks).

the same approximate 12-nm honeycomb-like hexagonal arrangement immediately above the base layer as observed previously in *C. crescentus*. We conclude that, throughout the entire wide range of species and receptor classes imaged here [including WT *E. coli* and *T. maritima*, for which MCP crystal structures and alternative models exist, as well as organisms from 6 diverse taxonomic groups that span the bacterial kingdom (Fig. S2 and *SI Appendix*)], trimers of receptor dimers pack at the vertices of a 12-nm hexagonal lattice. In all the arrays we observed, the honeycomb-like lattice was clearest just above the base plate but deteriorated as it rose toward the inner membrane. These observations support the notion that the major architectural contacts occur near the signaling sub-domain of chemoreceptors (4). Although the basic arrangement of all of the arrays was clearly hexagonal, none of the arrays were perfectly regular, supporting the idea that the degree of local order could reflect activation and/or regulation (22). The size of the arrays, and thus the estimated number of receptors, varied by an order of magnitude (from ≈1,200 in *M. magneticum* to ≈14,400 in *C. jejuni*; Table 1), without obvious correlation to the cell size or bacterial taxonomy.

Conclusion

Tightly coupled, communicating chemoreceptor arrays are thought to enable the main features of the signaling mechanism: heightened sensitivity (28), signal gain (29), cooperativity (30, 31), and adaptation (32, 33). The universal hexagonal architecture and secondary structure of chemoreceptor arrays we observed in diverse bacterial species therefore implies that the trimer-of-dimers arrangement and the underlying signaling mechanism are preserved over long evolutionary distances (Fig. S2). The main features of the signaling mechanism that are being revealed in *E. coli* are therefore likely to be applicable to other bacterial species. This is important because, although chemotaxis is critical to pathogenic (34) and symbiotic (35) interactions of bacteria with higher organisms, the molecular details of this system can at present be studied in only a few model organisms.

Materials and Methods

Strains, Sample Preparation, EM Data Collection, and Image Processing. Bacterial strains [*C. crescentus* CB15N, *E. coli* RP437 and MG1655, *T. maritima* MSB8/DSM 3109, *V. cholerae* TRH7000, *M. magneticum* sp. AMB-1, *H. hepaticus* ATCC 51449, *C. jejuni* ATCC 29428, *R. sphaeroides* NCIB 8253, *B. burgdorferi* B31 cells ATCC 35210, *L. monocytogenes* strain 10403S (serotype 1/2a), *A. longum* APO-1 DSM 6540, *T. primitia* strain ZAS-2, *H. neapolitanus* C2 ATCC 23641] were grown in standard media. To flatten the thickest cell types slightly, *E. coli* cells were incubated with 462 IU/mL penicillin G for 60 min at 30 °C (36) and *T. maritima* cells were treated with 1 mg/mL polymyxin B for 10 h on ice. Cultures were plunge-frozen across EM grids as described (37). Standard EM tilt series were collected on 300 kV electron cryo-microscopes and 3D reconstructions were calculated as described (38, 39). The hexagonal arrangement of the arrays was clearly evident in both the raw tomographic slices and their power spectra. *SI Text* contains further details.

MCP Sequences and Classification. MCP sequences from the complete genomes (*E. coli*, *C. crescentus*, *T. maritima*, *V. cholerae*, *M. magneticum*, *H. hepaticus*, *C. jejuni*, *R. sphaeroides*, *B. burgdorferi*, *L. monocytogenes*) were downloaded from the MIST database (40). For the draft genomes (*A. longum*, *T. primitia*, and *H. neapolitanus*), contigs were subjected to the GeneMark gene finding program (41) to obtain the translated sequences. MCPs were then identified

in translated proteins using the MCPsignal domain model [Pfam database (42) accession number PF00015] and the HMMER software package (43). The final set contained 223 MCPs from 13 genomes (Table 1). MCPs were assigned to signaling classes and membrane topology types as previously described (3, 44). Sequences that did not match any established signaling class were left unclassified ("unc" in Table 1).

Physical and Sequence Length Measurements. Because of the well understood point-spread function in ECT (including a final low-pass filter), the edges of objects appear less sharp in tomograms than they really are. The exact positions of the top and bottom of the inner membrane or CheAW base plate are therefore difficult to ascertain. However, the location of their midplanes are highly reliable, as the point-spread function only smooths (and does not shift) peaks. The distance between the peaks (i.e., midplanes) of the inner membrane and CheAW base plate was therefore used as an estimate of the physical length of the cytoplasmic portion of the MCPs. Likewise, the center of transmembrane regions can be more reliably predicted from sequence than the edges, and neither is exact because transmembrane helices likely drift up and down a few residues within the fluid bilayer. The sequence length of the "cytoplasmic" domains was therefore taken to be the number of amino acids from the middle of TM2 to the conserved glycine at the tip of the hairpin (Gly-390 in the Tsr protein of *E. coli*; Fig. S1*A*). Although it is not yet known exactly where the tip of the hairpin is with respect to the midplane of the CheAW base plate, because whatever discrepancy that might exist is likely to be the same for all the receptors, it should not affect the slope of the correlation between physical and sequence lengths across different receptor classes.

ACKNOWLEDGMENTS. The authors wish to thank Eric Matson, Reinhard Rachel, Kevin Bruhn, Gordon Cannon, Alan Barbour, Sarkis Mazmanian, Jeanette Beatty, Maria Sandkvist, Dianne Newman, and John S. Parkinson for bacterial strains; Howard Berg for the penicillin treatment protocol for *E. coli*; Jane H. Ding for computational support; Juergen Plitzko, Alasdair McDowall and Jian Shi for EM support; and Roger Alexander, Luke Ulrich, and Bhanu Rekapalli for assistance and helpful suggestions. The authors also thank Professor Wolfgang Baumeister (Max Planck Institute for Biochemistry, Martinsried, Germany) for the permission to include the data from *T. maritima* (which was collected in his laboratory and under his supervision) in this study. This work was supported in part by National Institutes of Health Grants R01 AI067548 and P50 GM082545 (to G.J.J.) and R01 GM72285 (to I.B.Z.), as well as the Howard Hughes Medical Institute, the Beckman Institute at Caltech, and gifts to Caltech from the Gordon and Betty Moore Foundation and Agouron Institute.

1. Wadhams GH, Armitage JP (2004) Making sense of it all: bacterial chemotaxis. *Nat Rev Mol Cell Biol* 5:1024–1037.
2. Zhulin IB (2001) The superfamily of chemotaxis transducers: from physiology to genomics and back. *Adv Microb Physiol* 45:157–198.
3. Alexander RP, Zhulin IB (2007) Evolutionary genomics reveals conserved structural determinants of signaling and adaptation in microbial chemoreceptors. *Proc Natl Acad Sci USA* 104:2885–2890.
4. Hazelbauer GL, Falke JJ, Parkinson JS (2008) Bacterial chemoreceptors: high-performance signaling in networked arrays. *Trends Biochem Sci* 33:9–19.
5. Boukhvalova MS, Dahlquist FW, Stewart RC (2002) CheW binding interactions with CheA and Tar: importance for chemotaxis signaling in *E. coli*. *J Biol Chem* 277:22251–22259.
6. Bray D, Levin MD, Morton-Firth CJ (1998) Receptor clustering as a cellular mechanism to control sensitivity. *Nature* 393:85–88.
7. Gestwicki JE, Kiessling LL (2002) Inter-receptor communication through arrays of bacterial chemoreceptors. *Nature* 415:81–84.
8. Lybarger SR, Maddock J (2001) Polarity in action: asymmetric protein localization in bacteria. *J Bacteriol* 183:3261–3267.
9. Maddock JR, Shapiro L (1993) Polar location of the chemoreceptor complex in the *Escherichia coli* cell. *Science* 259:1717–1723.
10. Kim KK, Yokota H, Kim SH (1999) Four-helical-bundle structure of the cytoplasmic domain of a serine chemotaxis receptor. *Nature* 400:787–792.
11. Boldog T, Grimme S, Mingshan L, Sligar SG, Hazelbauer GL (2006) Nanodiscs separate chemoreceptor oligomeric states and reveal their signaling properties. *Proc Natl Acad Sci USA* 103:11509–11514.
12. Studdert CA, Parkinson JS (2007) In vivo crosslinking methods for analyzing the assembly and architecture of chemoreceptor arrays. *Methods Enzymol* 423:414–431.
13. Shimizu TS, et al. (2000) Molecular model of a lattice of signalling proteins involved in bacterial chemotaxis. *Nat Cell Biol* 2:792–796.
14. Khursigara CM, Wu X, Zhang P, Lefman J, Subramaniam S (2008) Role of HAMP domains in chemotaxis signaling by bacterial chemoreceptors. *Proc Natl Acad Sci USA* 105:16555–16560.
15. Lefman J, et al. (2004) Three-dimensional electron microscopic imaging of membrane invaginations in *Escherichia coli* overproducing the chemotaxis receptor Tsr. *J Bacteriol* 186:5052–5061.
16. Weis RM, et al. (2003) Electron microscopic analysis of membrane assemblies formed by the bacterial chemotaxis receptor Tsr. *J Bacteriol* 185:3636–3643.
17. Zhang P, et al. (2004) Direct visualization of receptor arrays in frozen-hydrated sections and plunge-frozen specimens of *E. coli* engineered to overproduce the chemotaxis receptor Tsr. *J Microsc* 216:76–83.
18. Wolanin PM, Baker MD, Thomas DR, DeRosier DJ, Stock AM (2006) Self-assembly of receptor/signaling complexes in bacterial chemotaxis. *Proc Natl Acad Sci USA* 103:14313–14318.
19. Zhang P, Khursigara CM, Hartnell LM, Subramaniam S (2007) Direct visualization of *Escherichia coli* chemotaxis receptor arrays using cryo-electron microscopy. *Proc Natl Acad Sci USA* 104:3777–3781.
20. Park SY, et al. (2006) Reconstruction of the chemotaxis receptor-kinase assembly. *Nat Struct Mol Biol* 13:400–407.
21. Briegel A, et al. (2008) Location and architecture of the *Caulobacter crescentus* chemoreceptor array. *Mol Microbiol* 69:30–41.
22. Khursigara CM, Wu X, Subramaniam S (2008) Chemoreceptors in *Caulobacter crescentus*: trimers of receptor dimers in a partially ordered hexagonally packed array. *J Bacteriol* 190:6805–6810.
23. Porter SL, Wadhams GH, Armitage JP (2008) *Rhodobacter sphaeroides*: complexity in chemotactic signaling. *Trends Microbiol* 16:251–260.
24. Wadhams GH, et al. (2002) TlpC, a novel chemotaxis protein in *Rhodobacter sphaeroides*, localizes to a discrete region in the cytoplasm. *Mol Microbiol* 46:1211–1221.
25. Wadhams GH, Warren AV, Martin AC, Armitage JP (2003) Targeting of two signal transduction pathways to different regions of the bacterial cell. *Mol Microbiol* 50:763–770.
26. Hulko M, et al. (2006) The HAMP domain structure implies helix rotation in transmembrane signaling. *Cell* 126:929–940.
27. Aravind L, Ponting CP (1999) The cytoplasmic helical linker domain of receptor histidine kinase and methyl-accepting proteins is common to many prokaryotic signalling proteins. *FEBS Microbiol Lett* 176:111–116.
28. Duke TAJ, Bray D (1999) Heightened sensitivity of a lattice of membrane receptors. *Proc Natl Acad Sci USA* 96:10104–10108.
29. Sourjik V, Berg H (2002) Receptor sensitivity in bacterial chemotaxis. *Proc Natl Acad Sci USA* 99:123–127.
30. Li G, Weis RM (2000) Covalent modification regulates ligand binding to receptor complexes in the chemosensory system of *Escherichia coli*. *Cell* 100:357–365.
31. Sourjik V, Berg HC (2004) Functional interactions between receptors in bacterial chemotaxis. *Nature* 428:437–441.
32. Endres RG, Wingreen NS (2006) Precise adaptation in bacterial chemotaxis through "assistance neighborhoods." *Proc Natl Acad Sci USA* 103:13040–13044.
33. Li M, Hazelbauer GL (2005) Adaptational assistance in clusters of bacterial chemoreceptors. *Mol Microbiol* 56:1617–1626.
34. Butler SM, Camilli A (2004) Both chemotaxis and net motility greatly influence the infectivity of *Vibrio cholerae*. *Proc Natl Acad Sci USA* 101:5018–5023.
35. Miller LD, Yost CK, Hynes MF, Alexandre G (2007) The major chemotaxis gene cluster of *Rhizobium leguminosarum* bv. viciae is essential for competitive nodulation. *Mol Microbiol* 63:348–362.
36. Eisenbach M, Adler J (1981) Bacterial cell envelopes with functional flagella. *J Biol Chem* 256:8807–8814.
37. Iancu CV, et al. (2007) Electron cryotomography sample preparation using the Vitrobot. *Nat Protoc* 1:2813–2819.
38. Mastronarde DA (1997) Dual-axis tomography: an approach with alignment methods that preserve resolution. *J Struct Biol* 120:343–352.
39. Hegerl R (1996) The EM program package: a platform for image processing in biological electron microscopy. *J Struct Biol* 116:30–34.
40. Ulrich LE, Zhulin IB (2007) MiST: a microbial signal transduction database. *Nucleic Acids Res* 35:D386–D390.
41. Besemer J, Borodovsky M (2005) GeneMark: web software for gene finding in prokaryotes, eukaryotes and viruses. *Nucleic Acids Res* 33:W451–W454.
42. Finn RD, et al. (2008). The Pfam protein families database. *Nucleic Acids Res* 36:D281–D2288.
43. Eddy SR (1998) Profile hidden Markov models. *Bioinformatics* 14:755–763.
44. Wuichet K, Alexander RP, Zhulin IB (2007) Comparative genomic and protein sequence analyses of a complex system controlling bacterial chemotaxis. *Methods Enzymol* 422:1–31.

APPENDIX B

The EMBO Journal (2011), 1–10 | © 2011 European Molecular Biology Organization | All Rights Reserved 0261-4189/11
www.embojournal.org

THE EMBO JOURNAL

Structural diversity of bacterial flagellar motors

Songye Chen[1,6], Morgan Beeby[1,2,6], Gavin E Murphy[1,7], Jared R Leadbetter[3], David R Hendrixson[4], Ariane Briegel[1,2], Zhuo Li[1,2,8], Jian Shi[1,2], Elitza I Tocheva[1], Axel Müller[5], Megan J Dobro[1] and Grant J Jensen[1,2,*]

[1]Division of Biology, California Institute of Technology, Pasadena, CA, USA, [2]Howard Hughes Medical Institute, California Institute of Technology, Pasadena, CA, USA, [3]Division of Environmental Science and Engineering, California Institute of Technology, Pasadena, CA, USA, [4]Department of Microbiology, University of Texas Southwestern Medical Center, Dallas, TX, USA and [5]Division of Chemistry, California Institute of Technology, Pasadena, CA, USA

The bacterial flagellum is one of nature's most amazing and well-studied nanomachines. Its cell-wall-anchored motor uses chemical energy to rotate a microns-long filament and propel the bacterium towards nutrients and away from toxins. While much is known about flagellar motors from certain model organisms, their diversity across the bacterial kingdom is less well characterized, allowing the occasional misrepresentation of the motor as an invariant, ideal machine. Here, we present an electron cryotomographical survey of flagellar motor architectures throughout the Bacteria. While a conserved structural core was observed in all 11 bacteria imaged, surprisingly novel and divergent structures as well as different symmetries were observed surrounding the core. Correlating the motor structures with the presence and absence of particular motor genes in each organism suggested the locations of five proteins involved in the export apparatus including FliI, whose position below the C-ring was confirmed by imaging a deletion strain. The combination of conserved and specially-adapted structures seen here sheds light on how this complex protein nanomachine has evolved to meet the needs of different species.

The EMBO Journal advance online publication, 14 June 2011; doi:10.1038/emboj.2011.186
Subject Categories: microbiology & pathogens; structural biology
Keywords: bacterial flagellar motor; electron cryotomography; motility; phylogenetic profiling; subtomogram average

*Corresponding author. Division of Biology, California Institute of Technology, 1200 E. California Blvd, MC114-96, Pasadena, CA 91125, USA. Tel.: +1 626 395 8827; Fax: +1 626 395 5730;
E-mail: Jensen@caltech.edu
[6]These authors contributed equally to this work
[7]Present address: Laboratory of Cell Biology, Center for Cancer Research, National Cancer Institute, National Institutes of Health, Bethesda, MD 20892, USA
[8]Present address: Molecular and Cellular Biology Department, City of Hope Beckman Research Institute, Electron Microscopy Facility, Duarte, CA 91010, USA

Received: 20 December 2010; accepted: 17 May 2011

Introduction

The bacterial flagellum is a paradigm in modern molecular biology. Its structural complexity, multi-phasic and strictly regulated self-assembly, mechanical capabilities, functional interdependence with the chemosensory system, and both pathogenic and ecophysiological importance have made it central to studies and discussions in both the scientific and popular literature (Berg, 2003; McCarter, 2006; Pallen and Matzke, 2006; Chevance and Hughes, 2008; Minamino *et al*, 2008; Sowa and Berry, 2008; Snyder *et al*, 2009). The flagellum consists of a motor also known as the basal body, a flexible linker termed the hook, and a filament that behaves as a helical propeller and is typically many times the length of the bacterium itself. The motor converts ion flux across the cytoplasmic membrane into a torque that rotates the flagellum. In some organisms such as *Escherichia coli*, counter-clockwise rotation generates thrust that propels the cell forward. Signals from chemoreceptor arrays (Briegel *et al*, 2009) modulate the probability of the flagellar motor reversing direction (to spin clockwise) (Hazelbauer *et al*, 2008), which causes the bacterium to randomly re-orient. Thus, if a bacterium detects that it is swimming towards nutrients, the chemosensory system can prolong its movement in a specific direction.

Although all bacterial flagella share similarities in structure and mechanism, extensive variation in number, placement and usage exist between species. While cells such as *Vibrio cholerae* and *Caulobacter crescentus*, for example, exhibit a single polar flagellum, others, including *Salmonella enterica* and *E. coli* distribute several or many flagella around their periphery. Under different conditions, some bacteria alternate between polar and lateral flagellar systems (McCarter, 2004). The flagella of spirochaetes do not typically pierce the outer membrane, but instead remain in the periplasm where they rotate and/or contort the cell (Murphy *et al*, 2006; Liu *et al*, 2009; Kudryashev *et al*, 2010). Flagellar rotation is powered either by a proton-motive force (e.g., *E. coli*) or by a sodium-motive force (e.g., *V. cholerae*). The 'run and tumble' swimming mode that switches between clockwise and counter-clockwise rotations is best known, but other bacteria function differently, for example by varying the speed of a unidirectional motor. The molecular architectures of the helical flagellar filaments are also diverse (Galkin *et al*, 2008).

The flagellar motor is constructed from >20 proteins, and its basic morphology consists of an extended axial rod with coaxial rings termed the L-, P-, S-, M- and C-rings based on their locations relative to the cell. Previous analyses of flagellar motor genes have shown that they are widely distributed throughout and conserved across many bacterial lines of descent, but it has not been clear how observed sequence variations relate to the final structure of the macromolecular complex (Pallen *et al*, 2005; Liu and Ochman, 2007; Snyder *et al*, 2009). Structural studies of the motor to date have focussed on a small number of key organisms and have been hampered by the motor's size, complexity,

membrane localization and attachment to the cell envelope. These factors make motors difficult if not impossible to purify intact. X-ray crystallography has nevertheless revealed the structures of some of the isolated motor proteins, and complementary biochemical and genetic analyses have located many of them within the intact motor. Single-particle cryoEM studies have produced nanometre-resolution structures of the purified *S. enterica* motor, albeit without stators or the export apparatus (Thomas *et al*, 2006). In just the past few years, the development of electron cryotomography (ECT) has made it possible to image the structures of complete motors within intact cells in 3D to 'macromolecular' (several nanometres) resolution (Li and Jensen, 2009; Milne and Subramaniam, 2009). The first *in situ* structures have been from the thin spirochaetes *Treponema primitia* (Murphy *et al*, 2006) and *Borrelia burgdorferi* (Liu *et al*, 2009; Kudryashev *et al*, 2010). Those species demonstrated large peripheral structures not seen in the *S. enterica* single-particle reconstruction, hinting that the diversity of motor structures might be great.

Results and discussion

Data collected and overall appearance of the motors

We sought to sample the structural diversity of bacterial flagellar motors. To this end, we imaged the flagellar motors from 11 phylogenetically diverse bacteria chosen for their general interest as model organisms; involvement in animal host associations or free-living lifestyles, and suitability for ECT. The selected bacteria include those with polar (*C. crescentus* and *Campylobacter jejuni*), peritrichous (*S. enterica* and *E. coli*) and periplasmic (the spirochaetes *T. primitia* and *B. burgdorferi*) flagella. Bacteria employing Na-driven motors (*V. cholerae*) or 'sheathed' flagella (*V. cholerae* and *Helicobacter hepaticus*) were also included (see Supplementary Table S1 for comprehensive details on the phylogenetics and characteristics of each motor). Using high-throughput imaging methods (Suloway *et al*, 2009), for each species hundreds of cryotomograms of whole cells were collected. Subtomograms containing motors were computationally extracted from the data, mutually aligned, averaged and cylindrically symmetrized to obtain resolutions of a few nanometres (see Materials and methods).

While all the motors had clear similarities, their overall appearances were strikingly diverse (Figure 1). Comparison of the *S. enterica* structure with a previous single-particle cryoEM reconstruction (Thomas *et al*, 2006) exhibited similar features at similar positions along the rod and C-ring (Figure 2, left panel), cross-validating the two approaches, but the ECT reconstruction here also showed the position and curvature of the membranes and elements of the export apparatus, albeit at lower resolution. To highlight similarities among the motors, we generated a 'generic' motor by aligning and averaging the axial slices of all 11 structures. As shown in Figure 2 (right panel), the core structure of the rod, L-, P-, S-, M- and C-rings, and the export apparatus, as well as their relative locations with regard to the membranes are consistent across all motors. Because the C-rings of different species have different diameters, several C-rings appear in the generic average. This is in contrast with the other parts such as the rod, the LP- and MS-ring complexes and the export apparatus, whose boundaries remain sharp, indicating high structural conservation in their structures across species. Using these conserved features as landmarks, the densities present in the 11 independent motor reconstructions were carefully compared with those in the generic and *S. enterica* structures and assigned to known structures where possible (Figure 3). To assist in this process and provide insight into the differences, we correlated our imaging results with genomic data for each organism, sequencing and annotating new genomes when necessary. Lists of orthologues of known flagellar proteins were hand-curated (see Supplementary Table S2) and novel, previously unrecognized flagellar motor gene products were sought using their co-occurrence with motor genes in operons.

Export apparatus

The MS-ring in the inner membrane serves as the starting point for motor assembly. As expected, homologues of the sole component protein of the MS-ring, FliF, are present in all genomes. The periplasmic S-ring is correspondingly clear in all the organisms, but the membrane-embedded M-ring is less distinct due to contrast matching with the membrane. Compared with the single-particle reconstruction of *S. enterica*, there are three major additional densities present in the ECT reconstructions below the MS-ring: a convex dome bulging into the cytoplasm immediately beneath the MS-ring, a torus 10 nm lower and a spherical density 10 nm below the torus (Figure 4, schematic). Based on their position, presence in the intact cells, and absence in the single-particle reconstruction, we hypothesized that these three additional densities correspond to the dedicated type III secretion system (T3SS) that exports the proteins that form the rod, hook and filament through the hollow inner bore of the assembling flagellum. This flagellar export apparatus typically consists of six transmembrane (FlhA, FlhB, FliO, FliP, FliQ and FliR) and three soluble (FliH, FliI and FliJ) proteins.

The transmembrane proteins must reside at least in part in the dome, as it appears to be the continuation of the cytoplasmic membrane across the motor. The bulging of the dome (most prominent in *E. coli*, *C. jejuni*, *B. burgdorferi*, *T. primitia* and *Acetonema longum*) may be necessary to accommodate the transmembrane proteins, as the circular area within the plane of the M-ring in single-particle reconstructions was judged insufficient (Suzuki *et al*, 2004). Both FlhA and FlhB possess C-terminal cytoplasmic domains at the end of long (~30 amino acid) linkers (Saijo-Hamano *et al*, 2004, 2010; Zarivach *et al*, 2008; Moore and Jia, 2010; Worrall *et al*, 2010). The torus immediately below the dome, therefore, likely corresponds to their cytoplasmic domains, and the weak density seen between the dome and the torus in some of the reconstructions (most notably *S. enterica*) to the

Figure 1 Flagellar motor structures obtained by ECT and subtomogram averaging. Left column: 20-nm thick central slices through tomograms of individual cells exhibiting flagellar motors, arranged in the same order as they appear on the phylogenetic tree shown in Supplementary Figure S2. Scale bar, 50 nm. Right column: Axial slices through average reconstructions of each motor. Scale bar, 10 nm. (Note that the motor structure of *T. primitia* was published previously; Murphy *et al*, 2006.)

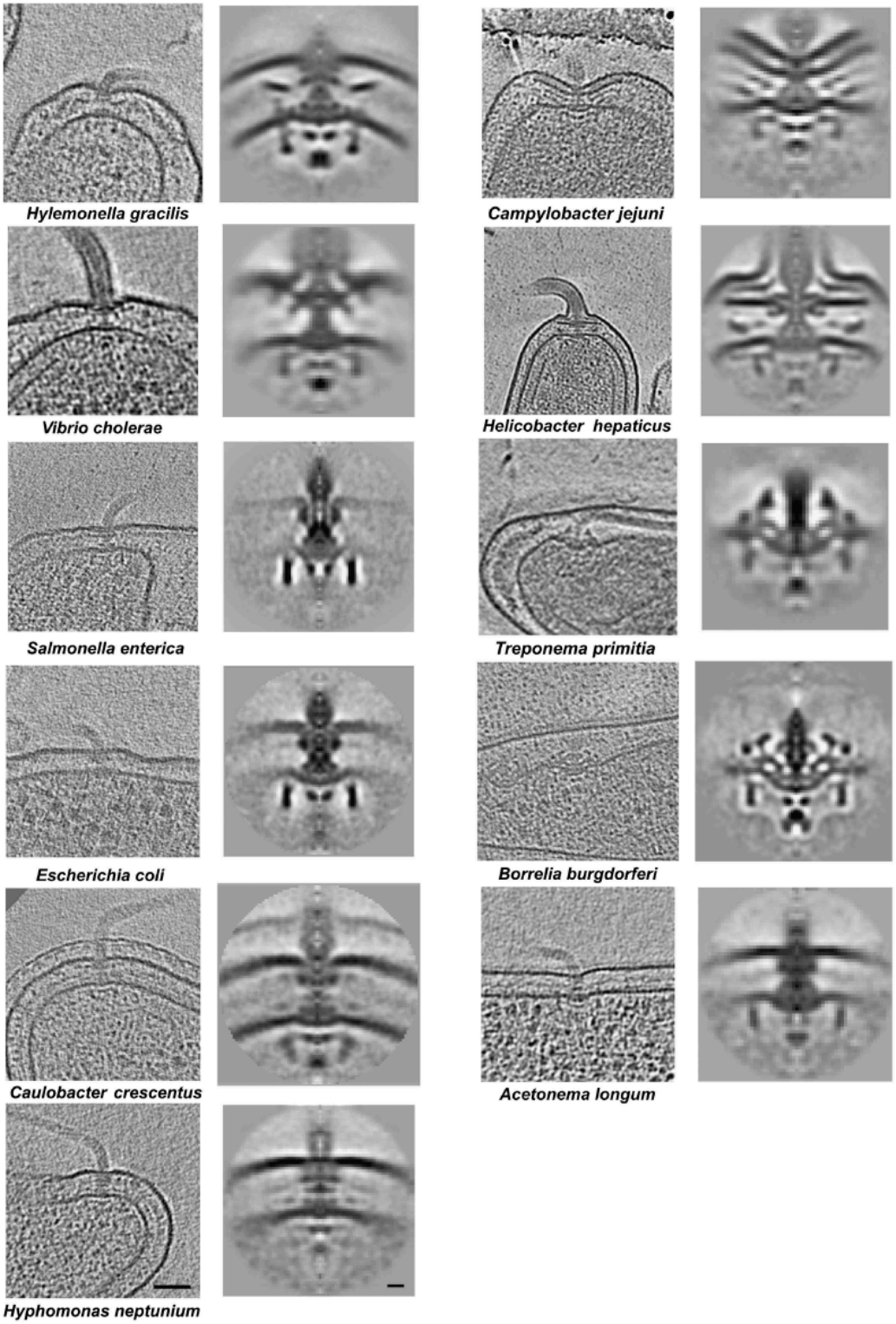

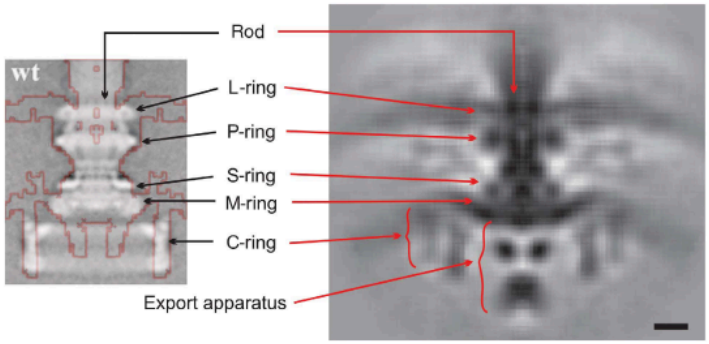

Figure 2 Structure of the common core and its comparison with an earlier cryoEM single-particle reconstruction. Left: Isosurface of the *S. enterica* motor obtained by ECT and subtomogram averaging (red line) superimposed on an earlier single-particle reconstruction of purified basal bodies from the same organism (grey levels) (Thomas *et al*, 2006). Right: A generic motor structure obtained by aligning and averaging the axial slices of all 11 motors reconstructed here. Scale bar, 10 nm.

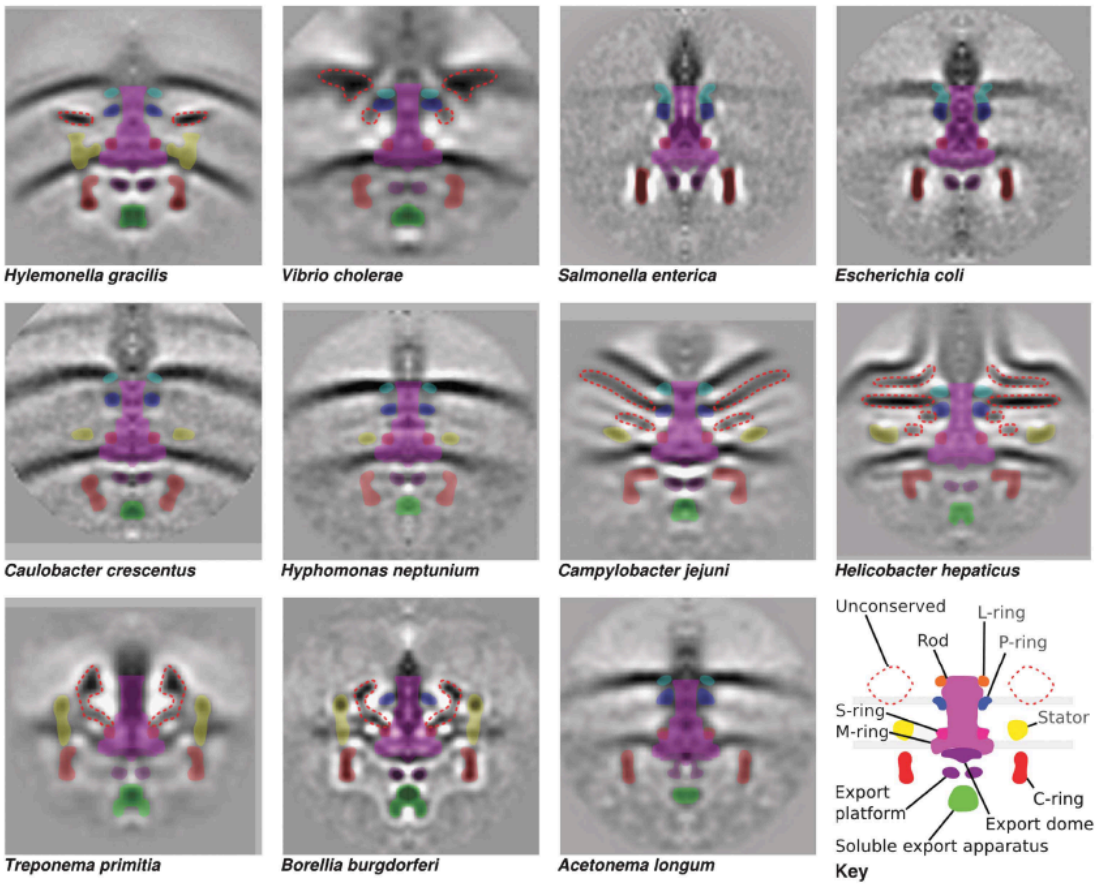

Figure 3 Assignment of densities. Manual segmentation of conserved (solid colours) and unconserved (dotted lines) motor components based on visual inspection. The conserved components from bottom to top are soluble export apparatus (FliH, FliI and FliJ); export platform and dome (FlhA, FlhB, FliO, FliP, FliQ and FliR); C-ring (FliG, FliM and FliN); MS-ring (FliF); stators (MotA and MotB in the H^+-dependent stators or PomA and PomB in the Na^+-dependent stators); rod (FliE, FlgB, FlgC, FlgF and FlgG); P-ring (FlgI); and L-ring (FlgH).

linkers. Together, the cytoplasmic domains of FlhA and FlhB have been referred to as the 'export platform', and may have been at least in part what was previously referred to as the 'C rod' in freeze-etch images (Katayama *et al*, 1996). Structures of homologues of these domains are available (Zarivach *et al*, 2008; Saijo-Hamano *et al*, 2010), and match

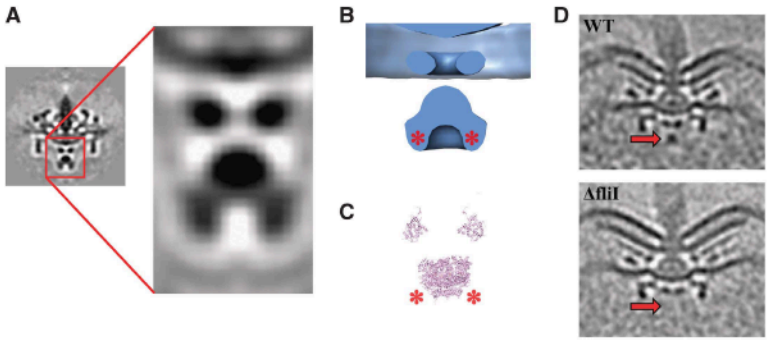

Figure 4 Structure of the export apparatus. (**A**) Enlarged view of the *B. burgdorferi* export apparatus and (**B**) 3D isosurface illustrating from top to bottom the export dome, torus and spherical density. (**C**) Atomic models of the cytoplasmic domains of FlhA above and the hexameric F1-ATPase, a homologue of FliI, shown at the same scale as (**B**) to show the correspondence of their sizes to the torus and spherical density. (**D**) Wild-type (top) and *ΔfliI* (bottom) *C. jejuni* motors confirming that the spherical density (red arrows, present above and absent below) is FliI.

the dimension of the torus reasonably well, though it remains unclear how they pack together or how many are required to complete the ring.

We reasoned that the spherical density below the torus likely corresponded to the ubiquitous ATPase FliI. FliI is thought to oligomerize into a roughly spherical cyclic hexamer ~9.5 nm in diameter (Claret *et al*, 2003), as illustrated by models based on the homologous F1-ATPase (Miwa and Yoshida, 1989) using crystal structures of FliI (Imada *et al*, 2007) or the FliI homologue EscN from the T3SS (Zarivach *et al*, 2007). This is in good agreement with the ~10 nm diameter seen for the spherical density in the reconstructions presented here (Imada *et al*, 2007; Zarivach *et al*, 2007). To test the hypothesis that this spherical density corresponds to FliI, we recorded cryotomograms of a *C. jejuni* strain lacking the *fliI* gene. *C. jejuni* was chosen for this test because it can be manipulated genetically and exhibits a clear density in this region. Despite the absence of *fliI*, the deletion strain produced sufficient motors for subtomogram averaging, consistent with a recent study in *Salmonella* (Paul *et al*, 2008), demonstrating that assembly can proceed without an absolute requirement for the export apparatus component FliI. The structure of the *fliI*-deletion strain was essentially identical to the wild type except for the spherical density, which was completely absent, confirming its identity (Figure 4D).

In addition to FliI, two other proteins (FliH and FliJ) are also probably part of the spherical density. FliH, a FliI regulator encoded in the genomes of all organisms but *Hyphomonas neptunium*, is known to bind FliI at its extreme N-terminus. If the FliI hexamer is oriented towards the membrane in the same way as its homologue, the F1-ATPase, as suggested in a recent study (Ibuki *et al*, 2011), the N-terminus of each FliI monomer will point towards the cytoplasm. The cytoplasmic-facing protuberances on the spherical density are, therefore, likely FliH (asterisks in Figure 4B). The poorly conserved FliJ has been shown to occupy the central pore of the FliI hexamer, and is structurally similar to the γ-subunit of the F1F0-ATPase (Ibuki *et al*, 2011). Although *fliJ* could not be detected in some organisms, its absence may be due to a difficulty in identifying the poorly conserved sequence.

The assignment of the torus as the cytoplasmic domains of FlhA and FlhB and the spherical density as the FliHIJ complex rationalize why in a recent tomographic study of detergent-treated *B. burgdorferi* cells, the torus but not the spherical density was visible (because the torus is covalently linked to the dome) (Liu *et al*, 2009). These assignments also explain why the spherical density is faint in the reconstructions of *S. enterica* and *E. coli* presented here: *S. enterica* and *E. coli* were included in the present survey because they are key model systems, but because both of them are too thick for high resolution ECT, these cells were gently lysed just before freezing (see Materials and methods), which would likely disrupt the localization of soluble proteins like FliI. The shape and prominence of the FliHIJ density in the average reconstructions may also be affected by the facts that FliI occurs as both a monomer and a hexamer and is also known to interact with the relatively distant C-ring, and may not therefore occupy a consistent location.

C-ring

Assembling around FliF (the MS-ring) and the export apparatus is the C-ring, which is involved in export, torque generation and directional switching. Accordingly, the C-ring is present in all 11 organisms and three C-ring structural genes, *fliG*, *fliM* and *fliN*, are conserved across all genomes. Considerable variation is evident, however, in the appearance and diameter of the C-rings, which range from 34 nm in *C. crescentus* to 57 nm in *T. primitia* (Figures 1 and 3). Consistent with the cryoEM single-particle reconstruction of the *S. enterica* motor (Thomas *et al*, 2006), all the three γ-proteobacteria *V. cholerae*, *S. enterica* and *E. coli* as well as the thin β-proteobacterium *Hylemonella gracilis* have similar cross-sections and diameters of ~40 nm. The C-rings from *H. neptunium* and *C. crescentus* (both α-proteobacteria) are less clear (suggesting incomplete occupancy or mobility) and exhibit a distinctive conical reduction in diameters from, for example in *C. crescentus*, 36 nm near the inner membrane to 26 nm at the tip near the FliHIJ complex. The average diameter of the C-rings in the pathogenic ε-proteobacteria *C. jejuni* and *H. hepaticus* is 49 nm, and these display stronger densities at the membrane-proximal side of the C-ring next to the export platform immediately beneath the MS-ring. It is known that the membrane-proximal part of the C-ring is composed of FliG (Thomas *et al*, 2006; Liu *et al*, 2009); and therefore, these stronger densities may represent

alternative, more stable, or higher occupancy conformations of FliG, or additional components of the motor exclusive to the ε-proteobacteria. The spirochaetes *B. burgdorferi* and *T. primitia* and the diderm firmicute *A. longum* possess C-rings with an even larger average diameter of 54 nm, but maintain the same cross-section as *S. enterica*. No correlation could be made between tomographic density and the presence of FliY, a FliN paralogue with an additional domain found in *A. longum*, *T. primitia*, *H. hepaticus*, *C. jejuni* and *S. enterica*.

Rod and L/P-rings

Assembling atop the S-ring is the rod, which acts as the central driveshaft through the cell envelope, transmitting torque applied to the MS-ring to the hook and filament. The rod is comprised of ubiquitous paralogous proteins that are known to form a proximal (FliE, FlgB, FlgC and FlgF) and a distal (FlgG) rod, but no new details about the arrangement of these proteins could be gleaned from the tomograms. The length of the rod was well conserved, as judged by the distinct densities seen in the generic average for the S- and P-rings and inner and outer membranes. The distance between the distal end of the S-ring and the centre of the outer membrane was 22 nm (measured in the generic average), confirming earlier measurements of the rod length on isolated flagellar hook-basal bodies (HBBs) from wild-type *S. enterica* (Takahashi *et al*, 2009).

The periplasmic P- and L-rings around the rod are thought to function as bushings through the peptidoglycan layer and lipopolysaccharide of the outer membrane, respectively. Because the rings coat the outside of the rod, both proteins (FlgH and FlgI) are exported into the periplasm via the Sec pathway instead of through the dedicated flagellar T3SS (Homma *et al*, 1987; Jones and Macnab, 1990). Unlike the rod proteins, however, it has previously been noted that the genes encoding the L/P-ring components are not ubiquitous, and the variation seen here calls into question the presumed roles of these proteins (Pallen *et al*, 2005). The reconstructions of *S. enterica*, *E. coli*, *H. neptunium*, *C. crescentus* and *A. longum* represent the 'standard' cases, where both the L- and P-ring genes are present, the P-ring is visible in the tomograms, and the L-ring is not, likely because it is embedded in the outer membrane. In *H. gracilis*, both genes are present, and two rings are visible underneath the outer membrane, suggesting that the L-ring may not be embedded in the membrane in this species, although it is not clear why this alternative arrangement is seen. In the sheathed flagella of *H. hepaticus* and *V. cholerae*, the outer membrane continues as a sheath around the flagellar hook and filament. The L-ring proteins in these two organisms presumably still form a complex with the P-ring, but the diverse structures in that region make assignments unclear. It is noteworthy that the *H. hepaticus* L-ring gene does not encode an otherwise ubiquitous cysteine residue in the vicinity of the amino terminus (Schoenhals and Macnab, 1996). This residue has been shown to be part of a signal peptide II cleavage consensus motif that is subsequently lipoylated. The situation is further complicated by the fact that this cysteine residue is nevertheless retained in the other organism with a sheathed flagellum, *V. cholerae*. In the spirochaetes *B. burgdorferi* and *T. primitia*, the L-ring protein FlgH is absent, as is thought due to the fact that the flagellar filaments in these organisms never cross the outer membrane (Pallen *et al*, 2005), but remain within the periplasm. The P-ring protein FlgI is absent only in the genome of *T. primitia*. This was first observed by tomography in a recent study of a *B. burgforferi* FlgI mutant, in which a density around the rod was absent (Liu *et al*, 2009). Here, we observe a similar absence of ring density on the rod of *T. primitia*, corresponding to FlgI. It is noteworthy that FlgI in the spirochaetes is distant from the peptidoglycan layer, at odds with its supposed function. FlgI is also found in the Leptospiraceae, another family within the spirochaete class, so it may have a special alternative function in the spirochaetes (Chevance *et al*, 2007).

Stator complex

Above the C-ring and surrounding the MS-ring in the inner membrane are stator complexes that are thought to extend towards and bind to the peptidoglycan layer. Through interactions with the C-ring proteins, the stators transform the flow of H^+ or Na^+ ions across the membrane into torque to drive the motor. Each stator complex is composed of two proteins, MotA and MotB in the H^+-dependent stators (e.g., *E. coli*), or PomA and PomB in the Na^+-dependent stators (e.g., *V. cholerae*), with an apparent 4:2 stoichiometry. In our averaged structures, we see distinctive rod-shaped stator ring structures above the inner membrane with connections on the other side of the membrane to the C-ring in the β-proteobacterium *H. gracilis* and the spirochaetes *B. burgdorferi* and *T. primitia*. As previously shown elsewhere (Murphy *et al*, 2006; Liu *et al*, 2009; Kudryashev *et al*, 2010) and reproduced in Figure 5, 16 copies of the stator complexes are clearly seen in the averaged tomograms of the spirochaetes *B. burgdorferi* and *T. primitia* even before rotational averaging. In contrast, the symmetry observed in the *H. gracilis* stator ring is 13 (Figure 5). In the α-proteobacteria (*H. neptunium* and *C. crescentus*), stator densities are visible, but they are less prominent and their symmetries could not be discerned. In the ε-proteobacteria *C. jejuni* and *H. hepaticus*, stator densities are clear, but they have a different shape in cross-section, lie nearly parallel to the cytoplasmic membrane, and extend further into the periplasm. The reason that the symmetry of these motors could not be discerned may be that the stator system is highly dynamic with rapid turnover of subunits (Leake *et al*, 2006) and perhaps variable conformations, causing low occupancy and heterogeneity. These cells also have single, polar flagella, and so because the rod-shaped cells freeze lying flat on the grid, no direct 'top' views of the motor were obtained, which makes detecting rotational symmetries more difficult. The rest of the species may not exhibit clear stator density because the periplasmic domains of the stator complex (MotA/B or PomA/B) are thin, as shown in cryoEM images of purified PomA/B in liposomes (Yonekura *et al*, 2006).

Unconserved densities

In addition to this somewhat conserved structural core, many of the organisms exhibited additional, presumably proteinaceous densities that are likely to be unrecognized, novel components of the motor. The most striking is the spirochaetes' large 'P-collar' that forms a bowl-like structure around the rod within the stator ring, and which has been postulated to stabilize the motor (Murphy *et al*, 2006). To generate hypotheses about which proteins form the P-collar, we

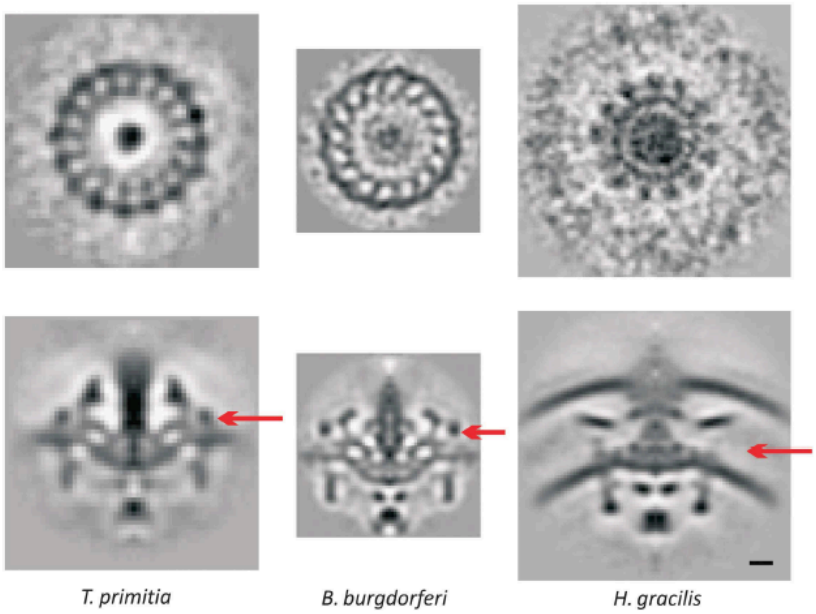

Figure 5 Symmetries in the stator region. Upper row: Radial slices through the stator regions of three average motors before rotational averaging showing 16-, 16- and 13-fold symmetry, respectively. Lower row: Axial slices through the averaged and symmetrized motors with arrows showing the height at which the radial slices were taken. Scale bar, 10 nm.

exploited the fact that genes encoding proteins involved in stable complexes are frequently encoded in genomic proximity to one-another (Huynen *et al*, 2000). Furthermore, as the protein is not a component of the cylindrical core of the rod, hook or filament, we assumed its secretion would be via the Sec pathway as opposed to the dedicated flagellar T3SS. Using these criteria (see Materials and methods), we narrowed our search to a candidate gene for involvement in the P-collar, flbB, first identified in a comprehensive study of *B. burgdorferi* flagellar genetics (Ge *et al*, 1997). This gene is consistently near other flagellar motor genes in spirochaetes and includes the appropriate periplasmic export signal.

While the L/P-ring complex simply surrounds the rod as it passes through the lipopolysaccharide membrane and peptidoglycan layer in the well-studied flagellar motors, in *V. cholerae* it appears to serve as a foundation for two additional structures. *V. cholerae* possesses two proteins, MotX and MotY, which form a so-called T-ring that is thought to assist in the formation and binding of the MotA/MotB stators (Terashima *et al*, 2006). Here, this T-ring can be seen lower and to the outside of the P-ring, to which it is connected. There is also a substantial increase in density near the presumed position of the L-ring. Hosogi *et al* (2011) recently described this entire density in the closely related *Vibrio alginolyticus* HBB as the L-ring. Based on the fact that the L-ring-encoding *flgH* gene is ~360 amino acids long in both *S. enterica* and *V. cholerae*, we propose that the unusually large and oddly shaped ring structure must also include an additional, as-yet unidentified protein.

The L/P-ring complex also appears to serve as a structural anchor in the ε-proteobacteria *C. jejuni* and *H. hepaticus*. Here, the L/P-ring complex is attached to large periplasmic basal disks. In *C. jejuni*, an extensive disk-like density is found in the periplasm immediately below and parallel to the outer membrane around the rod and above the stators. This disk connects to the P-ring and has an outer radius of 48 ± 9 nm, calculated from the edge of the rod along the disk. A second disk with a radius of 32 ± 7 nm sits beneath the first and seems to be faintly connected to the M/S-ring. In *H. hepaticus*, a similarly extensive (32 ± 2 nm in radius) but flat disk is found between what are probably enhanced L- and P-rings. A similarly large disk (85 nm average radius) connected to the L/P-ring complex was observed previously by EM of negatively stained flagellar motors purified from another ε-proteobacterium, *Wolinella succinogenes*, which is closely related to *C. jejuni* and *H. hepaticus* (Engelhardt *et al*, 1993). While all three of these large basal disks are likely composed of homologous proteins, bioinformatic analyses yielded no candidate proteins for this structure, likely unaided by the well-discussed genomic fragmentation and lack of synteny within the ε-proteobacteria (Eppinger *et al*, 2004).

It is interesting to note that the β-proteobacterium *H. gracilis* also exhibited a periplasmic disk above the stators, but the relationship of this disk to the larger ε-proteobacterial basal disks is unclear. The *H. gracilis* disk is at the same height as the P-ring but does not connect, exhibiting an inner and outer radius of 18 ± 2 and 31 ± 2 nm, respectively. Previously, similar disks have been observed in another β-proteobacterium, *Aquaspirillum serpens* (Coulton and Murray, 1978). The function of these disks remains unclear, as their occurrence does not seem to correlate with any obvious phenotype (such as sheathed flagella) or habitat (such as viscous environment), besides that they are so far exclusive to (but not

required for) polar flagella. Based on their position, they may stabilize the stators to sustain larger torques.

Above the basal disk and immediately below the highly curved bend in the outer membrane of the sheathed *H. hepaticus* is yet another disk-like density. As mentioned above, in the other sheathed bacterium, *V. cholerae*, the L-ring is unusually large and odd-shaped. These structures may stabilize the outer membrane and the sheath against the rotation of the flagellum. Finally, two previous studies of negatively stained, purified *C. crescentus* motors gave conflicting reports about whether or not a so-called E-ring existed between the M/S- and L/P-ring complexes (Stallmeyer *et al*, 1989; Kanbe *et al*, 2005). It remains unclear whether there are additional rings here in the *C. crescentus* and *H. neptunium* reconstructions.

Conclusion

In summary, three-dimensional structures of 11 phylogenetically diverse bacterial flagellar motors were obtained *in situ* at a few nanometre resolutions via ECT and subtomogram averaging. The positions of key proteins of the export apparatus were determined. While the motors all exhibited a common core built from the products of conserved flagellar genes, their overall appearances were strikingly different due to variations in the structure of that core and the presence of unique peripheral densities, showing that each is a related but specially adapted nanomachine.

Materials and methods

Culture conditions

C. crescentus CB15N, *E. coli* RP437 and MG1655, *V. cholerae* TRH7000, *H. hepaticus* (ATCC 51449), *C. jejuni* (ATCC 29428), *B. burgdorferi* B31 (ATCC 35210), *A. longum* APO-1 DSM 6540 and *T. primitia* strain ZAS-2 cells were grown as described previously (Murphy *et al*, 2006; Briegel *et al*, 2009).

H. neptunium (ATCC 15444) was grown in 2216 marine broth (Difco) at 30°C for 24–48 h. The cell culture was incubated on ice during plunge freezing.

S. enterica subsp. enterica serovar Typhimurium str. LT2 was grown in LB plus 0.3 M sucrose and up to 10 mM $MgSO_4$. Penicillin (466 IU/ml) was added 15 and 60 min before plunge freezing.

H. gracilis was cultivated from a rotten lily taken from a Caltech pond by placing a drop of liquid upon a 0.22-μm filter resting atop agar containing 10 mM MOPS pH 7.0, 0.5 g tryptone and 0.5 g yeast extract per litre. Colonies appeared several weeks later. The 16S rRNA was sequenced from a liquid culture and found to be identical to the type strain of *H. gracilis*. Cultures were grown in the above media without MOPS for 2 days and only reached an OD of 0.05. The cells were checked for motility with a light microscope. The cells were then centrifuged and concentrated 10-fold in the same media for plunge freezing onto the EM grids (Murphy, 2007).

Genome sequencing

H. gracilis (ATCC 19624) cultures were obtained from the ATCC and cultured in liquid and agar media containing 5 g peptone, 0.5 g yeast extract, 0.02 g Tween-80 and 0.1 g K_2HPO_4 made up to 1 l with nanopure water with optional addition of 15 g agar. Colonies were initially grown on agar plates and subsequently used to inoculate liquid cultures. The identity of the cultures was confirmed by PCR amplification and sequencing of 16S rRNA. DNA was purified from 2 l cultures by lysing cells with lysozyme followed by consecutive RnaseA, proteinase K, SDS, sodium acetate and chloroform/phenol mixture additions. DNA was washed with ethanol and dried. A paired-end genomic DNA library was prepared from this sample and 76 bp reads generated using Illumina sequencing at Caltech's Millard & Muriel Jacobs Genetics & Genomics Laboratory (http://mmjggl.caltech.edu/sequencing/). Reads were truncated to 67 bp and assembled using Velvet (Zerbino and Birney, 2008). Using a kmer size of 49, 3.6 Mb of sequence data was generated and distributed over 152 contigs with an n_{50} of 75 kb and a maximum contig length of 192 kb. This partially assembled genome was annotated for ORFs using the NCBI PGAAP service and flagellar genes semi-automatically annotated using reciprocal best-hit methodology and manual curation. This Whole Genome Shotgun project has been deposited at DDBJ/EMBL/GenBank under the accession AEGR00000000. The version described in this paper is the first version, AEGR01000000.

The genome sequencing of *A. longum* APO-1 was performed at Stanford in the laboratory facility of Stephen Quake and will be described elsewhere. This Whole Genome Shotgun project has been deposited at DDBJ/EMBL/GenBank under the accession AFGF00000000. The version described in this paper is the first version, AFGF01000000. Genome sequencing results for *T. primitia* ZAS-2 will be described elsewhere; the closed sequence for this strain has been deposited into GenBank as CP001843.

EM sample preparation, data collection and tomogram reconstruction

EM R2/2 copper/rhodium Quantifoil or lacy carbon grids were glow discharged and coated with a 3 ×-concentrated solution of 10 nm colloidal gold particles (Ted Pella). A 5 × -concentrated solution of 10 nm colloidal gold was also added to the cells immediately before plunge freezing. A 4-μl droplet of the sample solution was applied to the EM grid, then blotted and plunge frozen into liquid ethane (Dubochet *et al*, 1988) or into a liquid ethane–propane mixture (Tivol *et al*, 2008) using a Vitrobot (FEI Company) (Iancu *et al*, 2006) or in-house plunger. To flatten the thickest cell types, *E. coli* and *S. enterica* cells were incubated with 466 IU/ml penicillin G for up to 60 min at 30°C (Eisenbach and Adler, 1981), which caused some cells to rupture when blotted just before plunge freezing. The grids were stored under liquid nitrogen until data collection.

EM images were collected using a Polara 300-kV FEG transmission electron microscope (FEI Company) equipped with an energy filter (slit width 20 eV; Gatan) on a 2k × 2k Ultrascan CCD camera or, later, a lens-coupled 4k × 4k UltraCam (Gatan). Typically, tilt series were recorded from −60° to 60° with an increment of 1° semi-automatically around 1 or 2 axes (Iancu *et al*, 2005) at 8–12 μm under-focus using the predictive UCSF-Tomo package (Zheng *et al*, 2007) or Leginon (Suloway *et al*, 2009). Cumulative doses of up to 200 $e^-/Å^2$ were used.

Image tilt series were generally binned by two (in X and Y) and 3D tomograms were calculated automatically by Raptor (Amat *et al*, 2008) using the Peach distributed computing system (Leong *et al*, 2005). In cases where Raptor was not available or failed, the semi-automatic IMOD software package (Mastronarde, 1997) was used. No digital filters were used to reduce noise. Image tilt series and final reconstructions were deposited into an in-house web-based database. For a more detailed protocol, see Chen *et al* (2010).

Subtomogram extraction, alignment, averaging and symmetrization

Bsoft (Heymann *et al*, 2008) and the Peach (Leong *et al*, 2005) distributed computing system were used for iterative subtomogram extraction, alignment, averaging and symmetrization. For *V. cholerae*, *H. neptunium* and *A. longum*, tomograms of different magnifications were used, and the tomograms of higher magnification were re-sampled to match the pixel size of the tomograms of lowest magnification. The positions of flagellar motors in the tomograms were marked by eye at the entry point of the flagellar filament into the outer membrane. For alignment, subtomograms centred on the motors were extracted, bandpass filtered between 200 nm and the first CTF zero and masked in reciprocal space within the missing wedge. Rotational alignments were done with 3° step sizes, as no further improvement was seen with finer steps. Subtomograms containing flagellar motors were first extracted by hand and aligned to a reference arbitrarily chosen from the data sets. The aligned motors were then averaged, and the average was rotated so that the rod axis coincided with the *z*-axis. This result was cylindrically symmetrized around the *z*-axis. Subtomograms were computationally re-extracted based on the previous alignment result, realigned to the symmetrized average motor, re-averaged and symmetrized. The whole process was iterated until the coordinates of motors stabilized. Average motors were checked computationally for symmetry about the rod before applying any symmetry. In the cases of the spirochaetes and *H. gracilis*, where

symmetry was detected in the stator rings, the average reconstruction was symmetrized accordingly (16- and 13-fold, respectively). In all other cases, 16-fold symmetry was applied simply to improve the signal-to-noise ratio of the final motor structure. Note the cylindrical symmetrization does not affect the axial structures obtained as shown in Figure 1. All the symmetrized average motor structures have been deposited into the EMDataBank.

Tomograms were inspected and measured with IMOD (Mastronarde, 1997). 2D image thresholding and superposition was done with Adobe Photoshop (Adobe Systems Inc.). The resolution was estimated by separately averaging and symmetrizing two halves of the data set and correlating them using Fourier shell correlation with a threshold of 0.5 (Supplementary Figure S1).

Identification of FliI location

Starting with wild-type *Campylobacter jejuni* 81-176 Sm^R (DRH212) containing an *rpsL* allele conferring streptomycin resistance (Hendrixson *et al*, 2001), strain DRH2257 was constructed through in-frame deletions of *fliI* and marker gene *astA* (the enzyme arylsulphatase), which does not affect flagellar biosynthesis or motility (Joslin and Hendrixson, 2009). DRH212 and DRH2257 were grown on MH agar under microaerophilic conditions for 3 days, re-streaked and grown overnight. Colonies were resuspended in MH broth, plunge frozen and imaged as described above except that images were collected at −15 μm defocus. Subtomographic averages were generated from 21 wild-type and 19 Δ*fliI* motors, respectively, using PEET from the IMOD suite of programs without symmetrization (Mastronarde, 1997).

Bioinformatics analysis

To define orthologous gene families, flagellar structural protein genes were initially grouped according to the KEGG Orthology (KO) Database (Kanehisa *et al*, 2010). Family assignments were verified and/or revised by extensive literature searches and manual BLASTing to confirm the automated KO assignments. For those genomes not covered by the KO Database, genes were assigned to orthologous gene families by BLAST reciprocal best-hit methods against the previously curated family allocations. Non-flagellar gene family assignments were made automatically using the KO Database without further manual curation.

To predict functional linkages between known flagellar genes and novel genes, the mutual information score was calculated between operon occurrence vectors of each orthologous gene family using a previously described operon prediction method (Overbeek *et al*, 1999). An operon occurrence vector describes in which operons a given orthologous gene family resides: that is, for each orthologous family, a binary vector is assigned of dimension equal to the number of operons in the combined sequenced genomes used for this analysis. Thus, each gene family's operon occurrence vector will be predominantly '0', with occasionally a '1' for those operons in which that family occurs. For each defined novel substructure observed by tomography (e.g., the P-collar), the subset of organisms in which it is found were noted, and the mutual information between all gene families exclusive to that subset was calculated. Orthologous families predicted to be functionally linked to known flagellar genes by a high mutual information score were further filtered for periplasmic export sequences using SignalP (Emanuelsson *et al*, 2007).

Supplementary data

Supplementary data are available at *The EMBO Journal* Online (http://www.embojournal.org).

Acknowledgements

We thank Drs Jane H Ding and Alasdair McDowall for computational and EM support, respectively; Sarkis K Mazmanian for use of the microaerobic chamber; and Igor Antoshechkin for advice on genome assembly. This work was supported by the Howard Hughes Medical Institute, the Gordon and Betty Moore Foundation Cell Center and the National Science Foundation.

Author contributions: GJJ designed the research; SC, MB, GEM, AB, ZL, JS, EIT, AM, JRL and MJD cultured cells and/or collected tomograms; SC averaged subtomograms with help from GEM; JRL and MB coordinated the sequencing and annotation of needed genomes, MB performed bioinformatics, and together with DRH identified export densities, including subtomogram averaging of the comparative wild-type and mutant *C. jejuni* motors; SC, MB and GJJ analysed the results and wrote the paper.

Conflict of interest

The authors declare that they have no conflict of interest.

References

Amat F, Moussavi F, Comolli LR, Elidan G, Downing KH, Horowitz M (2008) Markov random field based automatic image alignment for electron tomography. *J Struct Biol* **161**: 260–275

Berg HC (2003) The rotary motor of bacterial flagella. *Annu Rev Biochem* **72**: 19–54

Briegel A, Ortega DR, Tocheva EI, Wuichet K, Li Z, Chen SY, Muller A, Iancu CV, Murphy GE, Dobro MJ, Zhulin IB, Jensen GJ (2009) Universal architecture of bacterial chemoreceptor arrays. *Proc Natl Acad Sci USA* **106**: 17181–17186

Chen S, McDowall A, Dobro MJ, Briegel A, Ladinsky M, Shi J, Tocheva EI, Beeby M, Pilhofer M, Ding HJ, Li Z, Gan L, Morris DM, Jensen GJ (2010) Electron cryotomography of bacterial cells. *J Vis Exp* **39**; doi:10.3791/1943, http://www.jove.com/details.stp?id=1943

Chevance FFV, Hughes KT (2008) Coordinating assembly of a bacterial macromolecular machine. *Nat Rev Microbiol* **6**: 455–465

Chevance FFV, Takahashi N, Karlinsey JE, Gnerer J, Hirano T, Samudrala R, Aizawa SI, Hughes KT (2007) The mechanism of outer membrane penetration by the eubacterial flagellum and implications for spirochete evolution. *Genes Dev* **21**: 2326–2335

Claret L, Calder SR, Higgins M, Hughes C (2003) Oligomerization and activation of the FliI ATPase central to bacterial flagellum assembly. *Mol Microbiol* **48**: 1349–1355

Coulton JW, Murray RGE (1978) Cell envelope associations of Aquaspirillum Serpens flagella. *J Bacteriol* **136**: 1037–1049

Dubochet J, Adrian M, Chang JJ, Homo JC, Lepault J, McDowall AW, Schultz P (1988) Cryo-Electron Microscopy of vitrified specimens. *Q Rev Biophys* **21**: 129–228

Eisenbach M, Adler J (1981) Bacterial-cell envelopes with functional flagella. *J Biol Chem* **256**: 8807–8814

Emanuelsson O, Brunak S, von Heijne G, Nielsen H (2007) Locating proteins in the cell using TargetP, SignalP and related tools. *Nat Protoc* **2**: 953–971

Engelhardt H, Schuster SC, Baeuerlein E (1993) An archimedian spiral—the basal disk of the Wolinella Flagellar Motor. *Science* **262**: 1046–1048

Eppinger M, Baar C, Raddatz G, Huson DH, Schuster SC (2004) Comparative analysis of four Campylobacterales. *Nat Rev Microbiol* **2**: 872–885

Galkin VE, Yu X, Bielnicki J, Heuser J, Ewing CP, Guerry P, Egelman EH (2008) Divergence of quaternary structures among bacterial flagellar filaments. *Science* **320**: 382–385

Ge Y, Old IG, Saint Girons I, Charon NW (1997) Molecular characterization of a large Borrelia burgdorferi motility operon which is initiated by a consensus sigma70 promoter. *J Bacteriol* **179**: 2289–2299

Hazelbauer GL, Falke JJ, Parkinson JS (2008) Bacterial chemoreceptors: high-performance signaling in networked arrays. *Trends Biochem Sci* **33**: 9–19

Hendrixson DR, Akerley BJ, DiRita VJ (2001) Transposon mutagenesis of Campylobacter jejuni identifies a bipartite energy taxis system required for motility. *Mol Microbiol* **40**: 214–224

Heymann JB, Cardone G, Winkler DC, Steven AC (2008) Computational resources for cryo-electron tomography in Bsoft. *J Struct Biol* **161**: 232–242

Homma M, Komeda Y, Iino T, Macnab RM (1987) The flaFIX gene product of Salmonella typhimurium is a flagellar basal body component with a signal peptide for export. *J Bacteriol* **169**: 1493–1498

Hosogi N, Shigematsu H, Terashima H, Homma M, Nagayama K (2011) Zernike phase contrast cryo-electron tomography of sodium-driven flagellar hook-basal bodies from Vibrio alginolyticus. *J Struct Biol* **173:** 67–76

Huynen M, Snel B, Lathe W, Bork P (2000) Predicting protein function by genomic context: quantitative evaluation and qualitative inferences. *Genome Res* **10:** 1204–1210

Iancu CV, Tivol WF, Schooler JB, Dias DP, Henderson GP, Murphy GE, Wright ER, Li Z, Yu Z, Briegel A, Gan L, He Y, Jensen GJ (2006) Electron cryotomography sample preparation using the Vitrobot. *Nat Protoc* **1:** 2813–2819

Iancu CV, Wright ER, Benjamin J, Tivol WF, Dias DP, Murphy GE, Morrison RC, Heymann JB, Jensen GJ (2005) A 'flip-flop' rotation stage for routine dual-axis electron cryotomography. *J Struct Biol* **151:** 288–297

Ibuki T, Imada K, Minamino T, Kato T, Miyata T, Namba K (2011) Common architecture of the flagellar type III protein export apparatus and F- and V-type ATPases. *Nat Struct Mol Biol* **18:** 277–282

Imada K, Minamino T, Tahara A, Namba K (2007) Structural similarity between the flagellar type III ATPase FliI and F-1-ATPase subunits. *Proc Natl Acad Sci USA* **104:** 485–490

Jones CJ, Macnab RM (1990) Flagellar assembly in Salmonella typhimurium: analysis with temperature-sensitive mutants. *J Bacteriol* **172:** 1327–1339

Joslin SN, Hendrixson DR (2009) Activation of the Campylobacter jejuni FlgSR two-component system is linked to the flagellar export apparatus. *J Bacteriol* **191:** 2656–2667

Kanbe M, Shibata S, Umino Y, Jenal U, Aizawa SI (2005) Protease susceptibility of the Caulobacter crescentus flagellar hook-basal body: a possible mechanism of flagellar ejection during cell differentiation. *Microbiology* **151:** 433–438

Kanehisa M, Goto S, Furumichi M, Tanabe M, Hirakawa M (2010) KEGG for representation and analysis of molecular networks involving diseases and drugs. *Nucleic Acids Res* **38:** D355–D360

Katayama E, Shiraishi T, Oosawa K, Baba N, Aizawa S (1996) Geometry of the flagellar motor in the cytoplasmic membrane of Salmonella typhimurium as determined by stereo-photogrammetry of quick-freeze deep-etch replica images. *J Mol Biol* **255:** 458–475

Kudryashev M, Cyrklaff M, Wallich R, Baumeister W, Frischknecht F (2010) Distinct *in situ* structures of the Borrelia flagellar motor. *J Struct Biol* **169:** 54–61

Leake MC, Chandler JH, Wadhams GH, Bai F, Berry RM, Armitage JP (2006) Stoichiometry and turnover in single, functioning membrane protein complexes. *Nature* **443:** 355–358

Leong PA, Heymann JB, Jensen GJ (2005) Peach: a simple Perl-based system for distributed computation and its application to cryo-EM data processing—Ways & means. *Structure* **13:** 505–511

Li Z, Jensen GJ (2009) Electron cryotomography: a new view into microbial ultrastructure. *Curr Opin Microbiol* **12:** 333–340

Liu J, Lin T, Botkin DJ, McCrum E, Winkler H, Norris SJ (2009) Intact flagellar motor of Borrelia burgdorferi revealed by cryo-electron tomography: evidence for stator ring curvature and rotor/C-ring assembly flexion. *J Bacteriol* **191:** 5026–5036

Liu RY, Ochman H (2007) Stepwise formation of the bacterial flagellar system. *Proc Natl Acad Sci USA* **104:** 7116–7121

Mastronarde DN (1997) Dual-axis tomography: an approach with alignment methods that preserve resolution. *J Struct Biol* **120:** 343–352

McCarter LL (2004) Dual flagellar systems enable motility under different circumstances. *J Mol Microbiol Biotechnol* **7:** 18–29

McCarter LL (2006) Regulation of flagella. *Curr Opin Microbiol* **9:** 180–186

Milne JLS, Subramaniam S (2009) Cryo-electron tomography of bacteria: progress, challenges and future prospects. *Nat Rev Microbiol* **7:** 666–675

Minamino T, Imada K, Namba K (2008) Molecular motors of the bacterial flagella. *Curr Opin Struct Biol* **18:** 693–701

Miwa K, Yoshida M (1989) The alpha 3 beta 3 complex, the catalytic core of F1-ATPase. *Proc Natl Acad Sci USA* **86:** 6484–6487

Moore SA, Jia YH (2010) Structure of the cytoplasmic domain of the flagellar secretion apparatus component FlhA from Helicobacter pylori. *J Biol Chem* **285:** 21060–21069

Murphy GE (2007) *Cryoelectron Tomography of Bacteria and Their Macromolecular Machines*. Pasadena, USA: California Institute of Technology

Murphy GE, Leadbetter JR, Jensen GJ (2006) *In situ* structure of the complete Treponema primitia flagellar motor. *Nature* **442:** 1062–1064

Overbeek R, Fonstein M, D'Souza M, Pusch GD, Maltsev N (1999) The use of gene clusters to infer functional coupling. *Proc Natl Acad Sci USA* **96:** 2896–2901

Pallen MJ, Matzke NJ (2006) From the origin of species to the origin of bacterial flagella. *Nat Rev Microbiol* **4:** 784–790

Pallen MJ, Penn CW, Chaudhuri RR (2005) Bacterial flagellar diversity in the post-genomic era. *Trends Microbiol* **13:** 143–149

Paul K, Erhardt M, Hirano T, Blair DF, Hughes KT (2008) Energy source of flagellar type III secretion. *Nature* **451:** 489–492

Saijo-Hamano Y, Imada K, Minamino T, Kihara M, Shimada M, Kitao A, Namba K (2010) Structure of the cytoplasmic domain of FlhA and implication for flagellar type III protein export. *Mol Microbiol* **76:** 260–268

Saijo-Hamano Y, Minamino T, Macnab RM, Namba K (2004) Structural and functional analysis of the C-terminal cytoplasmic domain of FlhA, an integral membrane component of the type III flagellar protein export apparatus in Salmonella. *J Mol Biol* **343:** 457–466

Schoenhals GJ, Macnab RM (1996) Physiological and biochemical analyses of FlgH, a lipoprotein forming the outer membrane L ring of the flagellar basal body of Salmonella typhimurium. *J Bacteriol* **178:** 4200–4207

Snyder LAS, Lornan NJ, Futterer K, Pallen MJ (2009) Bacterial flagellar diversity and evolution: seek simplicity and distrust it? *Trends Microbiol* **17:** 1–5

Sowa Y, Berry RM (2008) Bacterial flagellar motor. *Q Rev Biophys* **41:** 103–132

Stallmeyer MJB, Hahnenberger KM, Sosinsky GE, Shapiro L, Derosier DJ (1989) Image reconstruction of the flagellar basal body of Caulobacter crescentus. *J Mol Biol* **205:** 511–518

Suloway C, Shi J, Cheng A, Pulokas J, Carragher B, Potter CS, Zheng SQ, Agard DA, Jensen GJ (2009) Fully automated, sequential tilt-series acquisition with Leginon. *J Struct Biol* **167:** 11–18

Suzuki H, Yonekura K, Namba K (2004) Structure of the rotor of the bacterial flagellar motor revealed by electron cryomicroscopy and single-particle image analysis. *J Mol Biol* **337:** 105–113

Takahashi N, Mizuno S, Hirano T, Chevance FFV, Hughes KT, Aizawa SI (2009) Autonomous and FliK-dependent length control of the flagellar rod in Salmonella enterica. *J Bacteriol* **191:** 6469–6472

Terashima H, Fukuoka H, Yakushi T, Kojima S, Homma M (2006) The Vibrio motor proteins, MotX and MotY, are associated with the basal body of Na+-driven flagella and required for stator formation. *Mol Microbiol* **62:** 1170–1180

Thomas DR, Francis NR, Xu C, DeRosier DJ (2006) The three-dimensional structure of the flagellar rotor from a clockwise-locked mutant of Salmonella enterica serovar Typhimurium. *J Bacteriol* **188:** 7039–7048

Tivol WF, Briegel A, Jensen GJ (2008) An improved cryogen for plunge freezing. *Microsc Microanal* **14:** 375–379

Worrall LJ, Vuckovic M, Strynadka NCJ (2010) Crystal structure of the C-terminal domain of the Salmonella type III secretion system export apparatus protein InvA. *Protein Sci* **19:** 1091–1096

Yonekura K, Yakushi T, Atsumi T, Maki-Yonekura S, Homma M, Namba K (2006) Electron cryomicroscopic visualization of PomA/B stator units of the sodium-driven flagellar motor in liposomes. *J Mol Biol* **357:** 73–81

Zarivach R, Deng WY, Vuckovic M, Felise HB, Nguyen HV, Miller SI, Finlay BB, Strynadka NCJ (2008) Structural analysis of the essential self-cleaving type III secretion proteins EscU and SpaS. *Nature* **453:** 124–127

Zarivach R, Vuckovic M, Deng WY, Finlay BB, Strynadka NCJ (2007) Structural analysis of a prototypical ATPase from the type III secretion system. *Nat Struct Mol Biol* **14:** 131–137

Zerbino DR, Birney E (2008) Velvet: algorithms for *de novo* short read assembly using de Bruijn graphs. *Genome Res* **18:** 821–829

Zheng SQ, Keszthelyi B, Branlund E, Lyle JM, Braunfeld MB, Sedat JW, Agard DA (2007) UCSF tomography: an integrated software suite for real-time electron microscopic tomographic data collection, alignment, and reconstruction. *J Struct Biol* **157:** 138–147